Earth-Science Reviews 257 (2024) 104901

Contents lists available at ScienceDirect

Earth-Science Reviews

journal homepage: www.elsevier.com/locate/earscirev

Review Article

The uplift of the East Africa - Arabia swell

Andrea Sembroni [a,*], Claudio Faccenna [a,b], Thorsten W. Becker [c,d,e], Paola Molin [a]

[a] Department of Science, Roma Tre University, Rome, Italy
[b] GFZ, German Research Center for Geoscience, Germany
[c] Institute for Geophysics, Jackson School of Geosciences, The University of Texas at Austin, USA
[d] Department of Earth and Planetary Sciences, Jackson School of Geosciences, The University of Texas at Austin, USA
[e] Oden Institute for Computational Engineering & Sciences, The University of Texas at Austin, USA

ARTICLE INFO

Keywords:
Horn of Africa
Arabia
Afar superplume
Swell
Topography
Volcanism

ABSTRACT

The East Africa - Arabia topographic swell is an anomalously high-elevation region of ~4000 km long (from southern Ethiopia to Jordan) and ~ 1500 km wide (from Egypt to Saudi Arabia) extent. The swell is dissected by the Main Ethiopian, Red Sea, and Gulf of Aden rifts, and characterized by widespread basaltic volcanic deposits emplaced from the Eocene to the present. Geochemical and geophysical data confirm the involvement of mantle processes in swell formation; however, they have not been able to fully resolve some issues, e.g., regarding the number and location of plumes and uplift patterns. This study addresses these questions and provides a general evolutionary model of the region by focusing on the present topographic configuration through a quantitative analysis and correlating long and intermediate wavelength features with mantle and rifting processes. Moreover, the isostatic and dynamic components of topography have been evaluated considering a range of seismic tomographic models for the latter. When interpreted jointly with geological data including volcanic deposits, the constraints do imply causation by a single process which shaped the past and present topography of the study area: the upwelling of the Afar superplume. Once hot mantle material reached the base of the lithosphere below the Horn of Africa during the Late Eocene, the plume flowed laterally toward the Levant area guided by pre-existing discontinuities in the Early Miocene. Plume material reached the Anatolian Plateau in the Late Miocene after slab break-off and the consequent formation of a slab window. During plume material advance, buoyancy forces led to the formation of the topographic swell and tilting of the Arabia Peninsula. The persistence of mantle support beneath the study area for tens of million years also affected the formation and evolution of the Nile and Euphrates-Tigris fluvial networks. Subsequently, surface processes, tectonics, and volcanism partly modified the initial topography and shaped the present-day landscape.

1. Introduction

Earth's topography is the expression of the interactions between the floating equilibrium of a density column, surface processes, flexure, lithospheric deformation (i.e., tectonics, volcanism, and magmatic underplating), and mantle dynamics (e.g., Braun, 2010; Flament et al., 2013; Faccenna and Becker, 2020). To unravel some of these processes, the contributions to topography can be inferred as being due to two main components: the isostatic and dynamic ones (e.g., Panasyuk and Hager, 2000; Gvirtzman et al., 2016). The first depends on the heterogeneities in lithosphere structure and density; the second represents the deflection of the surface in response to mantle tractions arising from density driven flow in the mantle and plate motions. In particular, upwellings (i.e., mantle plumes), caused by the rise of hot mantle material, and downwellings, related to the descent of cold lithosphere during subduction, can cause uplift and subsidence at the surface, respectively (e.g., Hager et al., 1985; Panasyuk and Hager, 2000; Braun, 2010; Flament et al., 2013).

Mantle plumes show complex morphologies and dynamics (e.g. Heron, 2018; Koppers et al., 2021). One may classify them as "primary", consisting of whole-mantle structures rising from the core-mantle boundary as narrow, localized conduits or in the form of broader upwellings, or superplumes. "Secondary" plumes are confined to the upper mantle as the result of stagnation of the primary plumes at the base or within the mantle-transition zone (Ritsema et al., 1999; Courtillot et al., 2003; French and Romanowicz, 2015; Cloetingh et al., 2022). Regions

* Corresponding author.
E-mail address: andrea.sembroni@uniroma3.it (A. Sembroni).

https://doi.org/10.1016/j.earscirev.2024.104901
Received 15 February 2024; Received in revised form 10 August 2024; Accepted 15 August 2024
Available online 18 August 2024

affected by primary mantle plumes are often characterized by the emplacement of a huge volume of igneous rocks (Large Igneous Provinces – LIPs) typically attributed to the plume head arrival (e.g., Richards et al., 1989; Burke and Torsvik, 2004), and by broad, anomalously high-elevated regions (topographic swells; e.g. Richards et al., 1988; Ribe and Christensen, 1994; Heron, 2018). Despite successive isostatic adjustments and rifting events, topographic anomalies can be preserved for tens of millions of years by processes such as crustal thickening (McKenzie, 1984; Cox, 1989) and/or by the persistence of a mantle anomaly below the crust (Faccenna et al., 2019).

Topographic swells associated with mantle plumes are documented worldwide on both oceanic and continental plates (Dietz and Menard, 1953; Ribe and Christensen, 1994a, 1994b; Ribe and Christensen, 1999; Gurnis et al., 2000; Sengör, 2001; Daradich et al., 2003; Roberts and

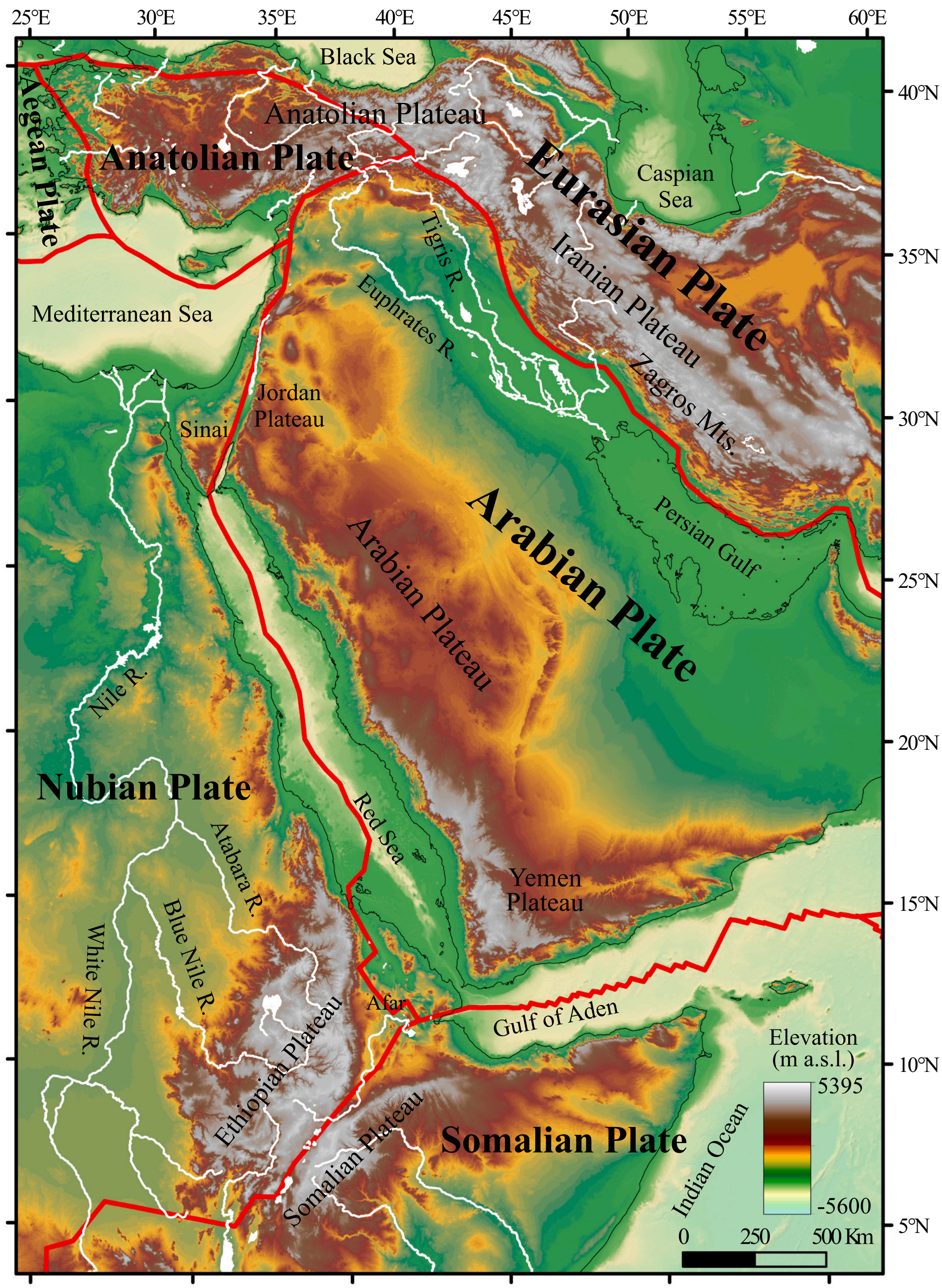

Fig. 1. Topographic configuration of the study area (ETOPO2022 global elevation model with resolution of ~500 m; www.ngdc.noaa.gov); the EAAS extends from south to north comprising the Ethiopian, Somalian, Arabian, and Jordan plateaux; solid red lines indicate plates boundaries. (For interpretation of the references to colour in this figure legend, the reader is referred to the web version of this article.)

White, 2010; Jones et al., 2012; Roberts et al., 2012; Davila and Lithgow-Bertelloni, 2013; Rowley et al., 2013; Czarnota et al., 2014; Paul et al., 2014; Liu, 2015; Heller and Liu, 2016; Sembroni et al., 2016a, 2021; Faccenna et al., 2019; Friedrich, 2019; Clementucci et al., 2023; Molin et al., 2023). Their formation and evolution has been addressed with numerical and analog convection models (e.g. Houseman, 1990; Griffiths and Campbell, 1991; Farnetani and Richards, 1994; Ribe and Christensen, 1994a, 1994b; Ribe and Christensen, 1999; d'Acremont et al., 2003; Burov and Guillou-Frottier, 2005; Moucha et al., 2008; Braun, 2010; Moucha and Forte, 2011; Crameri et al., 2012; Burov and Gerya, 2014; Koptev et al., 2015; Kiraly et al., 2015; Barnett-Moore et al., 2017; Koptev et al., 2017; Rubey et al., 2017; Sembroni et al., 2017; Cao et al., 2018).

One of the most studied ongoing swells is the East Africa-Arabia one (EAAS), also called the "Afro-Arabian dome" (Cloos, 1939; Almond, 1986; Camp and Roobol, 1992). It is an anomalously high-elevated region ~4000 km long (from southern Ethiopia to Jordan) and ~1500 km wide (from Egypt to Saudi Arabia; Cloos, 1939; Almond, 1986, Camp and Roobol, 1992; Avni et al., 2012; Bar et al., 2016; Fig. 1). The area is dissected by the Main Ethiopian, Red Sea, and Gulf of Aden rifts and is characterized, along its entire extent, by widespread volcanic deposits varying in age from Eocene to present-day (Coleman et al., 1983; Brown

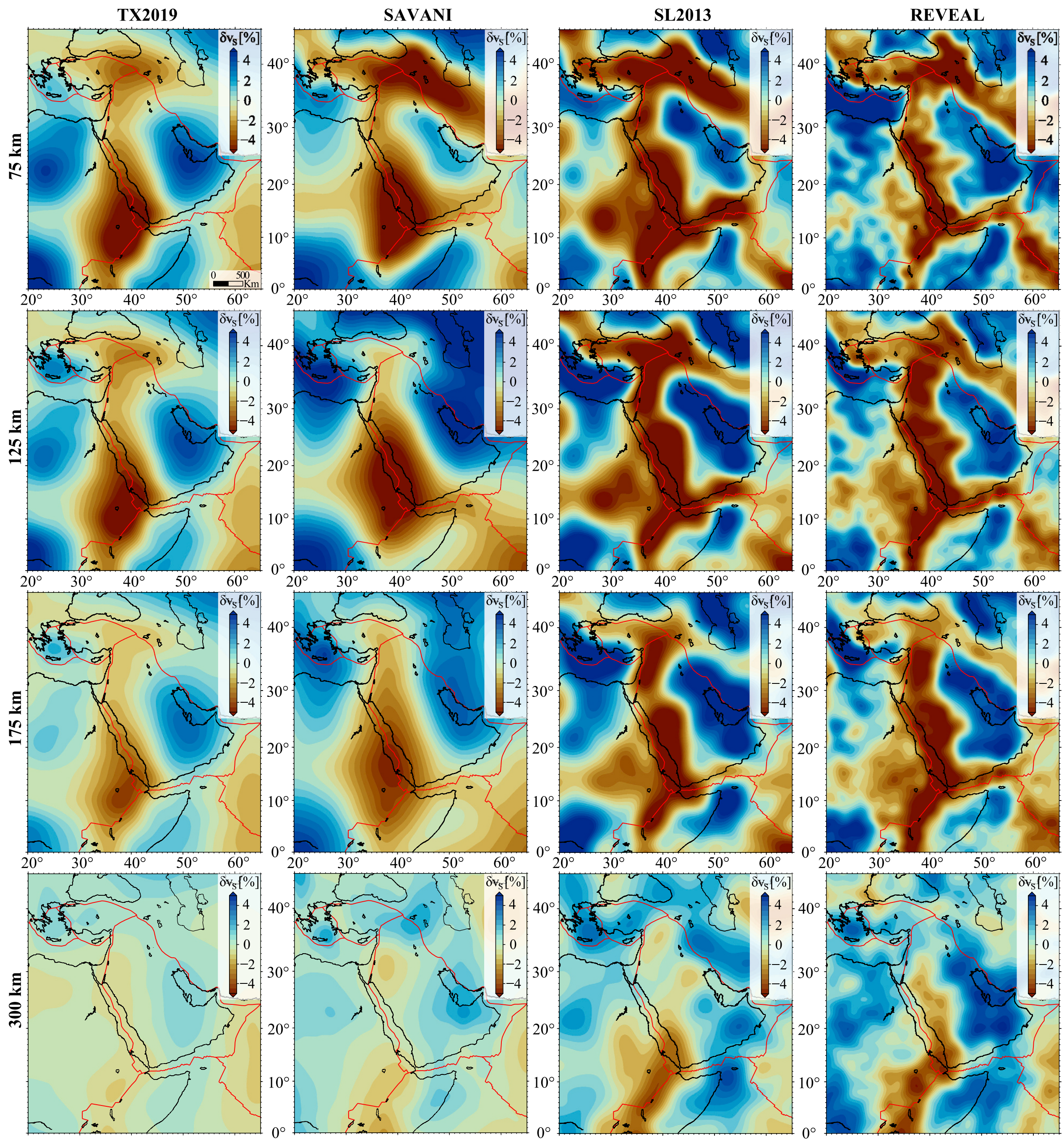

Fig. 2. Comparison of uppermost mantle structure from selected, global shear wave tomographic models: TX2019 (Lu et al., 2019), a body wave model, SAVANI (Auer et al., 2014) a radially anisotropic model based on body and surface waves, SL2013 (Schaeffer and Lebedev, 2013) a surface wave focused, higher resolution SV model, and REVEAL (Thrastarson et al., 2024), a full waveform inversion model. All tomographic models plotted at 75, 125, 175, and 300 km depth. Note the broad region of low seismic velocity below the area comprised between eastern Africa and Levant region. Overall anomalies are consistent across models, with the higher regional resolution models showing consistent northward slow structures, undulating underneath the Arabian plate.

et al., 1989; Camp and Roobol, 1992; Hofmann et al., 1997; Bosworth and Stockli, 2016; Purcell, 2017; Rooney, 2017; Fig. 1). The chemical composition (Baker et al., 1996; Kieffer et al., 2004; Rooney, 2017) and radiogenic isotope ratios (Krienitz et al., 2009; Hua et al., 2023) of the volcanics are consistent with a mantle source with lithospheric contamination.

Several seismic tomography studies show the presence of a broad region of low seismic velocity below the EAAS, interpreted as the signature of hot mantle material (Lithgow-Bertelloni and Silver, 1998; Ritsema et al., 1999; Gurnis et al., 2000; Nyblade et al., 2000; Ritsema and van Heijst, 2000; Benoit et al., 2006a, 2006b; Montagner et al., 2007; Bastow et al., 2008, 2011; Chang and Van der Lee, 2011; Moucha and Forte, 2011; Nyblade, 2011; Faccenna et al., 2013; Hansen and Nyblade, 2013; Schaeffer and Lebedev, 2013; Auer et al., 2014; Emry

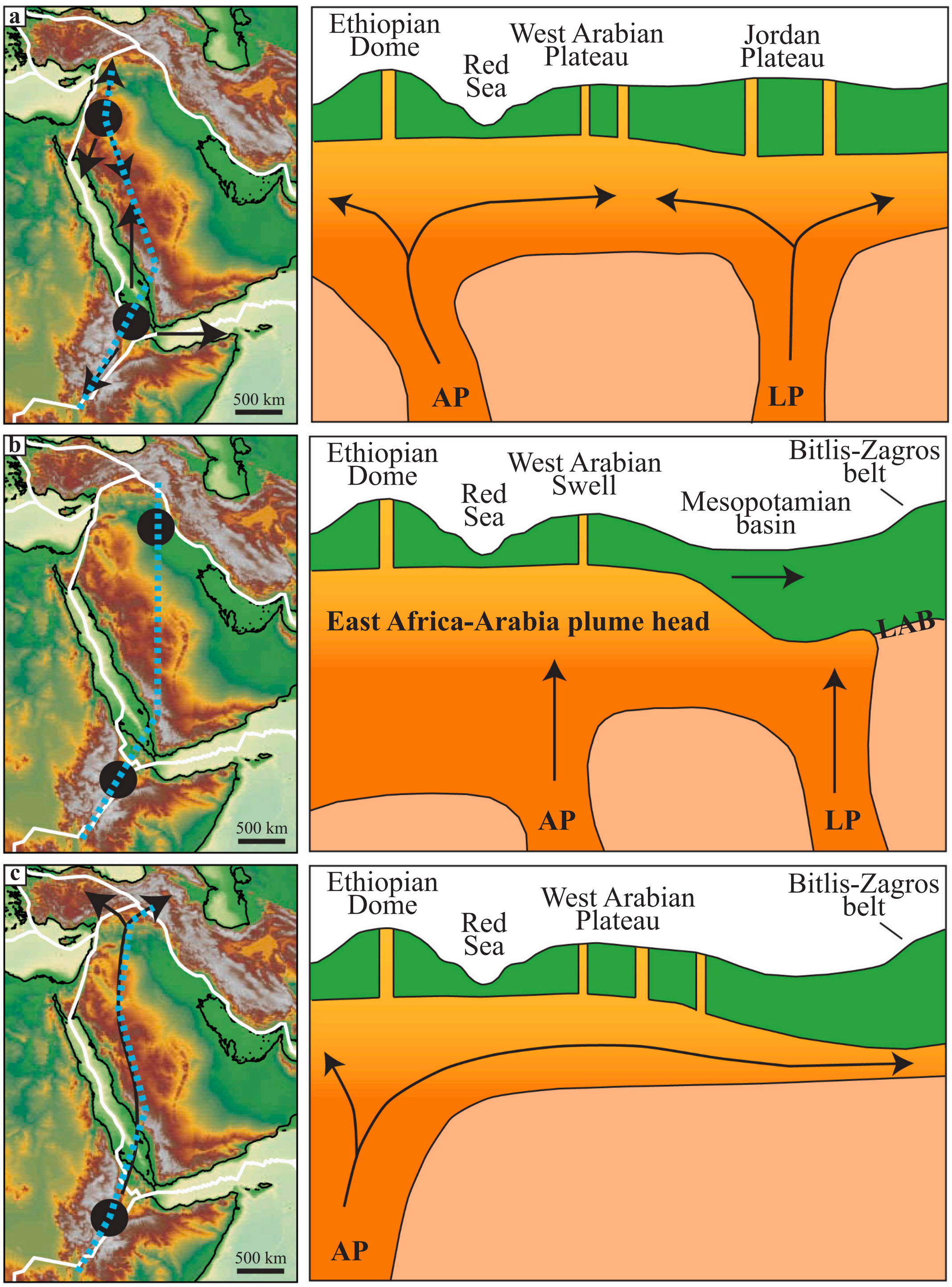

Fig. 3. Schematic maps showing locations of mantle plumes and mantle flow directions (left) with the relative conceptual models (right) according to (a) Chang and Van der Lee (2011), (b) Civiero et al. (2022), and (c) Faccenna et al. (2013). The dashed light blue lines on the maps indicate the traces of the schematic sections represented on the right. AP = Afar Plume; LP = Levant Plume. (For interpretation of the references to colour in this figure legend, the reader is referred to the web version of this article.)

et al., 2019; Lu et al., 2019; Wei et al., 2019; Chang et al., 2020; Tsekhmistrenko et al., 2021; Thrastarson et al., 2024; see Fig. 2). However, although the role of mantle processes has been commonly accepted as the main cause of the current topographic and geologic configurations of the region, in past years there has been debate about the location and number of plumes (Dixon et al., 1989; Ebinger and Sleep, 1998; Chang and Van der Lee, 2011; Hansen et al., 2012; Faccenna et al., 2013; Koulakov et al., 2016). More recent whole-mantle studies (Chang et al., 2020; Tsekhmistrenko et al., 2021; Civiero et al., 2022; Boyce et al., 2021, 2023) seem to converge on the consensus that the region is underlain by a broad low wave velocity anomaly (primarily the African Superplume) with potential addition from other deep-seated plume tails.

In particular, three models can be recognized (Fig. 3). The first indicates the presence of two near-vertical mantle plumes rising below Afar and northern Arabia and flowing beneath the lithosphere (e.g., Debayle et al., 2001; Montagner et al., 2007; Sicilia et al., 2008; Chang and Van der Lee, 2011; Koulakov et al., 2016; Fig. 3a). The second assumes two stationary plumes (Afar and northern Arabia plumes) beneath moving lithospheric plates; in this case, the plume head is stagnating below the lithosphere (e.g., Civiero et al., 2022; Fig. 3b). The last model, in accordance with regional seismic velocity, anisotropy patterns, and seismic tomography (Hansen et al., 2006; Berk Biryol et al., 2011; Schaeffer and Lebedev, 2013; Auer et al., 2014; Qaysi et al., 2018; Lu et al., 2019; Wei et al., 2019; Thrastarson et al., 2024) considers only one mantle plume (Afar superplume) rising below eastern Africa, but flowing to eastern Turkey through pressure gradients and/or prior discontinuities (e.g., Camp and Roobol, 1992; Ebinger and Sleep, 1998; Ershov and Nikishin, 2004; Hansen et al., 2012; Faccenna et al., 2013; Wei et al., 2019; Lim et al., 2020; Agostini et al., 2021; Hua et al., 2023; Fig. 3c).

The uplift pattern of the area is also controversial. In Ethiopia, the uplift is believed to have occurred before (Sengör, 2001), during (Pik et al., 2003), or after (Gani et al., 2007) the emplacement of the volcanic deposits. Some studies (Sembroni et al., 2016a, 2021; Faccenna et al., 2019) suggest that the present topography of Eastern Africa is “a long-term, dynamically supported feature” initiated, at least, in the Oligocene which deeply influenced the present path of the Nile River system (Faccenna et al., 2019). Along the western portion of the Arabian Peninsula, the existence of two distinct groups of volcanic deposits (one dated between 30 and 20 Ma and one younger than 12 Ma), separated by a stasis of few million years in volcanic activity, led Camp and Roobol (1992) to constrain the “initiation of significant uplift”, associated with an active mantle upwelling, at the Miocene. Lastly, studies on the topography of the Levant area allowed much of the uplift and the topography to be attributed to the late Oligocene (Avni et al., 2012; Bar et al., 2016).

In this study, we intend to contribute to the discussion about mantle plume number, volcanism, and uplift of the east Africa-Arabia region by analyzing the present surface topographic signal.

Analogue and numerical models produced surface topography related to the impingement of a mantle plume in the form of a long wavelength bulge. While the modeled dynamic topography amplitude scales with asthenospheric density anomalies to first order, the details of geometry and uplift rates depend on mantle–lithosphere interactions, rheological structure, and intraplate stresses (Griffiths and Campbell, 1991; Burov and Gerya, 2014; Kiraly et al., 2015; Sembroni et al., 2017). However, the presence of multiple mantle plumes would suggest a topographic configuration that gives rise to multiple bulges separated by depressed areas. In the case of a single plume locally channelized, the expected surface topography would be characterized by a ridge with the highest elevation at the impingement zone and a gradual decrease to the distal portion.

Therefore, it is not enough to observe the mantle signal to define the geodynamic configuration of a given area. There is a need for the interpretation of that signal to be consistent with the observed surface topographic configuration. To this end we performed a topography analysis (filtered topography, slope, swath profiles) and reevaluated isostatic (flexural isostasy) and dynamic components combining new data with a review of data from literature. Moreover, the pattern of topography along the entire area and the age trend of volcanic deposits of mantle origin have been compared to verify a common trend. The results allow the current topographic configuration of the East Africa-Arabia swell to be attributed to a single mantle plume that, flowing horizontally from East Africa to Turkey, caused uplift and intense volcanism from Eocene to present, influencing the formation and evolution of the major river networks of the area. Much of the present topography is the result of that uplift and of the successive modification by tectonics and surface processes.

2. Geological evolution

The EAAS extends within the Neoproterozoic Arabian Nubian Shield which is split between the Arabian and African plates and extends from Egypt (Sinai Peninsula), through Saudi Arabia, southward to Kenya (Fig. 4). It represents the northern portion of the East African Orogen that formed during the Pan-African Orogeny (900–550 Ma; Stern, 1994) when East and West Gondwana collided to form the supercontinent “Greater Gondwana” or “Pannotia” at the end of Neoproterozoic (Stern, 2002). In the southern part of the shield (Ethiopia and Kenya), the collision produced a pervasive north-trending shear zones; the central-southwestern sections were subjected to oblique and orthogonal east-west compression accompanied by north-south stretching; in the northern and northeastern parts (Arabian Peninsula), shearing and NW-trending thrusting, extension and tectonic escape, resulted in the NW-trending Najd Fault System (Johnson et al., 2017, and references therein).

In the Cambrian, an intensive erosional denudation affected the Arabian-Nubian Shield, forming an extensive low-relief surface over its northern part (e.g., Garfunkel, 1999; Johnson, 2003; Avigad and Gvirtzman, 2009) and in the Horn of Africa (the “pre-Ordovician planation surface” of Coltorti et al., 2007). Between the Precambrian and the Permian, the deposition of sediments at the Gondwana margin formed the Arabian Platform. While the deposits thickened toward the margin of the Arabian Platform, several erosion events exposed the Precambrian basement (e.g., Lebkicher, 1960; Powers et al., 1966; Murris, 1980; Weissbrod and Gvirtzman, 1989; Beydoun, 1991; Kohn et al., 1992; Alsharhan and Nairn, 1995; Ziegler, 2001; Garfunkel, 2002).

During the Permian and Early Mesozoic, continental fragments drifted away and migrated northward, leaving Arabia facing the newly born Neotethys Ocean (e.g., Dercourt et al., 1986; Beydoun, 1991; Alsharhan and Nairn, 1995). In the Horn of Africa this period is characterized by the formation of the Karoo-type rifts and the deposition of 2–4 km of clastic sediments (Beltrandi and Pyre, 1973; Davidson and McGregor, 1976; Davidson, 1983; Hunegnaw et al., 1998; Mège et al., 2015; Macgregor, 2018). Moreover, another denudation event originated a second planation surfaces (the “Late Triassic planation surface” of Coltorti et al., 2007, or the “paleotopography 1” of Sembroni and Molin, 2018) which indicates a pronounced uplift phase (from hundreds of meters to a thousand; see Coltorti et al., 2007). In the Jurassic, after the development of NE–SW and N-S striking structural basins, a main marine transgression took place from S and SE determining the deposition of thick sequences of marine marls, limestones, and evaporites (Guiraud et al., 2005; Davison and Steel, 2018; Macgregor, 2018). Since the Lower Jurassic, the extensional deformation caused the separation of the Madagascar-India block from Eastern Gondwana (Reeves and De Wit, 2000; Seward et al., 2004; Gibbons et al., 2013; Gaina et al., 2015; Macgregor, 2018). During the Late Cretaceous, the closure of the Neotethys Ocean (e.g., Robertson and Dixon, 1984; Garfunkel, 1998, 2004; Robertson et al., 2006) resulted in a horizontal compression and the formation of the S-shaped Syrian Arc fold belt, extending from Sinai to

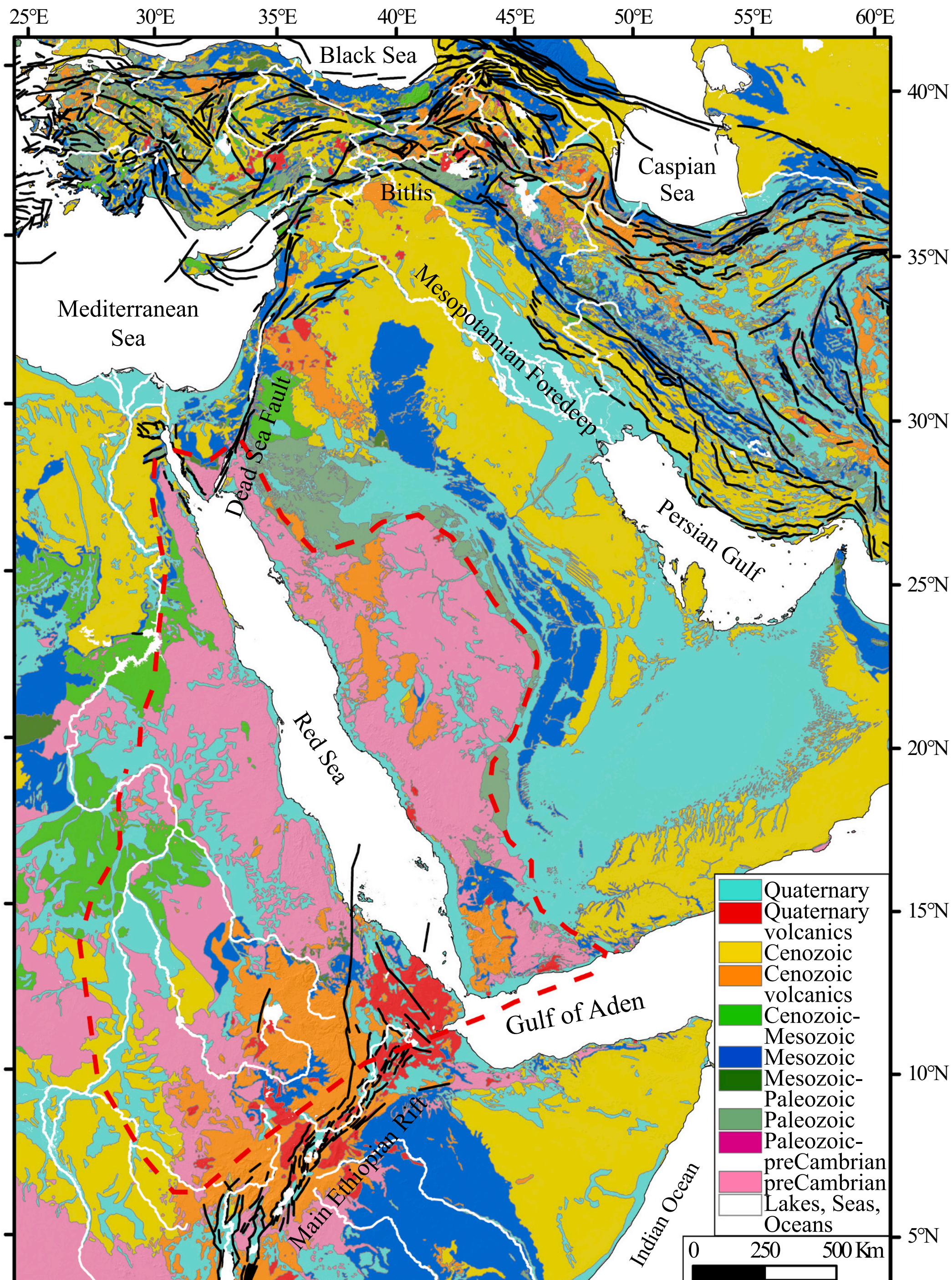

Fig. 4. Geological map of the study area (modified from the Lithologic Map of the World; (Hartmann and Moosdorf, 2012); active tectonic lineaments (solid black lines) are from the Global Active Faults database by Styron and Pagani (2020); dashed red line contours the Arabian-Nubian Shield (from Alemu, 2021). (For interpretation of the references to colour in this figure legend, the reader is referred to the web version of this article.)

Syria where it is represented by the Palmyride inversion zone and fold belt (Krenkel, 1924; Chaimov et al., 1990; Brew et al., 2001), while in eastern Africa a new extensional tectonic phase formed several NW-SE narrow basins and a third denudation event originated the "Cretaceous planation surface" (Coltorti et al., 2007), "paleotopography 2" of Sembroni and Molin (2018). At the end of the middle Eocene the most extensive transgression over the Arabian Platform terminated (Ziegler, 2001; Gvirtzman et al., 2011; Avni et al., 2012). In the same period the separation of Arabia from Africa (6–13 mm/yr; Sella et al., 2002; McClusky et al., 2003; Reilinger et al., 2006; Vigny et al., 2006; ArRajehi et al., 2010) occurred along with the development of the Gulf of Aden and Red Sea rift systems (Bosworth et al., 2005; Leroy et al., 2012). Continental rifting at the Gulf of Aden initiated between 38 and 33 Ma (Pik et al., 2013; Robinet et al., 2013; Purcell, 2017; Boone et al., 2021), concurrently with the onset of the Arabia-Eurasia collision (~23 mm/yr; ArRajehi et al., 2010; McClusky et al., 2003; Reilinger et al., 2006; Sella et al., 2002; Vigny et al., 2006). Thermochronology data indicate that collision took place at ~20 Ma along the Bitlis-Zagros zone (Okay et al., 2010), though older ages have been proposed (Pirouz et al., 2017; Koshnaw et al., 2019).

During the Oligocene, geological and thermochronological data indicate a pronounced phase of uplift both in Ethiopia (Şengör, 2001; Pik et al., 2003; Sembroni et al., 2016a, 2016b; Sembroni et al., 2021) and along the Arabian plate (Gvirtzman et al., 2008; Avni et al., 2012; Bar et al., 2013; Turab et al., 2023), where the marine environments shifted toward the margins (e.g., Beydoun, 1991; Alsharhan and Nairn, 1995; Ziegler, 2001). The Arabian inland region and eastern Africa were subjected to denudation, which led to the formation of extensive low-relief surfaces (e.g., Lebkicher, 1960; Alsharhan and Nairn, 1995; Burke and Gunnell, 2008; Avni et al., 2012; Bar et al., 2016) termed "the Oligocene Peneplain" in northern Arabia (Picard, 1951; Quennell, 1958; Garfunkel and Horowitz, 1966; Avni, 1991; Zilberman, 1991; Avni et al., 2012; Zilberman and Calvo, 2013; Bar et al., 2016) and "Trap volcanics planation surface" (Coltorti et al., 2007) or "paleotopography 3" (Sembroni and Molin, 2018) in eastern Africa.

At ~27 Ma, rifting commenced along the western and southern Afar margins (Purcell, 2017). The western Afar faulting marks a continuation of the Red Sea rifting which, in the meanwhile, was opening starting from its southern portion (Bosworth et al., 2005; Wolfenden et al., 2005; Purcell, 2017; Boone et al., 2021). At the beginning of Miocene, the East African Rift (EAR) started the expansion both north and south from the Turkana region (Purcell, 2017).

Between 18 and 14 Ma, the Arabian plate separated from the Sinai sub-plate by the ~1000 km long Dead Sea Transform Fault (DSTF; Quennell, 1958; Freund et al., 1970; Garfunkel, 1981; Garfunkel et al., 1981; Joffe and Garfunkel, 1987; Bosworth et al., 2005) and began rotating counterclockwise. Recent dating of *syn*-faulting calcite has further constrained the formation of the DSTF plate boundary to 20.8–18.5 Ma in southern Israel and propagating northwards by 17.1 Ma (Nuriel et al., 2017). At the northern boundary of the Arabian Plate, the stress regime appears to have changed from compressional to strike slip, due to the oblique collision between Anatolian and Arabian plates (e.g., Beydoun, 1999). This caused the lateral escape of the Anatolian Plate, accommodated by a system of lithospheric scale dextral (North Anatolian Fault) and sinistral (East Anatolian Fault) strike slip faults (Şengör et al., 2005; Reilinger et al., 2006; Ballato et al., 2018). At ~13 Ma the EAR tectonic activity increased: the Western Branch and the northern segment of the Main Ethiopian Rift (MER) started to form (Macgregor, 2015; Purcell, 2017).

The central portion of the MER started joining the southern and northern segments between 8 and 5 Ma (Bonini et al., 2005; Abebe et al., 2010). In the Pleistocene, the deformation and the main magmatic activity abandoned the MER margin faults and shifted to the floor of the rift valley with the formation of the oblique Wonji Fault Belt (Ebinger, 2005; Corti, 2009; Purcell, 2017).

From the middle-late Miocene, to the north of the Bitlis collision zone, the Eastern Anatolian Plateau experienced a strong exhumation, probably due to the combined effects of a more advanced stage of the Arabia-Eurasia collision (Okay et al., 2010; Ballato et al., 2011; Cavazza et al., 2018, 2019; Gusmeo et al., 2021; Darin and Umhoefer, 2022) and the arrival of hot mantle material below the lithosphere (Molin et al., 2023, and references therein).

Plate reconstructions and geodetic data suggest that the present-day motion of the Arabian plate relative to the Nubian and the Eurasian plates stayed consistent since at least 11 Ma (e.g., ArRajehi et al., 2010; McClusky et al., 2010; Reilinger and McClusky, 2011; Viltres et al., 2022).

2.1. Volcanism

Intra-plate basaltic volcanism started in southern Ethiopia/northern Turkana at 46 Ma ("Eocene Initial Phase" of Rooney, 2017) and lasted for ~10 Ma. After a short hiatus, new basaltic eruptions ("Oligocene Trap phase"; Rooney, 2017) covered parts of Ethiopia, Eritrea, southern Sudan, and western Yemen by 30–29 Ma (Hofmann et al., 1997; Fig. 4). This period of volcanism was coeval with initial faulting and deposition of syn-rift strata in the Gulf of Aden (Purcell, 2017; Rooney, 2017). In the same period, an intense magmatic activity occurred along the Western Arabian margin exploiting the NW-SE discontinuities associated with the Precambrian Najd Fault System ("Older Harrats"; Bosworth and Stockli, 2016; Fig. 4). Subsequently, a period of relative magmatic quiescence took place in the Horn of Africa with volcanism mainly concentrated in the Turkana area (Ukstins Peate and Bryan, 2008; Brown and Mcdougall, 2011), along the rift margins in Ethiopia and Yemen (Rooney et al., 2013), and in eastern Ogaden (Mège et al., 2016; Sembroni and Molin, 2018).

This period of volcanic quiescence is reflected in Ethiopia by the deposition of voluminous intratrappean sediments composed of red clays and sands between 29 and 27 Ma (Abbate et al., 2014). The last eruptions of the continental flood volcanics occurred at 26.5 Ma in Yemen and 25 Ma in Ethiopia. At 24 Ma basaltic dikes and igneous complexes formed northwest of Afar and along the present-day Red Sea margin of Yemen and Saudi Arabia (e.g., Coleman et al., 1983; Brown et al., 1989; Camp and Roobol, 1992; Ilani et al., 2001; Trifonov et al., 2011). At the same time, a large basaltic volcanic province developed in northern Egypt and in the Harrat Ash Shaam region of Jordan, while extensive NW-SE-trending diking, granitic intrusions and silicic volcanism occurred along the 1700 km length of the Western Arabian margin (Fig. 4).

In the middle-late Miocene voluminous volcanism affected the Eastern Anatolian Plateau (Keskin, 2003) causing the covering of large portion of the forming plateau (Fig. 4). This event seems to be coeval with both the collisional deformation along the Bitilis suture zone and the formation of the northern and eastern Anatolian faults (e.g. Keskin, 2003; Şengör et al., 2003; Faccenna et al., 2006; Faccenna et al., 2013; Schildgen et al., 2014; Memiş et al., 2020). In the same period (~13 Ma) a renewed magmatic phase, associated with the N-S movement along the DSTF, affected the Arabian Shield with the eruption of the so-called "Younger Harrats" (Bosworth and Stockli, 2016). Once initiated, volcanism at most locations continued until present.

3. Geomorphological setting

The East Africa-Arabia region displays spectacular signs of an ongoing mantle-plume impact on its surface. One of the most evident is the EAAS which extends for ~4000 km from Jordan to Ethiopia and ~1500 km from east to west (Almond, 1986; Dixon et al., 1989; Camp and Roobol, 1992; Fig. 1). To the south, the NW-SE trending Turkana depression, developed in the Early Cretaceous, separates the swell from the Kenya dome, while to the north the NW-SE trending Mesopotamian basin stands between the swell and the Bitlis Mts. (Fig. 4). While the low-lying nature of the Turkana region is the result of crustal stretching during the end of Mesozoic and Cenozoic (Kounoudis et al., 2023; Ogden and Bastow, 2022), the Mesopotamian lowland represents what remains of the foreland basin of the Zagros Fold and Thrust Belt and is ~900 km long and ~200 km wide (Berberian, 1995; Hessami et al., 2001).

Several studies demonstrated the presence of paleosurfaces both in the Arabia Peninsula (Avni et al., 2012; Bar et al., 2016) and in the Horn of Africa (Coltorti et al., 2007, 2015; Gani et al., 2007; Sembroni et al., 2016a; Sembroni and Molin, 2018; Sembroni et al., 2021). Avni et al. (2012) documented a regional truncation surface outcropping in the northern portion of the Red Sea and in the southern Levant region which separate middle Eocene – early Oligocene pre-rift deposits from late Oligocene – Holocene conglomerates and volcanic rocks. For this reason, the authors referred this surface to the Oligocene. Bar et al. (2016) extended such a surface to the western half of the Arabia Peninsula and defined it as a planation surface standing at elevation ranging between 800 and 1200 m (Arabian Plateau in Fig. 1). To the west and south, the Arabian Plateau is bounded by the elevated shoulders of the Red Sea and the Gulf of Aden rifts. To the north and east the plateau gently descends toward the Persian Gulf and the Mesopotamian Basin. The northeastern portion of the Arabian Plateau comprises the Jordan Plateau, a large eastward-tilted area with summits at 1200–1700 m and elevation increasing southward (Fig. 1). The evolution of this structure seems to be linked to the formation of the Dead Sea depression (Salameh, 1997; Avni et al., 2012; Bar and Zilberman, 2016; Ben-Israel et al., 2020).

Similarly, at the opposite side of the Red Sea, the Horn of Africa presents remnant surfaces representing the preserved top of the basaltic plateau formed after huge eruptions occurred mainly in the Oligocene Trap phase (the "Trap volcanics planation surface" of Coltorti et al., 2007, or "paleotopography PT3" of Sembroni and Molin, 2018). These sub-horizontal (< 3°) surfaces stand at an elevation comprised between 1000 m (in southern Ethiopia) and 2700 m (in central and northern Ethiopia; Sembroni et al., 2016a, 2016b) forming the so-called Ethiopian-Somalian Plateau (Fig. 1). This plateau is divided into the Ethiopian and Somalian portions by the NE-SW trending MER. Locally, large shield volcanoes rise 1000–2000 m above the average plateau elevation, the highest of which reach elevations >4200 m. The Ethiopian Plateau consists of a flat to gently rolling landscape (Fig. 1). Conversely the Somalian Plateau is much less extensive and presents the flat top along the southeastern margin of the MER (Fig. 1). To the west and southeast of the high elevated plateaux, the topography gradually decreases down to 500 m respectively in the Sudan and Somalian lowlands (Fig. 1). According to several studies the incision of these uplands initiated by regional uplift in the Late Oligocene continuing up to present time (McDougall et al., 1975; Pik et al., 2003; Gani et al., 2007; Ismail and Abdelsalam, 2012; Gani, 2015; Sembroni et al., 2016b; Gani and Neupane, 2018; Sembroni and Molin, 2018; Sembroni et al., 2021; Gani et al., 2023). This long-lasting incision sculpted a landscape characterized by steep slopes bordering high-elevated low relief surfaces underlain by continental flood basalts (plateau remnants; Sembroni et al., 2016b).

The Ethiopian-Somalian and Arabian plateaux are separated by the NW-SE trending Red Sea which displays longitudinal and along-strike variations in rift flank morphology (Fig. 1). In particular, the western margin is characterized by the narrow, 1500 km long "Red Sea Hills" (mean elevation 500 m), while the conjugate Arabian escarpment presents highlands averaging 1000–1500 m in elevation.

Immediately to the north of the Mesopotamian basin, the East Anatolia Plateau consists of a dome-shaped feature characterized by a rolling low-relief topography standing at a mean elevation of ~2000 m (Molin et al., 2023; Fig. 1). Volcanoes rise from its surface, some of which reach 5000 m. To the north and south, the topography decreases down to sea level.

The hydrography of these high elevated region shows a typical radial pattern both in Ethiopia (Nile drainage system; Sembroni et al., 2021) and in Arabia (Fig. 1). An exception is the Eastern Anatolian Plateau where rivers integrate into the plateau in a disorganized way, locally following tectonic structures (i.e., the Euphrates River; Molin et al., 2023; Fig. 1).

4. Deep mantle processes beneath East Africa - Arabia

Uplift, rifting, and volcanism in the East Africa-Arabia region have been related to one or more plumes, based on geochemical, seismic, and other evidence (Ebinger et al., 1989; Camp and Roobol, 1992; Burke, 1996; Ebinger and Sleep, 1998; Courtillot et al., 1999; Rogers et al., 2000; Montelli et al., 2006; Rogers, 2006; Chang and Van der Lee, 2011; Fishwick and Bastow, 2011; Nelson et al., 2012; Chang et al., 2020; Civiero et al., 2022). Thin-lithosphere corridors have been proposed to assist in plume transport or channel plume material to volcanic fields hundreds of kilometers away (cf. Fig. 2; Camp and Roobol, 1992; Ebinger and Sleep, 1998; Faccenna et al., 2013; Agostini et al., 2021; Civiero et al., 2022; Hua et al., 2023).

The strongest geochemical evidence for the presence of plume material below the region is the lack of a prominent contribution from shallow, depleted MORB mantle in the source material for pre-rift volcanism (Baker et al., 1996; Kieffer et al., 2004). Isotopic measurements in the basalts of southern Ethiopia, Afar, and Levant all indicate deep-mantle reservoirs, with a lithospheric component (e.g., Krienitz et al., 2009; Nelson et al., 2012).

Recently, Hua et al. (2023), according to a wide range of seismic and geochemical observations, inferred that the hot asthenosphere beneath Anatolia is fed by long-distance lateral transport of upper mantle from East Africa, with the lateral flow being driven by pressure gradients created by the buoyancy of the African mantle plume, consistent with the earlier inferences of Ershov and Nikishin (2004) and the mantle flow and seismic anisotropy modeling of Faccenna et al. (2013) (Figs. 2 and 5). In agreement with the suggested progressive northward motion of asthenopsheric plume material, seismic body and surface wave imaging (Fig. 2) and seismic anisotropy of the upper mantle, e.g. as inferred from SKS splitting (Fig. 5) beneath East Africa and Arabia appear related to the combination of channelized flow from Afar along the Red Sea (e.g., Hansen et al., 2012; Bagley and Nyblade, 2013; Faccenna et al., 2013; Hammond et al., 2014; Wei et al., 2019), and oriented partial melt pockets of other rifting associated processed closer to the Ethiopian flood basalt province (e.g., Kendall et al., 2005; Bastow et al., 2010; Ebinger et al., 2024).

The associated low-velocity anomaly crosses the upper mantle under East Africa and continues propagating northeasterly to western Arabia (Figs. 2 and 5). Some tomography models show a low-velocity feature in the upper mantle extending from the Red Sea into the interior of Arabia (Debayle et al., 2001; Benoit et al., 2006a, 2006b; Fishwick, 2010; Emry et al., 2019) and a narrow anomaly aligned with the Red Sea but offset to the east (Chang and Van der Lee, 2011; Chang et al., 2011; Koulakov et al., 2016; Lim et al., 2020; Tang et al., 2018; Yao et al., 2017). In contrast, Civiero et al. (2022) proposed three mantle plumes beneath Kenya, Afar, and Levant feeding an integral East Africa-Arabia plume head. Low shear-wave velocities beneath the Gulf of Aden down to 150 km depth were also reported, suggesting that the plume below Afar may be also feeding the Gulf of Aden ridge (Sicilia et al., 2008).

If we assume that seismic anisotropy is due to shear in mantle flow, the updated SKS compilation of Fig. 5 is consistent with previous discussions about plume-related, and slab curtain modulated, asthenospheric channeling, and in particular the mantle flow and texture formation modeling of a more limited SKS dataset by Faccenna et al. (2013). However, the more extensive coverage of the Arabian Peninsula provides an opportunity to further explore details of channeling and deflection of flow by lithospheric structure, for example.

5. Methods and results

To describe the extension and geometry of the EAAS and to investigate the different components of topography, the present topographic configuration of the study area has been analyzed by several techniques including slope map, swath profiles, and filtered topography. To quantify the isostatic component of topography along the Red Sea rift shoulders, the flexural uplift has been calculated. The non-isostatic contribution to topography has been quantified by the realization of residual and dynamic topography maps. As elevation data source we used the ETOPO2022 global elevation model (resolution of 15 arc-second = ~500 m; www.ngdc.noaa.gov) because its relative fine resolution allows the analysis of topography at a regional scale. The data have been extracted and elaborated by means of ArcGIS and MatLab software.

To highlight a possible common trend between topography and volcanism age patterns, topography analysis results have been analyzed together with geochronological data. In detail, 1465 published ages of volcanic deposits from Ethiopia to Turkey have been collected and statistically analyzed.

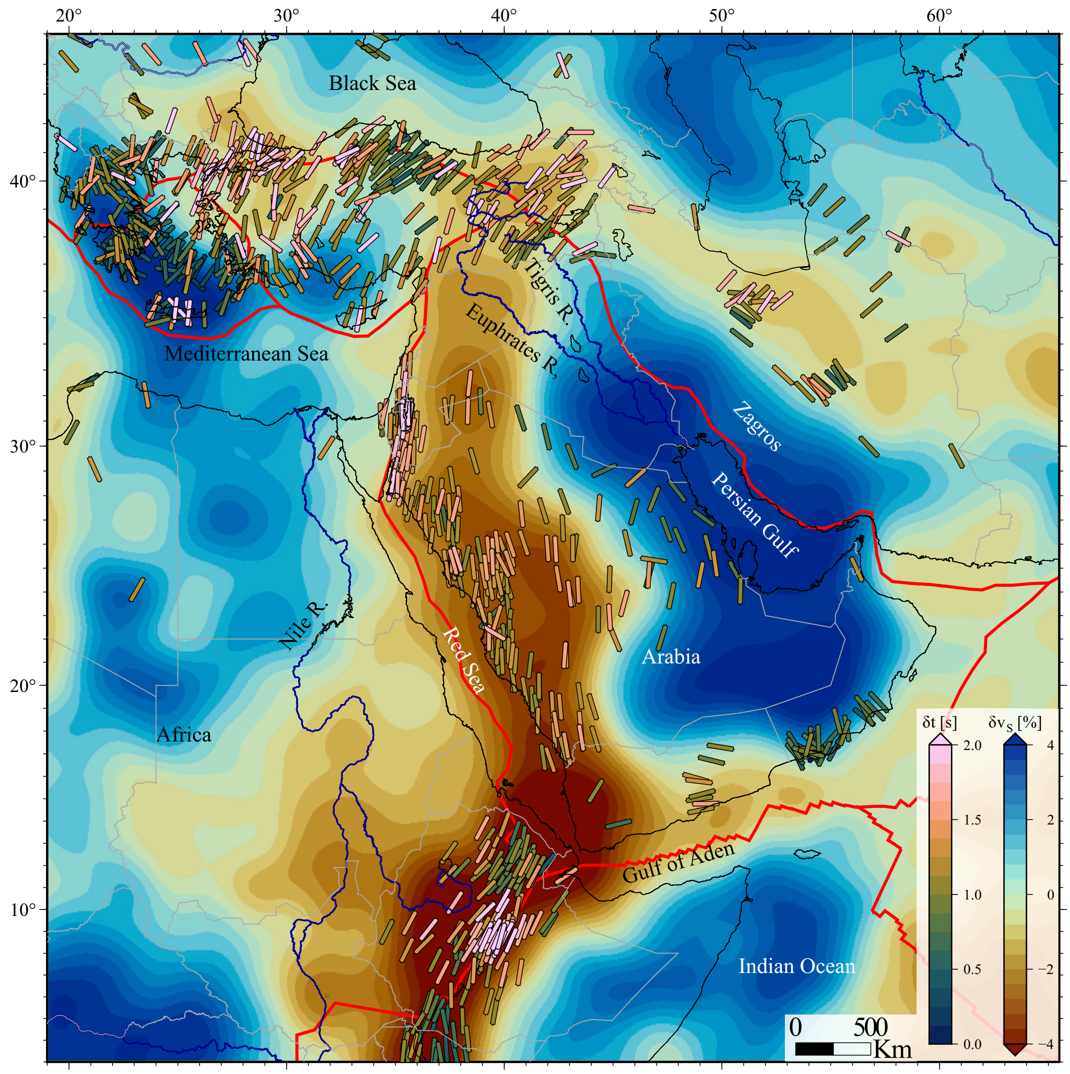

Fig. 5. REVEAL tomography model (Thrastarson et al., 2024) (see Fig. 2) averaged over the 100…400 km depth range (which dominates dynamic topography, cf. Fig. 10f) superimposed by SKS splitting observations aligned with "fast axes" and colored by delay time (compilation of Becker et al., 2012, updated as of 05/2024). Solid black show coastline, blue lines major rivers, and red line major plate boundaries. (For interpretation of the references to colour in this figure legend, the reader is referred to the web version of this article.)

5.1. Slope map and filtered topographies

Slope maps have been widely used to mark morphologies, such as high-standing plateaux or steep escarpments, which are not immediately detectable from the observation of a DEM. In this study, a slope map from the ETOPO2022 DEM has been generated in ArcGIS environment by the "Slope" tool which identifies the variation in elevation over the distance (3 × 3 cell neighborhood) for each cell of the DEM. The tool, interpolating the gradient value of cell centers, generates a plane whose slope value is calculated using the average maximum technique (Burrough and McDonnell, 1998). In this study the values have been classified in four classes (Fig. 6): the first three classes describe flat or gently dipping portions of landscape with slope <15°; the last class covers the range 15°-69° to emphasize escarpments.

The map shows the highest slope values (> 15°) in coincidence with the margins of the Red Sea, the Afar and MER escarpments, along the DSTF, and in the mountainous regions in the southernmost (Ethiopia) and northernmost (Turkey, Armenia, Azerbaijan, Iran) portions of the study area (Fig. 6). The lowest values (< 5°) concentrate on the remaining part and differentiate into low-elevated and high-elevated areas. The former ones correspond to the Nile, Tigris and Euphrates rivers valleys, the Persian Gulf surroundings, and the Horn of Africa coastal zone. Conversely, the high-elevated sub-horizontal surfaces are in the inner sectors of Turkey (Anatolian Plateau) and Iran (Iranian Plateau), along the western margin of the Arabian Peninsula (Arabian Plateau), and in the Ethiopia (Ethiopian-Somalian Plateau).

Previous studies on the region (Almond, 1986; Dixon et al., 1989; Camp and Roobol, 1992; Sengör, 2001; Şengör et al., 2003; Forte et al., 2010; Faccenna et al., 2013; Sembroni et al., 2016a, 2016b, 2021) relate large-scale morphologies to mantle processes. To isolate and quantify this component, the present topography of the study area has been filtered in frequency domain by a circular low pass filter in ArcGIS environment. This methodology has been used in other parts of the world such as Yellowstone and Colorado Plateau (Wegmann et al., 2007; Roy et al., 2009), Eastern Africa (Sembroni et al., 2016b, 2021), Apennines and Carpathians (D'Agostino and McKenzie, 1999; Molin et al., 2004, 2012; Faccenna et al., 2011), and Easter Anatolia Plateau (Molin et al., 2023). To avoid flexural effects, the choice of the filter wavelength is important (Molin et al., 2012). In this study we used two wavelengths: 200 (Fig. 7a) and 400 km (Fig. 7b). Such values are effective in filtering out the topographic signals of crustal tectonics and fluvial wide valleys and to isolate the mantle component (D'Agostino and McKenzie, 1999; Molin et al., 2004, 2012; Wegmann et al., 2007; Roy et al., 2009; Faccenna et al., 2011; Sembroni et al., 2016b, 2021). In particular, the

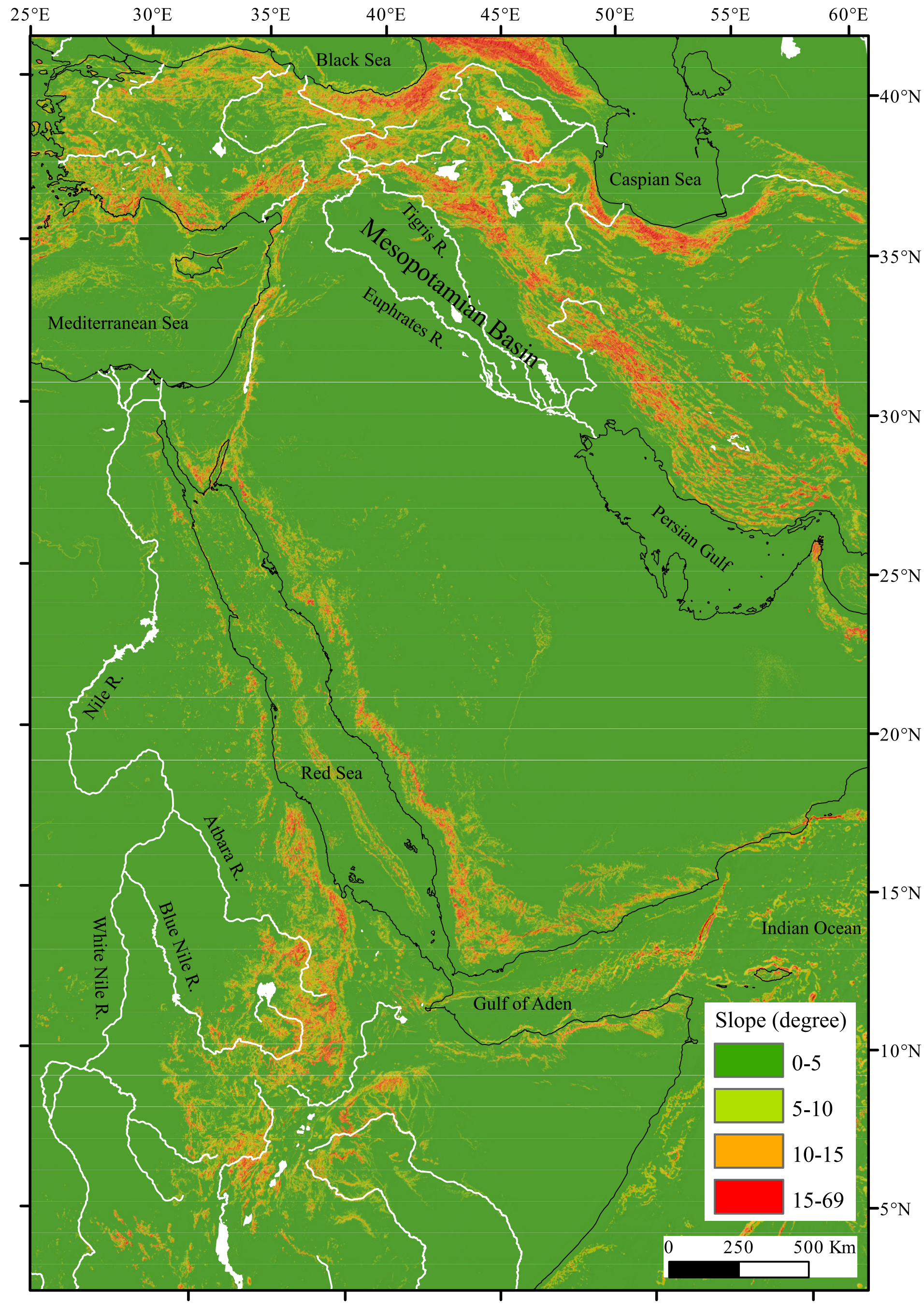

Fig. 6. Slope map of the study area elaborated from the ETOPO2022 global elevation model.

wavelength at 400 km allows to inhibit the topographic influence of the Red Sea, which presents a maximum width of ~300 km, and to discern the deeper component of the topography.

In the filtered topography at 200 km wavelength (Fig. 7a), values between 500 and 1000 m characterize a long strip of land from Ethiopia to Syria (NNW-SSE trend) interrupted only in coincidence with the Red Sea and the Gulf of Aden. Indeed, their maximum amplitude of 300 km exceeds the radius chosen for filtering the topography. We referred this topographic feature to the EAAS. Its highest elevation (1000–2500 m) falls in the Ethiopian-Somalian Plateau and in the southwestern corner of the Arabia peninsula. The swell is bordered to the west and east by lowlands at elevation comprised between 0 and 500 m represented, respectively, by the Nile River Valley and by the Mesopotamian Basin – Persian Gulf area. To the north, the filtered topography slightly decreases in northern Syria and then dramatically increases up to 2500 m in coincidence with the Anatolian Plateau and the Zagros Mts.

In the 400 km filtered topography (Fig. 7b), the swell is still clearly visible presenting almost the same elevation pattern and geometry previously described. In this case the higher elevation (1000–2000 m) focuses exclusively on the Horn of Africa while the Arabian Peninsula shows a relatively homogeneous elevation between 500 and 1000 m.

5.2. Swath profiles

A swath profile is a distance vs. elevation plot in which the trend of maximum, minimum, and mean topography is represented within a specific rectangular observation window (swath). Swath analysis has been widely used to compare magnitudes of orogenic belts (Fielding,

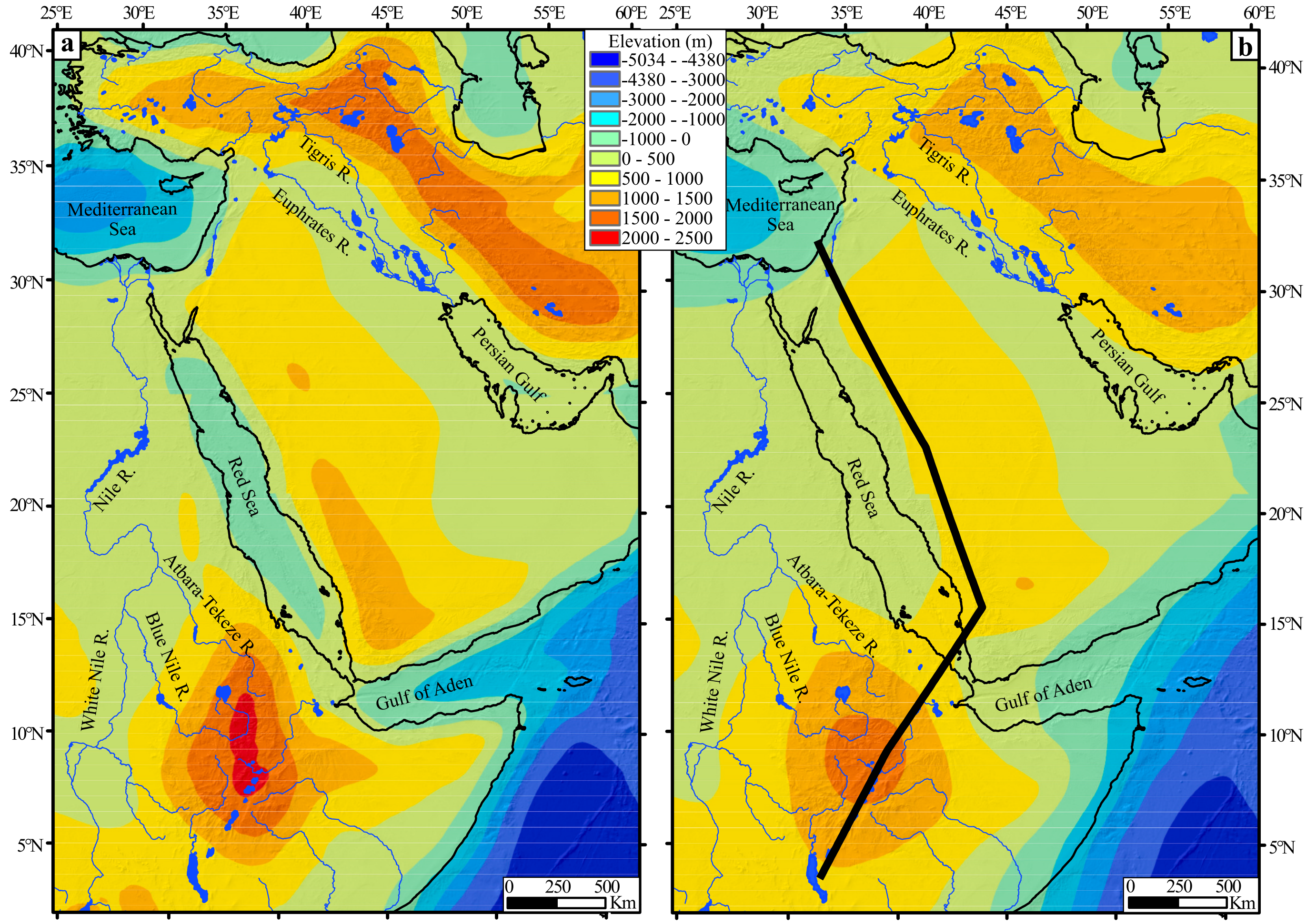

Fig. 7. Filtered topographies at 200 (a) and 400 km (b). The solid black line in (b) indicates the trace of the profiles represented in Fig. 13.

1996), to evaluate the relationship among erosion, precipitation and tectonic uplift (Thiede et al., 2004; Bookhagen et al., 2005; Hoke et al., 2005; Champagnac et al., 2009), to study the impact of rock erodibility on mountainous relief (Kühni and Pfiffner, 2001), and to catch drainage reorganization or fluvial terrace location (Godard et al., 2010; Stüwe et al., 2009; Wegmann and Pazzaglia, 2009). The difference between maximum and minimum topography at each point of the profile quantifies the local relief that, in a non-glaciated area, is a good approximation of fluvial incision (Isacks, 1992; Telbisz et al., 2013; see Fig. S2). Molin et al. (2004) showed that, in active tectonic landscapes, regions of high local relief often correspond with areas of incision in response to uplift.

To investigate the geometry of the EAAS, eight swath profiles have been extracted from the ETOPO2022 DEM by tracing 25 equally spaced topographic profiles into a 100 km wide observation window (Fig. 8). The elevation data along each profile have been sampled every 2 km. According to the configuration of the filtered topography at 200 and 400 km (Figs. 7a, b) we traced six profiles roughly orthogonal to the Red Sea (SW-NE trend), one orthogonal to the Main Ethiopian Rift and one along the crest of the swell, from Ethiopia to the border between Syria and Turkey. The first seven profiles clearly show a ridge-like topography interrupted by the Red Sea or the MER with a geometry varying from north to south (Fig. 8):

Profile 1. The ridge is ~800 km wide from Israel to the Euphrates-Tigris plain with a maximum elevation of ~800 m in coincidence with the Israel-Jordan Plateau. The higher peaks on the plateau correspond to the Harrat Ash Shaam volcanic province where volcanic edifices are 1600 m high.

Profile 2. The ridge considerably enlarges up to ~1000 km with a maximum elevation of ~1000 m occurring entirely on the Arabian margin of the Red Sea. As for Profile 1, the elevation gradually and smoothly decreases down to zero toward NE.

Profile 3. The ridge mostly extends in the Arabian margin with an amplitude of ~1100 km and an elevation of ~1000 m. In the Egypt margin, a small plateau (~200 km in width) at ~600 m of elevation may represent the northwestern portion of the ridge. The highest portion (~1000 m) is characterized by the edifices of three volcanic provinces named Harrat Qalib, Harrat Kura, Harrat Hutaymah arriving at ~2000 m of elevation (Coleman et al., 1983).

Profile 4. A pronounced ridge ~1200 km wide and ~1000 m high. ~200 km of the total width is observable in the Sudan margin while the remaining characterizes the Arabian one. The area with the maximum elevation is centered in the Arabian Plateau. Here the volcanoes of the Harrat Rahat and Harrat Al Kishb volcanic provinces tower up to an elevation of ~1500 m (Coleman et al., 1983).

Profiles 5 and 6. To the southernmost portion of the study area (Profiles 5 and 6) the ridge is first centered in the Red Sea (Profile 5) and then mostly in the southwestern margin (Profile 6) with a maximum width of ~1600 km and an elevation reaching ~2500 m in coincidence with the Ethiopian-Somalian and Yemen plateaux.

Profile 7. Orthogonal to the Main Ethiopian Rift and shows the southernmost portion of the swell. In particular, the bulge presents the highest elevation (~2700 m) and extends for >1300 km from the Sudan and Somalia lowlands, in accordance with previous studies (Sembroni et al., 2016b, 2021). The peaks seen in the maximum topography correspond with the major volcanoes that lie on the Ethiopian-Somalian

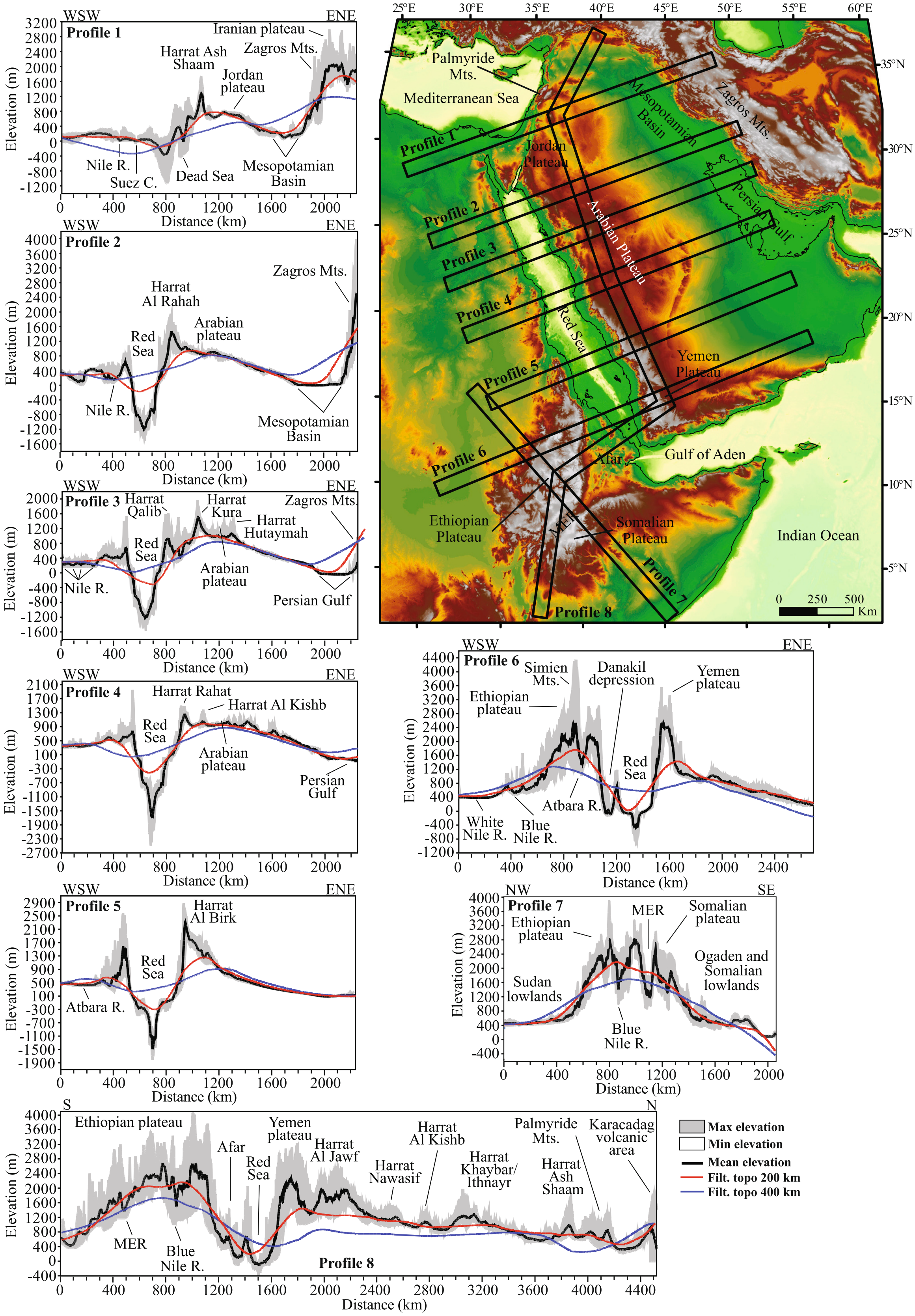

Fig. 8. Swath profiles extracted across the study area. To compare the general topographic configuration with the filtered topography, two curves extracted from the topography filtered at 200 and 400 km (Figs. 7a, b) along the middle line of each swath have been included in the plots. The trace of each swath is represented in the upper right map.

plateau.

Profile 8. Across the crest of the topography anomaly highlighted in the filtered topographies at 200 and 400 km (Figs. 7a, b). The EAAS extends for a total length of ~4000 km from Ethiopia to Jordan with a mean elevation gradually decreasing from ~2700 m (Ethiopia) to ~600 m (Jordan). The surface of the swell is characterized by the high-standing Ethiopian-Somalian and Yemen plateaux and by several volcanic provinces (harrats) in the Arabian portion which make its top surface irregular.

In all profiles, the local relief is low (< 200 m) on the ridge top and flanks, especially in the Arabian one, whereas is moderate to high (400–1000 m) in coincidence with the Red Sea and the MER and Afar margins (Fig. S2).

To better describe the topographic configuration of the swell, two curves extracted from the topography filtered at 200 and 400 km along the middle line of each swath have been included in the swath profiles (Fig. 8). The first curve (200 km in wavelength) roughly approximates the mean topography except for the Red Sea area where shorter wavelengths of topography are dominant. The second curve (400 km in wavelength) appears coincident with the mean topography of the Arabian (eastern) portion of the swell while deviates from the general pattern in the western part. It has negative values at the Indian Ocean coast.

In summary, the analysis of topography by swath profiles allows us to quantitatively define the geometry of the EAAS. It is confined between the Egypt-Sudan lowlands to the SW and the Euphrates-Tigris plain to the NE and characterized by an amplitude and an elevation gradually increasing from north (800 km and 800 m) to south (1600 km and 2700 m). The same trend is present in the topography at the Red Sea margins where the northern portion shows peaks approaching ~1000 m (southwestern margin) and ~2000 m (northeastern margin) of elevation which gradually increase at ~2500 m and ~2900 m respectively to the south. According to several studies (see Stüwe et al., 2022 and references therein) these high elevated portions along the margins of the Red Sea have been caused by the flexural uplift of the rift shoulders whose effect over time has been amplified by complex feedback between seafloor spreading and erosion. The same process has been studied by Weissel et al. (1995) and Sembroni et al. (2016a, 2016b) along the Afar escarpment and the Main Ethiopia Rift margins. The authors found increasing values of flexural uplift from ~500 m in the north to ~1200 m in the south.

5.3. The flexural uplift on the margins of the Red Sea

Although the EAAS represents a long wavelength signal, the opening of the Red Sea rift, with its maximum extent of ~300 km, may have modulated the expression of the swell partially hiding its topographic signal. To quantify such a topographic component, the uplift of rift flanks has been modeled as a flexural response to the unloading of the lithosphere due to extension.

Flexural deflections of the Earth lithosphere can support loads elastically on short wavelengths rather than having an isostatic floating equilibrium, which we expect to hold on long wavelengths, all relative to the effective elastic thickness. Elastic flexure with infill is governed by the equation (Turcotte and Schubert, 1982):

$$\nabla^2\left[D(x,y)\nabla^2 w(x,y)\right] + \Delta\rho g w = q(x,y) \qquad (1)$$

where *w(x,y)* is the deflection of the surface, *D(x, y)* the flexural rigidity, $\Delta\rho$ the density contrast between the crust and the mantle, *g* the acceleration due to gravity, and *q(x, y)* the vertical load applied or removed from the lithosphere. The solution of eq. (1) for the case of a broken lithosphere is (Turcotte and Schubert, 1982):

$$w(x) = w_0 e^{-x/\alpha} cos\frac{x}{\alpha} \qquad (2)$$

$$D = \frac{ET_e^3}{12(1-\nu^2)} \qquad (3)$$

$$\alpha = \left(\frac{4D}{g(\rho_m - \rho_a)}\right)^{1/4} \qquad (4)$$

where w_0 is the maximum vertical displacement caused by the load, α the flexural wavelength, T_e is the equivalent elastic thickness of the lithosphere, ρ_m mantle, and ρ_a air density.

In this study, nine topographic profiles (see Figs. S3, S4), extracted from a smoothed topography (30 km radius smoothing circular window – to remove peaks related to the biggest volcanic edifices), have been fitted by eq. (2) using an iterative, nonlinear least-squares fitting algorithm (as implemented in MatLab). Confidence bounds for fitted coefficients and prediction bounds for the fitting curve reflect a 95% confidence interval (see Fig. S4). Lastly, the data extracted along each profile have been interpolated by a triangulation algorithm in ArcGIS environment obtaining a TIN surface (Fig. 9a).

The results indicate a progressive increase in flexural uplift from north to south on both the Red Sea margins, except for the northernmost portion of the African margin (Fig. 9a). This is in accordance with thermochronological data which dated the beginning of rifting at 26–20 Ma in the southern portion of the Red Sea (Boone et al., 2021 and references therein). On average, the western margin is characterized by lower values (415–3382 m) than the eastern one (1447–2771 m). The deformation related to flexural (flexural wavelength) is consistent up to a maximum of ~250 km from the Red Sea margins (Fig. 9a; Table S1). The inferred elastic thickness varies from 13 to 76 km on the African side (37.7 km average) and from 20 to 29 in the Arabian one (25.2 km on average; Table S1) in agreement with previous studies (Chen et al., 2015; Sreenidhi et al., 2023). In particular, Chen et al. (2015) correlate the relatively small T_e values and the low S-wave velocity anomaly with the elevated topography of the region concluding that the uplift is supported by hot mantle.

To distinguish the different components of topography across the Red Sea area, a topographic profile has been extracted along the southern portion of the Red Sea where the flexural uplift is higher (Fig. 9a). Together with it we plotted the flexural uplift extracted from Fig. 9a and the two curves from the filtered topographies (Figs. 7a, b). The graph shows that the present topography is dominated by the flexural component only in the first ~200 km from the rift shoulders. Beyond that distance, the topography is better approximated by the filtered topography at 400 km (Fig. 9b), consistent with the expectation of dynamic or isostatic control of topography at long wavelengths.

5.4. Residual, dynamic topography, and river networks

Filtered analysis of actual topography can be complemented by considering anomalous topography relative to what is expected isostatically from a given lithospheric model, i.e. residual topography (e.g., Panasyuk and Hager, 2000). Our approach for estimating residual topography follows the approach of Becker et al. (2014) and Faccenna and Becker (2020). As in Faccenna and Becker (2020), we use a modification of the CRUST1 (Laske et al., 2013) global crustal thickness model which we continuously update, e.g. earlier by merging data from the compilation of Gvirtzman et al. (2016) and other studies. Compared to Faccenna and Becker (2020), we here also include a few newer studies as compiled by Boyce et al. (2023) for an updated Moho map that is shown in Fig. 10a (see Boyce et al., 2023, for references). A smoothed version of that new crustal thickness model is then used along with CRUST1 density anomalies to estimate residual, i.e. non-isostatic, topography, ignoring any lateral lithospheric mantle density or thickness variations, for simplicity.

The resulting, updated residual topography map (Fig. 10b) is overall very similar to that of Faccenna and Becker (2020) and Stephenson et al.

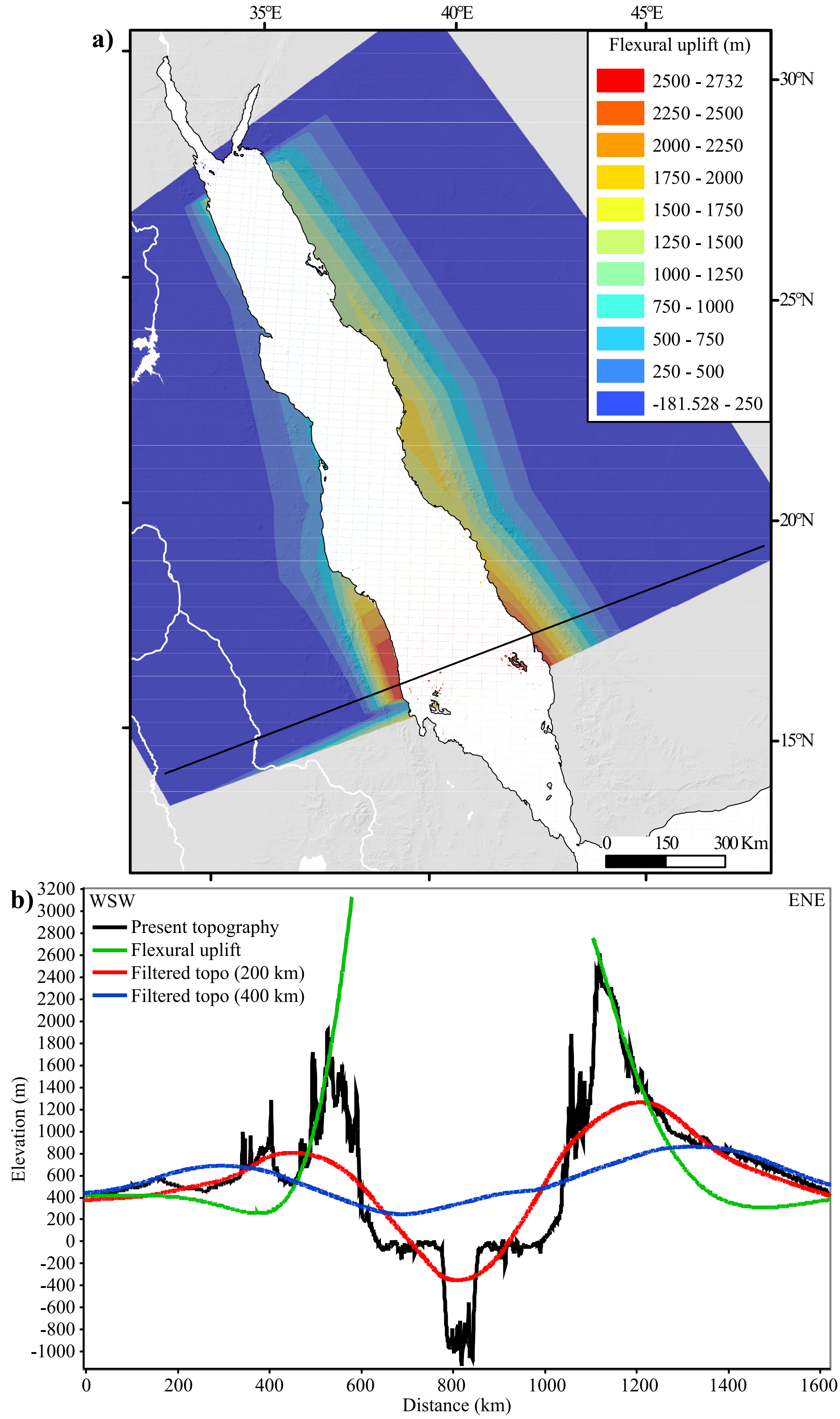

Fig. 9. a) Map of the flexural uplift calculated along the Red Sea region; the solid black line represents the trace of the profile shown in Fig. 9b; b) topographic profile extracted from the ETOPO2022 global elevation model. Along the same trace the flexural uplift and the filtered topographies at 200 and 400 km (Figs. 7a, b) have been extracted for comparison. (For interpretation of the references to colour in this figure legend, the reader is referred to the web version of this article.)

(2024); it shows positive anomalies (0–2000 m) concentrated in eastern Africa and along the Red Sea and the western portion of the Arabia Peninsula. The highest values (>2000 m) characterize the Main Ethiopian Rift, the southwestern portion of the Arabian Peninsula, and the Red Sea. Values between 0 and 2000 m are found to the west of the Nile River, in the central portion of the Arabian Peninsula, and in the western and central sectors of Anatolia. Negative values appear along the Mesopotamian Basin and the Persian Gulf area (−3000–0 m), in coincidence

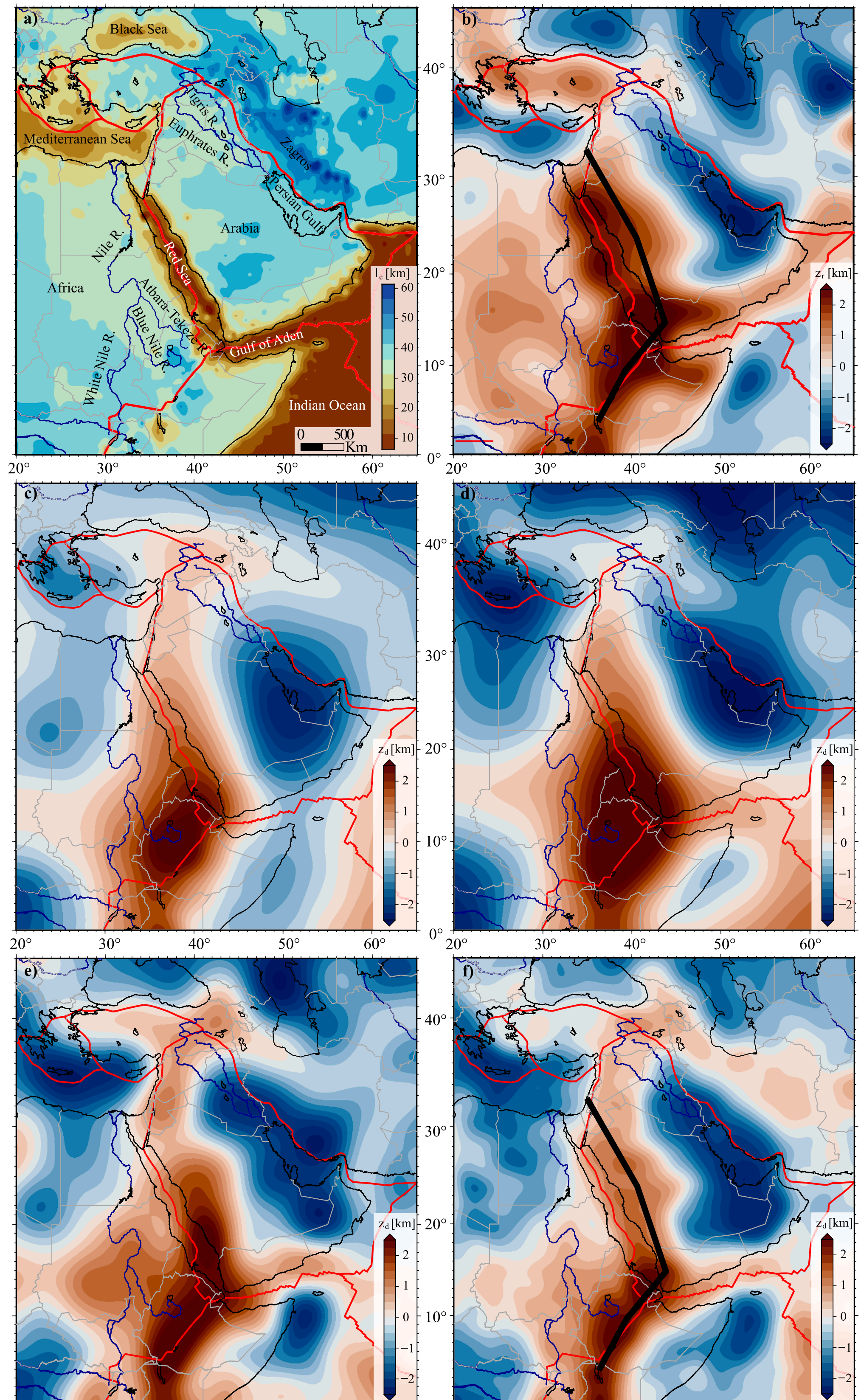

Fig. 10. a) Moho map based on a merger of CRUST1 (Laske et al., 2013) with constraints from regional studies (e.g. compiled in Gvirtzman et al., 2016), as in Faccenna and Becker (2020), but updated to also include the database of Boyce et al. (2023). b) residual topography based on crustal thickness and density variations, computed as in Faccenna and Becker (2020), but using a smoothed version of the new Moho map in a); c-e) dynamic topography based on mantle flow driven by scaling anomalies from TX2019 (c), SAVANI (d), SL2013 (e), and REVEAL (f, cf. Fig. 5), i.e. the seismic tomography models shown in Fig. 2. Residual and dynamic

topography computations follow Becker et al. (2014) and Faccenna and Becker (2020) but the wave speed anomaly to density scaling factors is reduced by 0.7 for models e) and f). The thick solid black line in b) and f) indicates the trace of profile represented in Fig. 13.

of the Zagros-Bitlis mountain belt (−1000–0 m), in the eastern sector of the Mediterranean Sea comprising the Nile River delta area (−1500–0 m), and in the western portion of the Indian Ocean (−1500–0 m), where we have not corrected for the effects of seafloor age dependent half-space cooling.

We can compare this lithospheric based estimate of anomalous residual topography with what deflections of the surface might be caused by mantle flow. At long wavelengths which allow ignoring flexural effects, those two anomalous topography estimates should match, assuming perfect knowledge of structure, density anomalies, and transport properties (see, e.g., discussion in Becker et al., 2014). We compute dynamic topography from a simplified, global mantle flow model with only radial viscosity variations by converting radial stresses to equivalent topography (e.g., Panasyuk and Hager, 2000), following the approach of Becker et al. (2014). On long wavelengths, this is a good approximation to the effects of mantle flow since dynamic topography of the surface is primarily sensitive to density anomalies in the uppermost mantle (e.g., Panasyuk and Hager, 2000), with only minor modifications due to lateral viscosity variations (e.g. Becker et al., 2014). Density anomalies are inferred by scaling seismic tomography with a constant scaling factor for all depths below 100 km, following Faccenna and Becker (2020), for simplicity. The seismic tomography models we use are, as in Fig. 2, TX2019 by Lu et al. (2019) (Fig. 10c), SAVANI by Auer et al. (2014) (Fig. 10d), SL2013 by Schaeffer and Lebedev (2013) (Fig. 10e), and REVEAL by Thrastarson et al. (2024) (Fig. 10f). Shear wave anomalies of models SL2013 and REVEAL have higher RMS than TX2019 or SAVANI and were scaled down by a factor of 0.7 to make overall anomalies comparable, sidestepping the general, unresolved issues of uncertain mineral physics scaling and uneven and model-dependent seismological anomaly recovery.

We therefore focus more on pattern than amplitudes, and the dynamic topography predictions based on the more recent, higher resolution models (Figs. 10e, f) indicate similar patterns to the residual topography one, implying that there is indeed a significant contribution from mantle processes to the non-isostatic, anomalous parts of topography. Moreover, comparison of the averaged shear wave velocity structure of Fig. 5 with the actual dynamic topography from flow prediction of the same model (Fig. 10f) highlights the aforementioned upper mantle density anomaly control of dynamic topography.

Positive values are concentrated along a roughly S—N trending strip from Ethiopia to Anatolia. The largest dynamic topography anomalies are found in part of Ethiopia, Eritrea, Djibouti, and Yemen. Positive anomalies up to 2000 m cover most of Sudan, the Red Sea, the western portion of the Arabian Peninsula, and the Middle East, up to Anatolia (Figs. 10c, d, e, f). Negative anomalies characterize the Somalian coast of Indian Ocean, northern Africa, eastern Mediterranean, and the Mesopotamian Basin-Persian Gulf area. This updated analysis broadly confirms earlier inferences (e.g. Daradich et al., 2003; Moucha and Forte, 2011; Chen et al., 2015; Faccenna and Becker, 2020), but Fig. 10 indicates an encouraging, improved regional match of residual and dynamic topography patterns.

The region represented in Fig. 10 is drained by two main drainage system: the Nile and the Euphrates-Tigris ones. The Nile River network is characterized by three main trunks: the White Nile, the Blue Nile, and the Atbara-Tekeze. While the first joined the main river network only in the Late Pleistocene (Williams, 2019), the Blue Nile and the Atbara-Tekeze rivers have a long history started at least in the Oligocene (Pik et al., 2003; Sembroni et al., 2016a; Faccenna et al., 2019; Sembroni et al., 2021). Indeed, geological and geophysical data (Garzanti et al., 2006; Padoan et al., 2011; Sembroni et al., 2016a; Faccenna et al., 2019) suggest that the deep mantle processes related to the upwelling of the Afar superplume created a stable topographic gradient which made the Blue Nile and the Atbara-Tekeze rivers stably connected to the Nile since at least 30 Ma.

Similarly, data from fluvial terraces (Demir et al., 2007; Stow et al., 2020) constrain the first appearance of the Euphrates River at the middle Miocene when the river flowed into the sea in southern Turkey. Successively, due to the regional uplift, the coast has shifted successively to the southeast resulting in the current path of the river (Demir et al., 2007; Stow et al., 2020). Demir et al. (2008), considering ~270 m of incision since the early Late Miocene (~9 Ma), estimated ~600 m of surface uplift on this timescale.

Plotting the drainage network on Fig. 10 we note that the Blue Nile-Atbara and the Euphrates-Tigris river networks source from areas of high positive residual and dynamic topographies (respectively the Ethiopian and the Eastern Anatolian plateaux) and end in regions of very low negative values (respectively the eastern Mediterranean Sea and the Persian Gulf).

Moreover, the area occupied by the swell (see Figs. 7 and 8) is characterized by the lowest values of lithosphere thickness in the region (Gvirtzman et al., 2016; cf. Fig. 2) and the highest residual and dynamic topographies (Fig. 10). P- (Benoit et al., 2006a; Hansen et al., 2012; Wei et al., 2019; Boyce et al., 2021, 2023) and S-wave (Benoit et al., 2006b; Priestley et al., 2008; Chang and Van der Lee, 2011; Schaeffer and Lebedev, 2013; Auer et al., 2014; Chen et al., 2015; Lu et al., 2019; Thrastarson et al., 2024) tomography indicates a low velocity anomaly at depths between 110 km and 300 km (Fig. 2). Moreover, the estimation of gravity effect of sediments all over the area results in a negative gravity anomaly region coinciding with the swell (Chen et al., 2015).

5.5. *The geometry of the swell top surface*

Previous studies demonstrated that during the Oligocene, several portions of the study area were characterized by low-relief surfaces which at present cover an area comprised of Ethiopia and the Levant (Coltorti et al., 2007; Gani et al., 2007; Avni et al., 2012; Bar et al., 2016; Sembroni et al., 2016a, 2016b; Sembroni and Molin, 2018; Sembroni et al., 2021). These surfaces are different in origin: the Levant and western Arabia ones are part of a wide planation surface separating the late Eocene – early Oligocene sediments from the late Oligocene - Holocene deposits (Avni et al., 2012; Bar et al., 2016) while the eastern Africa surface represents the top of the Oligocene basaltic plateau emplaced during or immediately after the impingement of the Afar superplume (Sembroni et al., 2021; Ebinger et al., 2024). At present, the surfaces stand at an elevation between 800 m (northern portion of the study area) and 2700 m (southern part).

To reconstruct the envelope of these surfaces, we mapped all the surfaces remnants by a spatial query in an ArcGIS environment (Fig. S1a). All surfaces with a slope lower than 3° and standing at an elevation ranging between 800 and 1200 m in the Arabian Peninsula and between 1000 and 2700 m in the Horn of Africa have been isolated (Fig. S1a). The surfaces have been then interpolated as a triangulated irregular network (TIN; Fig. S1b) and then smoothed by a circular low pass filter 100 km in radius to remove the artifacts related to the triangulation algorithm.

The result shows a surface whose trend changes from NE-SW in the southern portion to NNW-SSE in the northern one (Fig. 11). The elevation gradually decreases from south (2500 m) to north (900 m) for a total distance of ~4000 km from Ethiopia to Jordan. In Fig. 12 some images taken from Google Earth show examples of portions of the surface. This feature occupies the same region characterized by negative gravity anomaly (Chen et al., 2015), by P- and S-wave low velocity anomaly (Kendall et al., 2005; Benoit et al., 2006a, 2006b; Priestley et al., 2008; Bastow et al., 2010; Chang and Van der Lee, 2011; Hansen

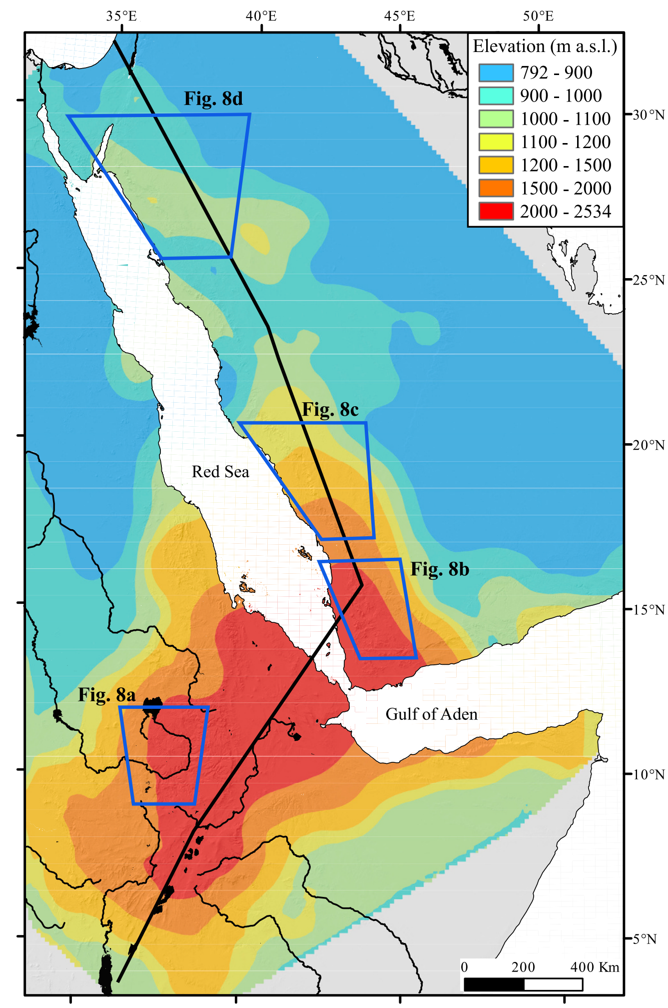

Fig. 11. a) The top surface of the East African-Arabia swell obtained by interpolating the isochronous high-standing surfaces mapped between Ethiopia and Jordan. The thick solid black line indicates the trace of the profile represented in Fig. 13.

et al., 2012; Schaeffer and Lebedev, 2013; Auer et al., 2014; Chen et al., 2015; Lu et al., 2019; Reiss et al., 2019; Wei et al., 2019; Chang et al., 2020; Hosseini et al., 2020; Andriampenomanana et al., 2021; Boyce et al., 2021, 2023; Saeidi et al., 2023; Ebinger et al., 2024; Thrastarson et al., 2024; Fig. 2), and by high residual and dynamic topographies (Fig. 10).

Lastly, to compare the geometry of the swell top surface with the trend of the filtered, residual, and dynamic topographies a profile for each has been extracted by using the same trace represented in Figs. 7b, 10b, f, and 11 (Fig. 13). The swell top surface profile matches quite well the residual and dynamic topographies. The same decreasing trend, even if with lower values, characterizes filtered topography at 400 km where the minimum at ~1250 km coincides with the Gulf of Aden-Red Sea rift system whose signal cannot be detected in the swell top surface. In summary, all the considered topographies show a decreasing trend from south to north with maximum values concentrated in the area comprising Ethiopia, Eritrea, Djibouti, and Yemen (Fig. 13).

5.6. *The distribution and age of volcanic deposits*

Since the Eocene, the study area was affected by widespread volcanism. To investigate the distribution and a possible age pattern of volcanic deposits, a compilation of 1465 volcanic samples has been analyzed expanding the databases previously published (Camp and Roobol, 1992; Bosworth and Stockli, 2016; Civiero et al., 2022; Hua et al., 2023; Fig. 14; see supplementary material for references – Table S2). Each sample is classified according to the country where it was sampled and the database has been cleared of all those deposits whose geochemical analyses showed a clear derivation from subduction processes (the “orogenic” deposits of Lustrino and Wilson, 2007). The study area has been divided into two parts: the southern portion (Ethiopia, Djibouti, Yemen, Saudi Arabia; Fig. 15a) and the northern one (Egypt, Israel, Jordan, Syria, Turkey; Fig. 15b).

The age frequency plots for both areas show a roughly bimodal distribution in accordance with previous studies (Camp and Roobol, 1992; Bosworth and Stockli, 2016; Civiero et al., 2022; Figs. 15a, b). In particular, the southern area presents the age ranges of 18–42 Ma and 0–16 Ma with peaks comprised between 28 and 32 Ma and 0 and 4 Ma respectively (Fig. 15a). These two ranges are separated by a brief period (16–17 Ma) of low volcanic activity well documented all over Saudi Arabia (Camp and Roobol, 1992; Bosworth and Stockli, 2016). In general, Ethiopia and Saudi Arabia are characterized by a quasi-continuous volcanic activity, while the ages of volcanic deposits in Yemen and Djibouti are comprised only between 32 and 20 Ma and 0 and 4 Ma, respectively (Fig. 15a).

In the northern area the bimodal distribution is shifted toward younger ages (Fig. 15b). In detail, the first range falls between 10 and 22 Ma while the second one is comprised between 0 and 8 Ma, with a remaining small number of samples with older ages (Fig. 15b). In contrast to the southern area, here the two ranges are separated by a sharp decrease in number of samples with ages comprised between 8 and 10 Ma. In general, except for Egypt, whose volcanic deposits ages vary between 18 and 32 Ma, in the remaining countries the volcanism is overall continuous (Fig. 15b).

The presence of young volcanic deposits in both areas may be in part because such deposits, outcropping at or near the surface, could cover the older ones. To investigate a possible pattern of volcanics age from the southern to the northern portions, the age data have been plotted against latitude following the example of previous studies (e.g., Bosworth et al., 2005; Bosworth and Stockli, 2016; Boone et al., 2021; Civiero et al., 2022). The result indicates a decrease in the maximum age of volcanic deposits from Ethiopia to Turkey with a plateau in coincidence with the Saudi Arabia data (Fig. 15c). By plotting on the same graph, the curve of filtered topography at 400 km extracted along the axis of the EAAS (Figs. 7b), it is possible to see a similar trend (excluding the Red Sea minimum) with elevation decreasing from ~1700 m in Ethiopia to less than zero in Jordan.

6. Discussion

The EAA swell covers the region from Ethiopia to Jordan crossing the Gulf of Aden and the Red Sea. Its configuration consists of a NNW-SSE trending ridge with amplitude and height decreasing from south to north. Most of volcanoes and basaltic lava fields are located along its axis. In general, the ridge appears asymmetric with respect to the Red Sea. This is possibly related to crustal thickening due to magmatic underplating as indicated by recent geophysical analysis in the central portion of the Arabian margin of the Red Sea which evidenced the presence of a magmatic body in the lower crust atop an underplated Moho (Mukhopadhyay et al., 2023). That portion is characterized at the surface by large volcanoes and basaltic lava fields dated between Tertiary and Quaternary (Coleman et al., 1983; Camp and Roobol, 1992). This configuration appears similar to the Main Ethiopian Rift one where the rift opened immediately to the east of the Ethiopian Plateau affected by a strong underplating during the Trap phase (Rooney, 2017), as evidenced by seismic refraction and receiver function data (Mackenzie et al., 2005; Tiberi et al., 2005).

The continuity of the swell is interrupted to the north in coincidence with the Mesopotamian Basin, considered as the foreland basin of the Bitlis-Zagros mountain belt. Here, a wide depression extending from

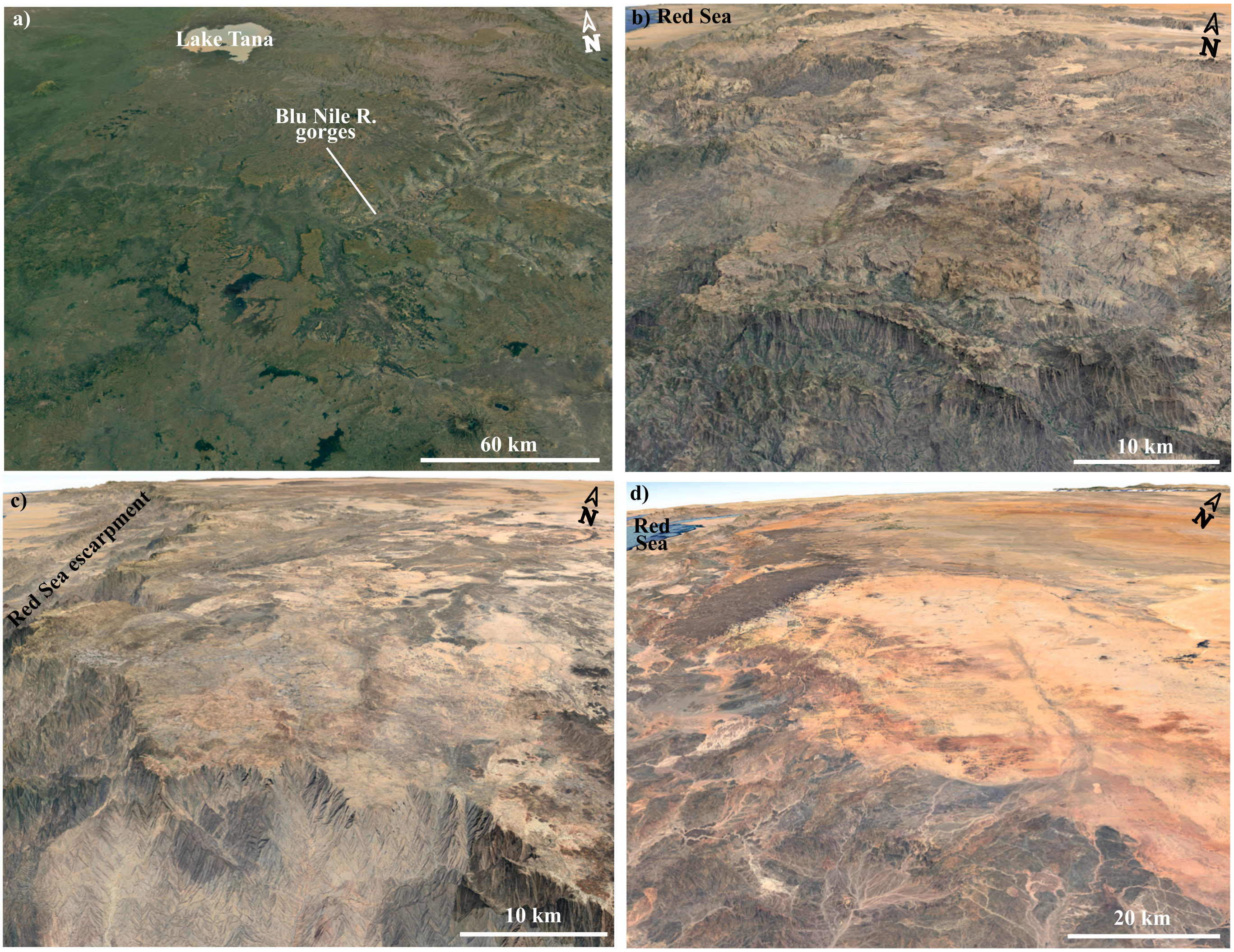

Fig. 12. Images from Google Earth showing portions of the Oligocene surface from Ethiopia (a), Yemen (b), western Saudi Arabia (c), and northern Saudi Arabia (d). Note the low-relief top surfaces in all figures which represent portions of the swell top surface. See Fig. 11 for the exact location.

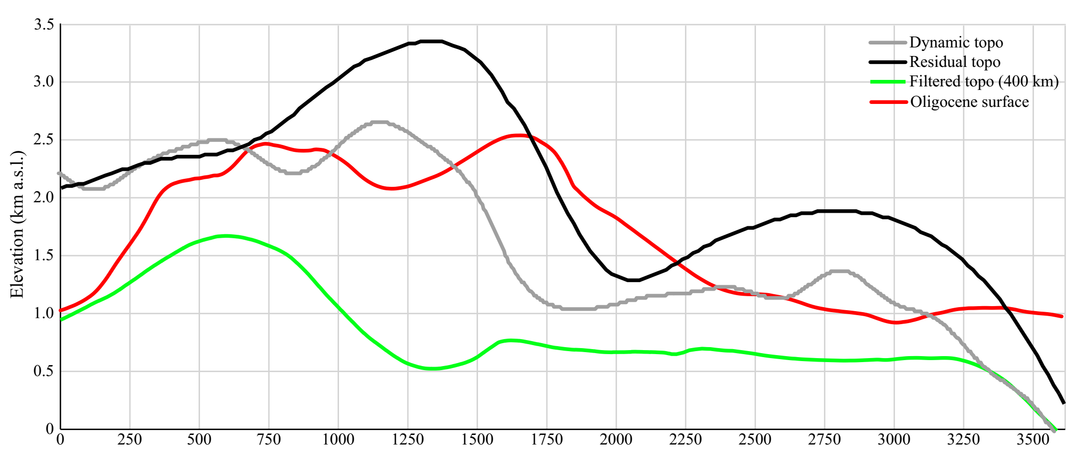

Fig. 13. Plot showing the trends of dynamic, residual, and filtered topographies (400 km) with respect to the Oligocene swell top surface along the solid black line drawn in Figs. 7b, 10b, f, and 11.

Syria to the Persian Gulf may be related to the depression of the lithosphere by subduction of the basement of the Arabian plate under the sedimentary rocks of the same plate (e.g., Yeats, 2012). This seems confirmed by the maps of dynamic topography (Figs. 10c, d, e,f) which, in accordance with previous studies (Gvirtzman et al., 2016; Steinberger, 2016; Faccenna et al., 2019; Steinberger et al., 2019; Lu et al.,

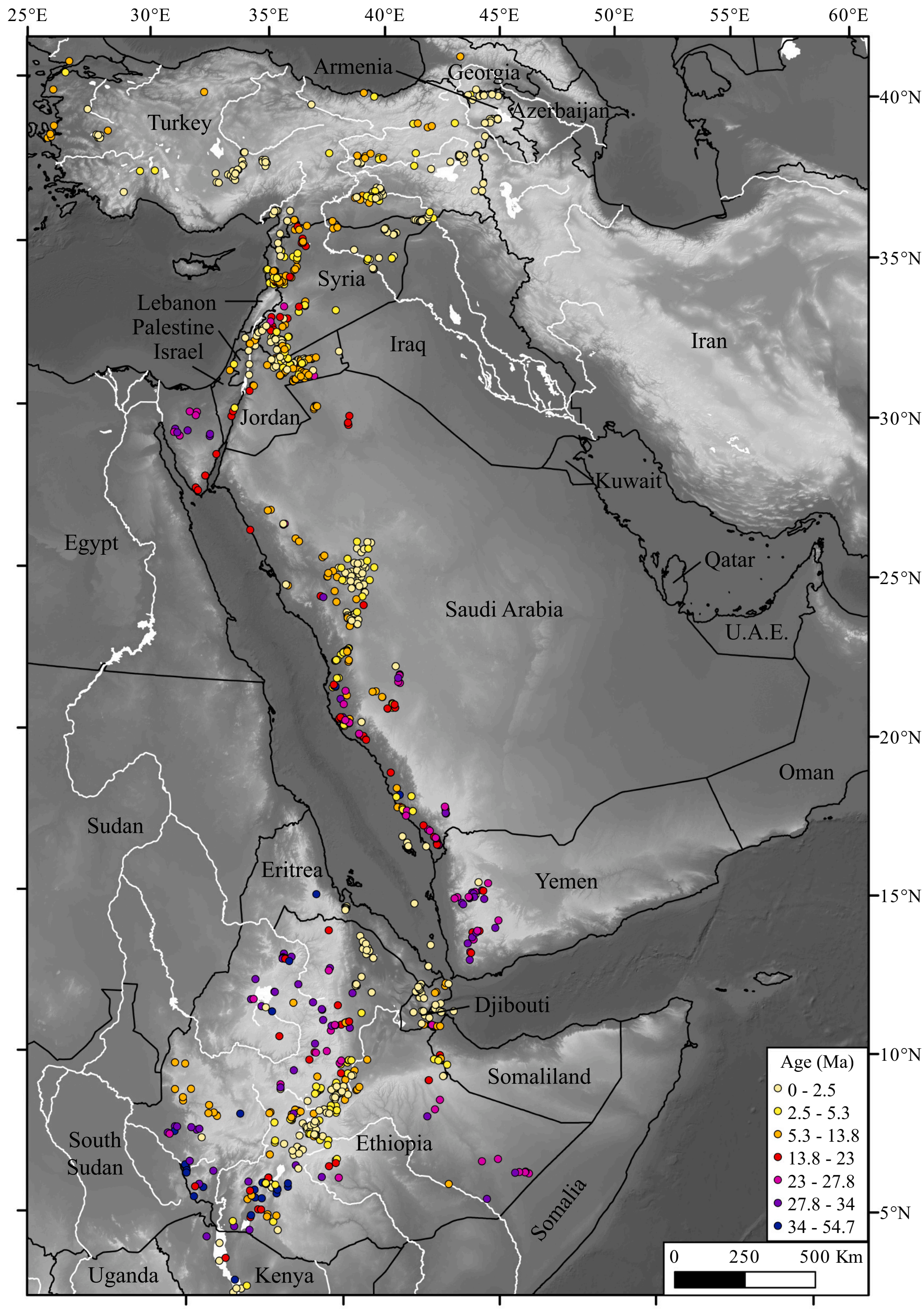

Fig. 14. Distribution of volcanic deposits along the study area distinguished by age.

2019), indicates negative values in the area. To the northwest, the swell is bounded by the easternmost portion of the Mediterranean basin characterized by negative values in filtered topography (Figs. 7a, b). As for the case of the Mesopotamian Basin, this area presents negative dynamic topography (Figs. 10c, d, e,f) related to the depression of the lithosphere induced by slab sinkers (Forte et al., 2010; Gvirtzman et al., 2016; Steinberger, 2016; Faccenna et al., 2019; Steinberger et al., 2019; Lu et al., 2019).

The incision (local relief) is low both on the top and on the flanks of the swell with the exception of the areas close to the Red Sea and Main

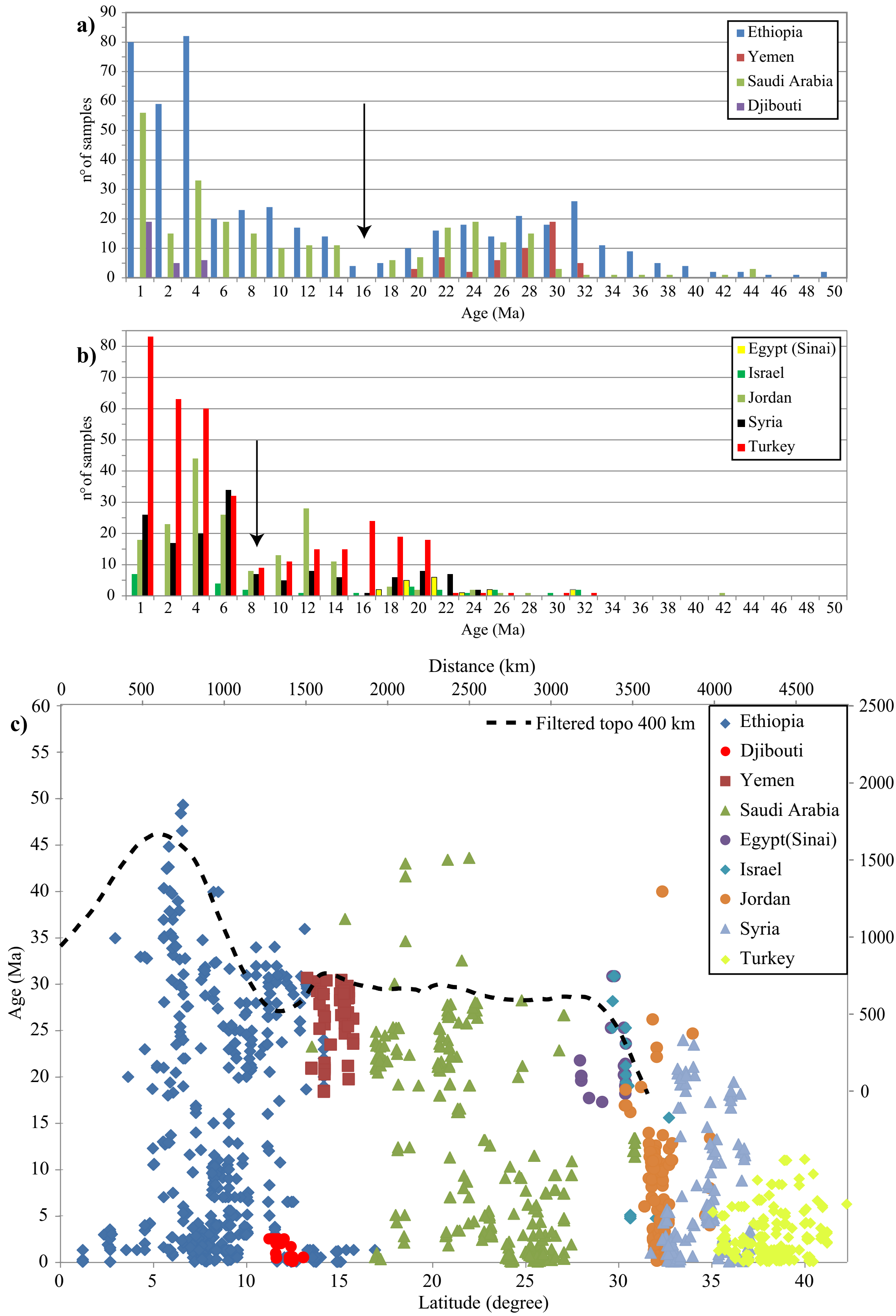

Fig. 15. a-b) Frequency plots of the volcanic deposits outcropping along the study area according to their ages; both plots show a bimodal distribution characterized by a marked minimum at 16–17 Ma in Fig. 15a and at 8–9 Ma in Fig. 15b; c) Distribution of the ages of the volcanic deposits according to latitude. Superimposed on the graph, the curve of the filtered topography at 400 km (the trace is shown in Fig. 7b) has been represented for comparison.

Ethiopian rift shoulders, where the highest values are related to the flexural uplift (Weissel et al., 1995; Sembroni et al., 2016a; Stüwe et al., 2022; Fig. S2), and the Ethiopian Plateau, because of the strong fluvial incision (Sembroni et al., 2016b, 2021; Fig. S2). The elastic thickness values obtained (Table S1) together with published seismic tomography data (Priestley et al., 2008; Chang and Van der Lee, 2011; Hansen et al., 2012; Chen et al., 2015) well correlate with the topographic pattern of the region and point to a mantle supported uplift (Chen et al., 2015). The feedback between erosion and seafloor spreading in the Red Sea area (Stüwe et al., 2022) could have enhanced the flexural uplift at the Red Sea margins inhibiting the capture of the swell top surface by rivers draining the inner part of the Red Sea shoulders. Portions of this surface has been locally studied in the past (Coltorti et al., 2007; Gani et al., 2007; Avni et al., 2012; Bar et al., 2016; Sembroni et al., 2016a, 2016b; Sembroni and Molin, 2018; Sembroni et al., 2021), but the topographic analysis performed here allows designating different fragments. They are located roughly along the axis of the swell ridge at an elevation between 800 m, in the north, and 2700 m, in the south (Fig. S1). The overall elevation pattern and geometry of the surface resembles the filtered, residual, and dynamic topographies (Figs. 7a, b and 10b, f). In turn, the filtered topography at 200 km approximates the present topography except for the Red Sea margins where the flexural component is dominant (Figs. 8 and 9). This suggests that the swell top surface and part of the present topography of the study area can be related to mantle processes (Sengör, 2001; Daradich et al., 2003; Forte et al., 2010; Moucha and Forte, 2011; Faccenna et al., 2013).

Recent studies on the uplift history of the Ethiopian-Somalian and Yemen plateaux (Sembroni et al., 2016a; Faccenna et al., 2019; Sembroni et al., 2021) and the Jordan plateau (Bar et al., 2016) show that the southern portion of the swell (Horn of Africa) in the lower Oligocene was at elevations very close to those currently shown by the swell top surface, while the northern one (Levant region) reached the elevation of ~1000 m (the average elevation of the swell top surface in this region) at the end of upper Miocene (Fig. 16). This means that the bulk of the uplift in most of the study area occurred between the Oligocene and Miocene and that the present topography is very similar to the one reached in that period, partly modified by surface erosion, flood basalt emplacement, and flexural uplift along the Red Sea and MER margins. This is also confirmed by thermochronology data showing a rapid and significant exhumation phase during that period (Boone et al., 2021; Lanari et al., 2023) with rates between 0.1 and 0.3 mm/yr in the northern portion of the Red Sea (Lanari et al., 2023).

The opening of the Red Sea begun in its southernmost portion between the end of the Oligocene and the beginning of the Miocene (Boone et al., 2021, and references therein). This would relate, at least temporally, this event to the deep process underlying the formation of the swell but does not allow to define with certainty whether the same process also caused the opening of the Red Sea. Several studies (McQuarrie et al., 2003; Bellahsen et al., 2003; Bosworth et al., 2005; Koptev et al., 2018; Khalil et al., 2020) agree that the Red Sea and the Gulf of Aden rifts were mainly driven by slab pull occurred along the Bitlis-Zagros subduction front, with plume-related magmatism acting to generate extension in the Afar and Red Sea.

However, the thermo-mechanical weakening of the lithosphere related to plume impingement together with pre-existing lithospheric heterogeneities seem to have played a role in rift evolution (e.g., Koptev

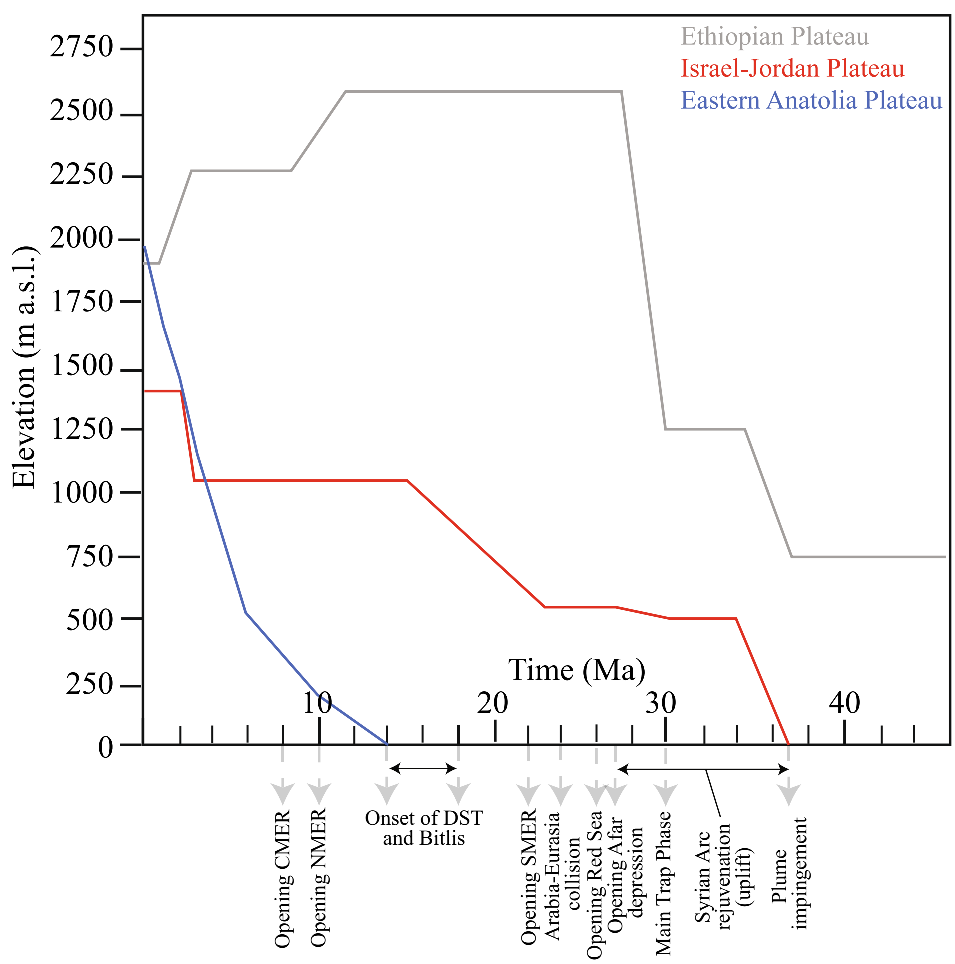

Fig. 16. Uplift histories of the Ethiopian, Jordan, and Eastern Anatolian plateaux according to recent studies (respectively Faccenna et al., 2019; Bar et al., 2016; Molin et al., 2023).

et al., 2018; Khalil et al., 2020). The analysis of flexural uplift along the Red Sea margins confirms the progressive northwards opening of the rift with an uplift increasing from north to south (Fig. 9a and Table S1). The greatest elevations (w_0) and wavelength (α) were found on the Arabian plate. Despite the high values (see Table S1), the flexural uplift marginally influenced the topographic configuration of the EAAS since its effect becomes close to zero at a maximum distance of ~250 km from the Red Sea margins (Fig. 9a). The same analysis performed in the Main Ethiopian Rift area suggests again a southward increase in flexural uplift (from 500 to 1200 m) with maximum wavelength of ~200 km from the rift shoulders (Weissel et al., 1995; Sembroni et al., 2016a).

The comparison between flexural uplift data and filtered topographies in the Red Sea region (Fig. 9b) clearly shows how the topography in this area is the result of the interaction between shallower (flexural uplift) and deeper (mantle plume) processes. Indeed, the topographic profile across the Red Sea presents neither a pattern typical of a rift margin subjected to flexural unloading (green curve in Fig. 9b) nor that of an area characterized by bulging due to rising hot mantle material (blue curve in Fig. 9b) but something in between: for the first 200 km the green curve is what best approximates the topography; beyond that distance the profile follows the blue curve.

Like topography and flexural uplift, the areal distribution of volcanism shows a marked asymmetry as much in the Horn of Africa as in the Arabian Peninsula (Fig. 14). Our analysis reveals that in the Horn of Africa most of the volcanic deposits outcrop to the west of the Main Ethiopian Rift (cf. Sembroni et al., 2016a). Conversely, in the Arabian Peninsula, most of volcanic fields follows the axis of the EAAS to the E of the Red Sea (Fig. 14). Along the strike of this axis, from Ethiopia to Turkey, there is an overall decrease in the age of volcanics and a parallel decrease in topography (Fig. 15c). This implies that a single main mantle upwelling is sufficient to explain the present topographic configuration and the chronology of volcanic deposits, as seismic tomography and geochemical data seem to confirm (Priestley et al., 2008; Hansen et al., 2012; Faccenna et al., 2013; Schaeffer and Lebedev, 2013; Auer et al., 2014; Gvirtzman et al., 2016; Lu et al., 2019; Thrastarson et al., 2024). If, as claimed in some studies (e.g., Chang and Van der Lee, 2011; Koulakov et al., 2016; Chang et al., 2020), there were more sources of volcanism (more arrivals of hot mantle material) or there was a different path, both the topography and volcanics age distribution would likely show a more irregular pattern. However, the concomitance of other local processes underlying Arabian volcanism cannot be ruled out. For example, the recent volcanism (< 12 Ma) in southwestern Arabia has been speculated to be related to decompression melting in the mantle lithosphere caused by flexural uplift (Stüwe et al., 2022).

The appearance of magmatism below the Arabian Peninsula seems to be spread over a very large area. This would imply the presence of a very low-viscosity asthenosphere as seems to be confirmed by seismic, petrological, and geochemical data (Hua et al., 2023).

The ages of the volcanic deposits are progressively younger toward the north, some of which may be due to younger deposits partly or completely covering older ones. Despite this limitation, the frequency of volcanic deposits ages shows a bimodal trend with a brief period (few millions of years) of partial quiescence characterized by few events (Fig. 15a, b). On the Arabian plate, the areal distribution of volcanics before and after this time span shows a marked change. In particular, the old volcanics were emplaced along NW-SE dikes inherited from Precambrian tectonic lineaments (Najd Fault System; Johnson et al., 2017 and references therein). Conversely, the new volcanic centers are aligned N-S (Fig. 14). The age of the partial quiescence shifts to younger ages from south (16–18 Ma) to north (8–10 Ma; Fig. 15a, b). The older quiescence period is coincident with the advanced stage of the Arabia-Eurasia collision at the Bitlis collision zone (18–14 Ma – Okay et al., 2010; Ballato et al., 2011; Cavazza et al., 2018, 2019; Gusmeo et al., 2021; Darin and Umhoefer, 2022) and the activation of the Dead Sea transform fault (17–20 Ma – Quennell, 1958; Freund et al., 1970; Garfunkel, 1981; Garfunkel et al., 1981; Joffe and Garfunkel, 1987; Bosworth et al., 2005; Nuriel et al., 2017). These processes caused the counterclockwise rotation of the Arabian plate and the change in the direction of maximum compression (at the Bitlis-Zagros front) and extension (in the Red Sea and Gulf of Aden) from NE-SW to N-S (Boone et al., 2021, and references therein). This may have caused the closure of the NW-SE Precambrian lineaments and the opening of new N-S lineaments as was already proposed in the case of the Harrat Ash Shaam in Syria (Al Kwatli et al., 2012).

The pause and renewal of volcanism in the study area are followed, respectively, by increases and decreases in the number of mammal evolution lineages (de Vries et al., 2021). Although de Vries et al. (2021) cite also the climate factor as a contributing cause, the close correlation between volcanism pauses and renewal and the mammal evolution lineages trend, makes the geological factor predominant as already demonstrated in other parts of the world (e.g., Deccan and Siberia; Prave et al., 2016; Ernst and Youbi, 2017).

In summary, the present topography of the region spanning from Ethiopia to Syria shows an elongated ridge with a roughly NNW-SSE direction. It originates in Ethiopia, where it presents the greatest elevations and amplitude, and extends mainly into the Arabian plate with decreasing elevation and amplitude toward the north. The ridge is well described by the Oligocene low-relief surfaces and by the trend of filtered (200 and 400 km), residual, and dynamic topographies (Figs. 7, 10, 11). The same area has lower lithospheric thickness and higher residual and dynamic topographies respect to the surroundings and has negative P- and S-wave velocity and gravity anomalies (Fig. 10; Benoit et al., 2006a, 2006b; Priestley et al., 2008; Chang and Van der Lee, 2011; Hansen et al., 2012; Schaeffer and Lebedev, 2013; Auer et al., 2014; Chen et al., 2015; Gvirtzman et al., 2016; Lu et al., 2019; Boyce et al., 2021, 2023; Ebinger et al., 2024; Thrastarson et al., 2024). The decrease of filtered topography from Ethiopia to Syria is very similar to the trend of the volcanic deposits age, decreasing from south to north. All these data indicate the presence of a main single process which sculpted the past and present topographic configuration of the area. This process, having a wavelength of >200 km, is likely subcrustal as it exceeds flexural wavelengths. As already stated in the previous works on the study area (Faccenna et al., 2013; Gvirtzman et al., 2016; Agostini et al., 2021; Hua et al., 2023) this deep seated process may be identified with the upwelling of the Afar Superplume below the Ethiopian lithosphere that, taking advantage of prior discontinuities and/or pression gradients, channeled to the Levant region in a few million years causing the tilting to the SE of the Arabian Peninsula discussed in several studies (Sengör, 2001; Daradich et al., 2003). The northward progression of plume induced flow as discussed by Faccenna et al. (2013) is also broadly consistent with time dependent mantle convection reconstructions for the region (e.g. Moucha and Forte, 2011; Faccenna et al., 2019; Straume et al., 2024).

According to geological data (Avni et al., 2012; Bar et al., 2016) the planation surface detected between the southern Levant area and the northern Red Sea region can be dated at the Oligocene. However, the region rose from 500 m to 1000 m elevation only at the end of upper Miocene (Bar et al., 2016; Fig. 16). This means that the arrival of the superplume in this sector may be placed at the beginning of the Miocene (Fig. 16). If this is correct, the tilting of Arabia can be placed between the impingement of the plume beneath Ethiopia (Late Eocene; Ebinger and Sleep, 1998; Sengör, 2001; Ebinger et al., 2024) and the arrival of the same plume in the Levant region (upper Miocene). This is confirmed by stratigraphic data which indicate a strong subaerial erosion phase throughout the Arabian Peninsula between the end of Paleogene and the beginning of the Neogene, immediately after a long transgression phase which established shallow marine condition over eastern Arabia since early Paleocene (Alsharhan and Nairn, 1995; Sengör, 2001; Ziegler, 2001). This phase generated an unconformity between the Paleocene and Miocene sediments and the shifting of the eastern Arabia coastline by >500 km to the northeast (Alsharhan and Nairn, 1995; Ziegler, 2001; Fig. 17). Looking at the coastline reconstruction of the eastern sector of

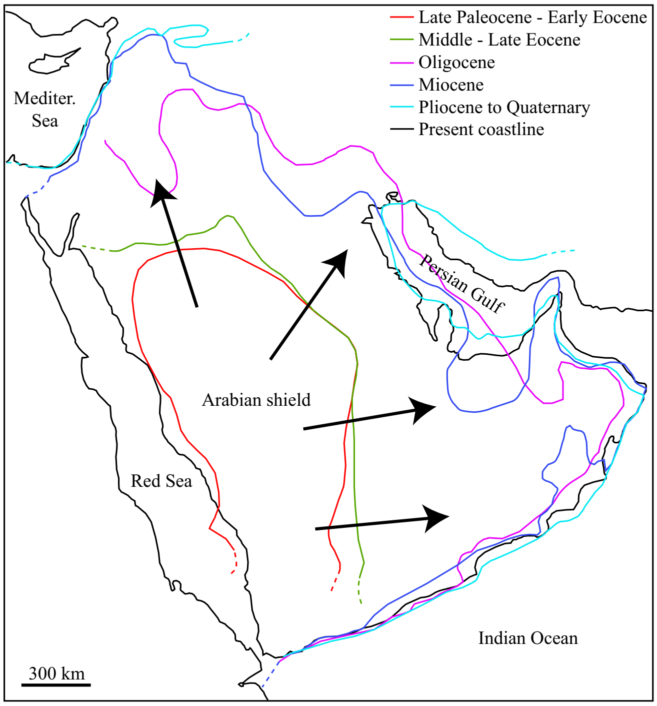

Fig. 17. Map showing the migration of the eastern Arabia coastline from Late Paleocene to Quaternary (modified after Alsharhan and Nairn, 1995 and Ziegler, 2001).

Arabia (Fig. 17), it is interesting to note that the northeastward shift appears to be parallel to the swell axis (Figs. 7, 8, 11). This suggests a direct involvement of the northward passage of the superplume in the coastline migration (cf. Straume et al., 2024). The presence of a new relief in the western side of Arabia is also confirmed by huge volumes of sands deposited from an easterly flowing river network between late Oligocene and early Miocene in an area comprising Saudi Arabia, Kuwait, and southeastern Iraq (Alsharhan and Nairn, 1995; Ziegler, 2001; Barrier and Vrielynck, 2008).

On the other hand, mantle flow took a longer time to reach Turkey. In fact, in the middle Miocene, the area was still under sea level (Molin et al., 2023 and references therein; Fig. 18). The uplift of Anatolia and in particular of the Eastern Anatolian Plateau is debated. Different models have been proposed: 1) mantle delamination (Göğüş and Pysklywec, 2008; Keskin, 2003; Bartol and Govers, 2014; Kounoudis et al., 2020); 2) slab break-off (Bottrill et al., 2012; Faccenna et al., 2006; Keskin, 2003; Schildgen et al., 2014); 3) mantle asthenosphere support (Faccenna et al., 2013; Keskin, 2007; Şengül Uluocak et al., 2021). Recently, Molin et al. (2023) tried to reconcile these three model in a single evolutionary scenario where at ~10–11 Ma the slab break-off drove the formation of a slab window which continued to widen until ~4–5 Ma (Faccenna et al., 2006, 2013; Schildgen et al., 2014). Such a corridor could have allowed the plume to reach the base of the Eastern Anatolian Plateau, as confirmed by the basaltic volcanism mainly Quaternary in age in that area (Figs. 14, 15a, c, 18). Recent upper mantle seismic tomographic models (e.g. Kounoudis et al. 2020), seismic anisotropy studies (e.g. Paul et al., 2014; Merry et al., 2021), and residual topography calculations (e.g. Ogden and Bastow, 2022) seem to confirm the requirement for a mantle contribution to plateau uplift (cf. Straume et al., 2024).

The path of mantle flow throughout the region deeply influenced also the evolution of the main river networks: the Nile and the Euphrates-Tigris drainage systems. Indeed, both river networks source from areas of positive residual and dynamic topographies and have their base level in regions characterized by negative values (Fig. 10). Geological (Garzanti et al., 2006; Padoan et al., 2011; Sembroni et al., 2016a), geophysical (Faccenna et al., 2019, and references therein), and thermochronological data (Pik et al., 2003) indicate that the Nile River establish a connection between the Ethiopian plateau and the Mediterranean since at least Oligocene sustained by the upwelling of the Afar superplume at its source (Faccenna et al., 2019). Similarly, the first appearance of the Euphrates River is dated back to the middle Eocene when the subduction started at the Bitlis front (Okay et al., 2010; Ballato et al., 2011; Cavazza et al., 2018, 2019; Gusmeo et al., 2021; Darin and Umhoefer, 2022) and the whole region passed from marine to continental conditions (Molin et al., 2023, and references therein). The successive evolution of the river with the progressive migration of the coastline to the southeast and the consequent lengthening of the river course could be related partly to the ongoing subduction and partly to the arrival of Afar superplume in the northern Arabia region at late Miocene (Molin et al., 2023).

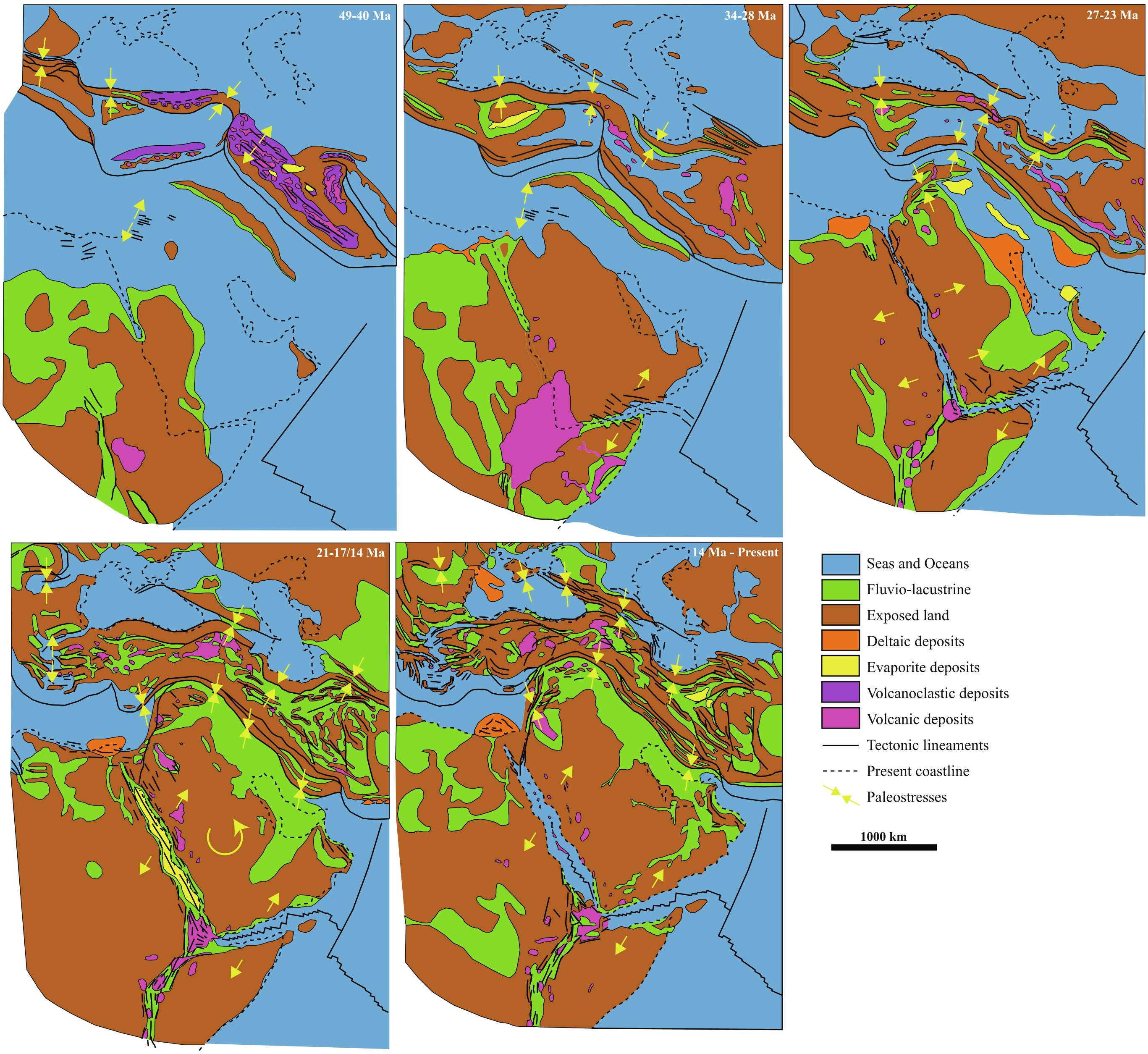

Fig. 18. Tectonic evolution of the study area (modified after Barrier and Vrielynck, 2008).

These data show how mantle processes can sculpt the surface of the Earth over tens of millions of years and support the idea expressed by Faccenna et al. (2019) that long-lived intra-continental rivers dynamics may provide indication of dynamic topography variations.

6.1. Tectonic evolution of the study area

The tectonic evolution of the study area can be summarized as follows (Figs. 18, 19):

45–35 Ma: Plume impingement occurred beneath Ethiopia, causing early uplift and volcanism mainly in southern Ethiopia.

31–29 Ma: Trap basalts are emplaced all over the Horn of Africa and the SW corner of the Arabian Peninsula forming an extended plateau. At about the same time (28–27 Ma) basalts poured out also in the western sector of Saudi Arabia from dikes and volcanoes aligned to Precambrian NW-SE structures. About 2/3 of the mammal fauna in the Afro-Arabia region becomes extinct (de Vries et al., 2021).

27–23 Ma: Volcanism continued in Arabia while a relative pause has been registered in Ethiopia highlands (formation of intratrappean levels; Abbate et al., 2014). Parallel to this pause in volcanism an increase in mammal fauna occurred in the region until about 20 Ma (de Vries et al., 2021). During this time the Oligocene planation surface formed in the Sinai and Levant areas (Avni et al., 2012). The uplift in the Oligocene formed almost all the topography of the Horn of Africa and the SW corner of the Arabian Peninsula. Meanwhile, the Gulf of Aden opened, and the Red Sea began to propagate from south to north (as well as the related flexural uplift as suggested by thermochronology data; Boone et al., 2021, and references therein). The tilting to the SE of the Arabia Peninsula began, testified by a strong erosion phase throughout Arabia and the northeastward shifting of the eastern Arabia coastline (Alsharhan and Nairn, 1995; Ziegler, 2001). An easterly flowing river network carried huge volume of sands eroded from the uplifted western Arabia to the Iraq-Persian Gulf area where a large deltaic system formed.

21–17/14 Ma: At the end of upper Miocene the Levant region experienced strong uplift which increased elevation from 500 to 1000 m (Bar et al., 2016; Fig. 16). Volcanic activity on the Ethiopian-Somalian

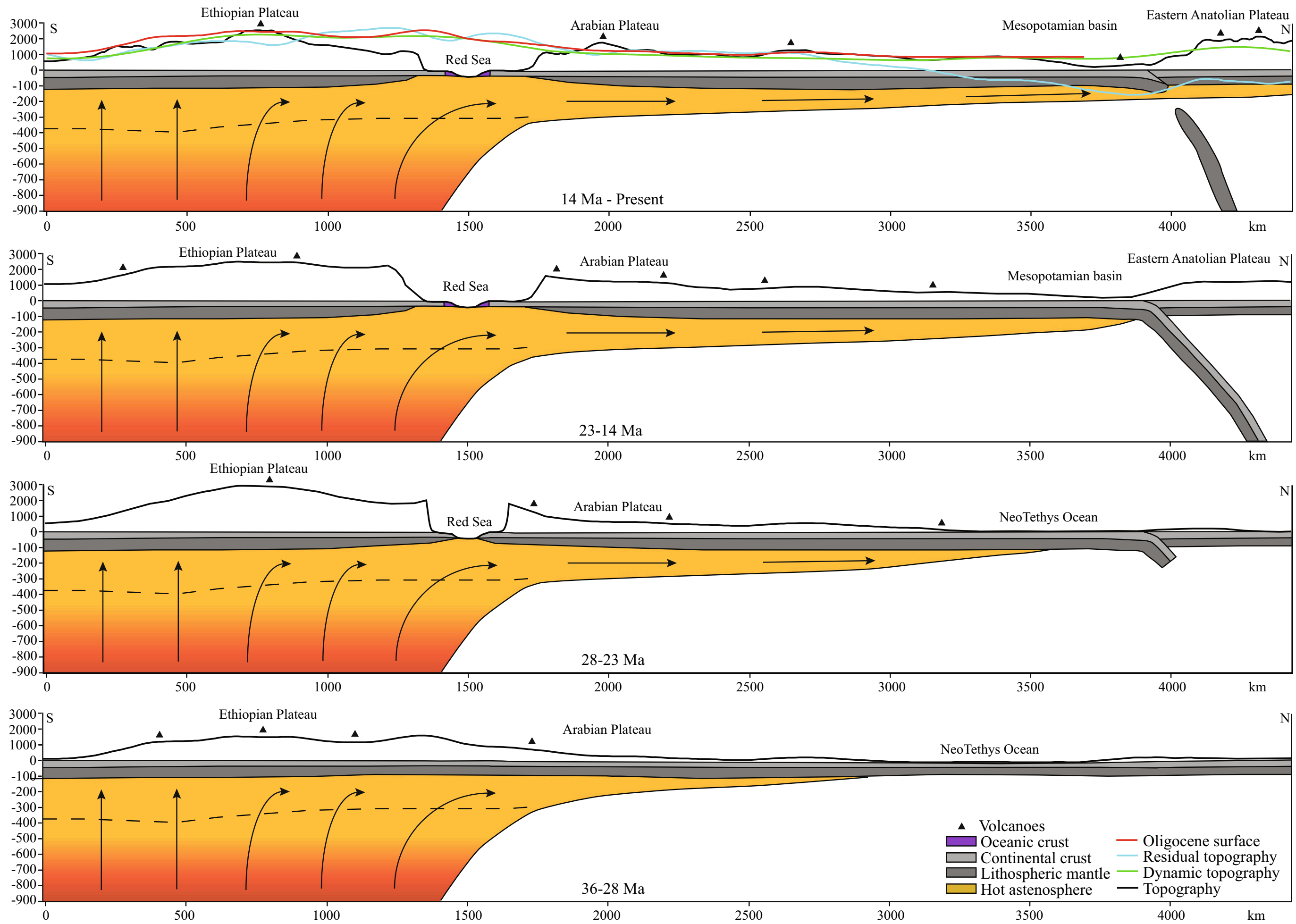

Fig. 19. Topographic evolution of the study area represented along a S—N trending topographic profile from Ethiopia to Eastern Anatolia. Note the lateral migration of the mantle flow and the parallel increase of surface topography (see text for further explanations).

plateau (shield volcanoes) and in the Ethiopian rift started over. In parallel, another dramatic decline in mammals occurred (de Vries et al., 2021). The stress regime changed: the Arabian plate rotates counterclockwise, and the direction of maximum compression becomes ~N-S. At the same time, the Dead Sea Transform Fault developed. A brief pause in volcanism in both Arabia and Horn of Africa occurred in coincidence with this change in the stress regime.

14 Ma-Present: Volcanism resumed in most of the study area. As a demonstration of the change in stress regime, the new volcanic edifices in Arabia are aligned ~N-S. It is at this stage that the most extensive volcanic fields formed in Arabia Peninsula. The eastern portion of Anatolia is strongly uplifted as demonstrated by geological data (passage from marine to continental deposition; Fig. 18), dating of Euphrates R. fluvial terraces (Demir et al., 2007) and river network analysis (Molin et al., 2023).

7. Conclusions

The East Africa - Arabia region has long been studied because of its anomalously high topography, volcanism, and active rifting. There is broad consensus about the role of mantle plumes in generating this high elevation, but the number of plumes and the uplift patterns are debated. We contribute to this discussion by providing an integrative evolutionary model of the region which seeks to integrate the range of constraints we have reviewed here. The main results are the following:

1. The EAA swell is a NNW-SSE trending ridge extending from Ethiopia to Jordan with amplitude and elevation gradually increasing from north (800 km and 800 m) to south (1600 km and 2700 m). Its continuity is interrupted to the south by the Turkana tectonic depression and to the north by the Mesopotamian foredeep basin whose depression may be related to the flexure of the lithosphere by subduction as confirmed by dynamic topography modeling. The area occupied by the swell presents thin lithosphere, high residual and dynamic topography, underlain by low seismic velocity anomalies.
2. The swell top is characterized by low relief surfaces, Oligocene in age, located roughly along the axis. The envelope of these surfaces represents the swell top surface which extends for >4000 km from Ethiopia to Jordan with present elevation decreasing from south (2500 m) to north (900 m).
3. The elevation pattern and geometry of the swell top surface resembles the filtered (200 and 400 km), residual, and dynamic topography, suggesting that the this surface is caused by mantle convective processes. Moreover, the uplift pattern of the southern portion of the swell show that the surface was at elevation close to the present one since the beginning of the lower Oligocene, while in the northern portion it reached ~1000 m at the end of the upper Miocene. Such a shift in uplift histories could match the migration pattern of the mantle plume, and indicates that most of the present topography is mainly the surface expression of mantle plume impingement.
4. The migration of mantle flow from eastern Africa drove the tilting of the Arabian Peninsula between late Eocene and upper Miocene.

Stratigraphic data indicate an erosion phase in the Arabian Peninsula between the end of Paleogene and the beginning of the Neogene and a significant shifting of the eastern Arabia coastline to the northeast which could constrain such an event.

5. The Nile and Euphrates-Tigris river networks source from areas of positive residual and dynamic topography and have their base level in regions characterized by negative values. This suggest that the formation and evolution of these drainage systems are influenced by mantle processes. In particular, the stable presence of a mantle upwelling beneath east Africa and the progressive migration of mantle flow to Turkey contributed to the formation of the Nile (Oligocene) and Euphrates-Tigris (Middle Miocene) river networks and to the maintenance of their path through tens of millions of years.
6. The incision pattern (local relief) on the top and on both flanks of the swell is low except for the rift margins, where the higher values are related to the flexural uplift, and of the Ethiopian Plateau because of the strong fluvial erosion.
7. Analysis of flexural uplift at the Red Sea margins shows an increase in uplift from south to north confirming thermochronological data from literature. In general, the western margin presents lower values than the eastern one, while the deformation related to flexural is visible up to ~250 km from the Red Sea margins. The comparison between flexural data and filtered topography confirms that the Red Sea region topography is the result of the interaction between shallower (flexural uplift) and deeper (mantle plume) processes.
8. The distribution of ages of volcanic deposits shows a gradual decrease in maximum age from Ethiopia to Turkey which broadly follows the curves of filtered topography extracted along the axis of the swell.
9. Along the swell axis volcanoes and basaltic lava fields are located. The frequency of volcanic deposits ages shows a bimodal trend with peaks separated by a brief period of low volcanic activity with a trend toward younger ages from south to north. In particular, the older quiescence period is coeval with the advanced stage of the Arabia-Eurasia collision at the Bitlis zone and the activation of the Dead Sea Transform Fault. These processes caused the counterclockwise rotation of the Arabian plate and the change in the direction of maximum compression from NE-SW to N-S favoring the opening of N-S trending tectonic lineaments and the closure of old NW-SE ones. In confirmation of this, Arabian volcanics older than 16 Ma emplaced through NW-SE-trending dikes, while younger deposits appear aligned in a N-S direction.

All these results point to the presence of a single process which shaped the past and present topographic configuration of the region, the upwelling of the Afar superplume. Once the plume reached the base of the lithosphere below the Horn of Africa, it flowed laterally toward the Levant area by exploiting pre-existing lithospheric structure, and then reached the Anatolian Plateau, facilitated by slab break-off and the consequent formation of a slab window. The buoyancy of the mantle material below the lithosphere generated the East African-Arabia swell interrupted to the north by the Mesopotamian foredeep basin.

Declaration of competing interest

Claudio Faccenna reports financial support was provided by Italian Research Ministry. If there are other authors, they declare that they have no known competing financial interests or personal relationships that could have appeared to influence the work reported in this paper.

Data availability

The original data supporting this research are available in the supplementary material or on request.

Acknowledgments

We thank the editor and anonymous reviewers for their efforts and comments which served to improve this manuscript from its original version. We also thank Alistair Boyce for sharing his Moho constraint compilation, as well as all authors for publishing SKS splitting and seismic tomography models openly. Several figures were generated with the Generic Mapping Tools by the late, great Pal Wessel (Wessel et al., 2019). This work has been supported by the project "Intraplate deformation, magmatism and topographic evolution of a diffuse collisional belt: Insights into the geodynamics of the Arabia-Eurasia collisional zones" funded by the Italian Research Ministry (MUR-PRIN 2017–2021). We thank all project participants for many fruitful discussions. TWB was supported by NSF EAR-1925939.

Appendix A. Supplementary data

Supplementary data to this article can be found online at https://doi.org/10.1016/j.earscirev.2024.104901.

References

Abbate, E., Bruni, P., Ferretti, M.P., Delmer, C., Laurenzi, M.A., Hagos, M., et al., 2014. The East Africa Oligocene intertrappean beds: Regional distribution, depositional environments and Afro/Arabian mammal dispersals. J. Afr. Earth Sci. 99, 463–489.
Abebe, T., Balestrieri, M.L., Bigazzi, G., 2010. The Central Main Ethiopian rift is younger than 8 Ma: Confirmation through apatite fission-track thermochronology. Terra Nova 22 (6), 470–476.
Agostini, S., Di Giuseppe, P., Manetti, P., Doglioni, C., Conticelli, S., 2021. A heterogeneous subcontinental mantle under the African–Arabian Plate boundary revealed by boron and radiogenic isotopes. Sci. Rep. 11 (1), 11230.
Al Kwatli, M.A., Gillot, P.Y., Zeyen, H., Hildenbrand, A., Al Gharib, I., 2012. Volcano-tectonic evolution of the northern part of the Arabian plate in the light of new K–Ar ages and remote sensing: Harrat Ash Shaam volcanic province (Syria). Tectonophysics 580, 192–207.
Alemu, T., 2021. Tectonic evolution of the Pan-African Belt in Western Ethiopia, Southern Arabian-Nubian Shield. In: Hamimi, Z., et al. (Eds.), The Geology of the Arabian-Nubian Shield, Regional Geology Reviews, pp. 81–108.
Almond, D.C., 1986. Geological evolution of the Afro-Arabian dome. Tectonophysics 131, 301–332.
Alsharhan, A.S., Nairn, A.E.M., 1995. Tertiary of the Arabian Gulf: sedimentology and hydrocarbon potential. Palaeogeogr. Palaeoec. 114 (2–4), 369–384.
Andriampenomanana, F., Nyblade, A., Durrheim, R., Tugume, F., Nyago, J., 2021. Shear wave splitting measurements in northeastern Uganda and southeastern Tanzania: corroborating evidence for sublithospheric mantle flow beneath East Africa. Geophys. J. Int. 226 (3), 1696–1704.
ArRajehi, A., McClusky, S., Reilinger, R., Daoud, M., Alchalbi, A., Ergintav, S., et al., 2010. Geodetic constraints on present-day motion of the Arabian Plate: Implications for Red Sea and Gulf of Aden rifting. Tectonics 29 (3).
Auer, L., Boschi, L., Becker, T.W., Nissen-Meyer, T., Giardini, D., 2014. Savani: a variable resolution whole-mantle model of anisotropic shear velocity variations based on multiple data sets. *J. Geophys. Res.: Solid.* Earth 119 (4), 3006–3034.
Avigad, D., Gvirtzman, Z., 2009. Late Neoproterozoic rise and fall of the northern Arabian–Nubian Shield: the role of lithospheric mantle delamination and subsequent thermal subsidence. Tectonophysics 477 (3–4), 217–228.
Avni, Y., 1991. The geology, paleogeography and the landscape evolution of the Central Negev Highlands and the western Ramon structure. Isr. Geol. Surv. Rep. GSI/6/91, 153 pp.
Avni, Y., Segev, A., Ginat, H., 2012. Oligocene regional denudation of the northern Afar dome: Pre-and syn-breakup stages of the Afro-Arabian plate. Bulletin 124 (11–12), 1871–1897.
Bagley, B., Nyblade, A.A., 2013. Seismic anisotropy in eastern Africa, mantle flow, and the African superplume. Geophys. Res. Lett. 40 (8), 1500–1505.
Baker, J., Snee, L., Menzies, M., 1996. A brief Oligocene period of flood volcanism in Yemen. Earth Planet. Sci. Lett. 138, 39–55.
Ballato, P., Uba, C.E., Landgraf, A., Strecker, M.R., Sudo, M., Stockli, D.F., et al., 2011. Arabia-Eurasia continental collision: Insights from late Tertiary foreland-basin evolution in the Alborz Mountains, northern Iran. Bulletin 123 (1–2), 106–131.
Ballato, P., Parra, M., Schildgen, T.F., Dunkl, I., Yıldırım, C., Özsayın, E., Sobel, E.R., Echtler, H., Strecker, M.R., 2018. Multiple exhumation phases in the Central Pontides (N Turkey): New temporal constraints on major geodynamic changes associated with the closure of the Neo-Tethys Ocean. Tectonics 37 (6), 1831–1857.
Bar, O., Zilberman, E., 2016. Subsidence and conversion of the Dead Sea basin to an inland erosion base level in the early middle Miocene as inferred from geomorphological analysis of its ancient western fluvial outlet. Geomorphology 261, 147–161.
Bar, O., Gvirtzman, Z., Feinstein, S., Zilberman, E., 2013. Accelerated subsidence and sedimentation in the Levant Basin during the late Tertiary and concurrent uplift of

the Arabian platform: Tectonic versus counteracting sedimentary loading effects. Tectonics 32 (3), 334–350.
Bar, O., Zilberman, E., Feinstein, S., Calvo, R., Gvirtzman, Z., 2016. The uplift history of the Arabian Plateau as inferred from geomorphologic analysis of its northwestern edge. Tectonophysics 671, 9–23.
Barnett-Moore, N., Hassan, R., Flament, N., Müller, D., 2017. The deep Earth origin of the Iceland plume and its effects on regional surface uplift and subsidence. Sol. Ea. 8 (1), 235–254.
Barrier, E., Vrielynck, B., 2008. Palaeotectonic Maps of the Middle East. Atlas of, p. 14.
Bastow, I.D., Nyblade, A.A., Stuart, G.W., Rooney, T.O., Benoit, M.H., 2008. Upper mantle seismic structure beneath the Ethiopian hot spot: Rifting at the edge of the African low-velocity anomaly. Geochem. Geophys. Geosyst. 9, Q12022 https://doi.org/10.1029/2008GC002107.
Bastow, I.D., Pilidou, S., Kendall, J.M., Stuart, G.W., 2010. Melt-induced seismic anisotropy and magma assisted rifting in Ethiopia: evidence from surface waves. Geochem. Geophy. Geosyst. 11 (6).
Bartol, J., Govers, R., 2014. A single cause for uplift of the Central and Eastern Anatolian plateau? Tectonophysics 637, 116–136.
Bastow, I.D., Keir, D., Daly, E., 2011. The Ethiopia Afar Geoscientific Lithospheric Experiment (EAGLE): probing the transition from continental rifting to incipient sea floor spreading. Geol. Soc. Am., Soc. Pap. 478, ISSN, 1366–8781.
Becker, T.W., Lebedev, S., Long, M.D., 2012. On the relationship between azimuthal anisotropy from shear wave splitting and surface wave tomography. J. Geophys. Res. - Solid Earth 117, B01306. https://doi.org/10.1029/2011JB008705. Compilation updated in 05/2024, and available online at. http://www-udc.ig.utexas.edu/external/becker/sksdata.html. accessed 05/2024.
Becker, T.W., Faccenna, C., Humphreys, E.D., Lowry, A.R., Miller, M.S., 2014. Static and dynamic support of western U.S. topography. Earth Planet. Sci. Lett. 402, 234–246.
Bellahsen, N., Faccenna, C., Funiciello, F., Daniel, J.M., Jolivet, L., 2003. Why did Arabia separate from Africa? Insights from 3-D laboratory experiments. Earth Planet. Sci. Lett. 216 (3), 365–381. https://doi.org/10.1016/S0012-821X(03)00516-8.
Beltrandi, M.D., Pyre, A., 1973. Geological evolution of Southwest Somalia. Sedimentary Basins of the African Coasts 2, 159–178.
Ben-Israel, M., Matmon, A., Hidy, A.J., Avni, Y., Balco, G., 2020. Early-to-mid Miocene erosion rates inferred from pre-Dead Sea rift Hazeva River fluvial chert pebbles using cosmogenic 21 Ne. Earth. Surf. Dynam. 8 (2), 289–301.
Benoit, M.H., Nyblade, A.A., VanDecar, J.C., Gurrola, H., 2006a. Upper mantle P wave velocity structure and transition zone thickness beneath the Arabian Shield. Geophys. Res. Lett. 30 (10), 3–6. https://doi.org/10.1029/2002gl016436.
Benoit, M.H., Nyblade, A.A., Owens, T.J., Stuart, G., 2006b. Mantle transition zone structure and upper mantle S velocity variations beneath Ethiopia: evidence for a broad, deep-seated thermal anomaly. Geochem., Geophy., Geosy. 7 (11).
Berberian, M., 1995. Master "blind" thrust faults hidden under the Zagros folds: active basement tectonics and surface morphotectonics. Tectonophysics 241 (3–4), 193–224.
Berk Biryol, C., Beck, S.L., Zandt, G., Özacar, A.A., 2011. Segmented African lithosphere beneath the Anatolian region inferred from teleseismic P-wave tomography. Geophys. J. Int. 184 (3), 1037–1057.
Beydoun, Z.R., 1991. Arabian Plate Hydrocarbon Geology and Potential—A Plate Tectonic Approach. American Association of Petroleum Geologists.
Beydoun, Z.R., 1999. Evolution and development of the Levant (Dead Sea Rift) Transform System: a historical-chronological review of a structural controversy. Geol. Soc. Spec. Publ. 164 (1), 239–255.
Bonini, M., Corti, G., Innocenti, F., Manetti, P., Mazzarini, F., Abebe, T., Pecskay, Z., 2005. Evolution of the Main Ethiopian Rift in the frame of Afar and Kenya rifts propagation. Tectonics 24 (1).
Bookhagen, B., Thiede, R.C., Strecker, M.R., 2005. Abnormal monsoon years and their control on erosion and sediment flux in the high, arid northwest Himalaya. Earth Planet. Sci. Lett. 231 (1–2), 131–146.
Boone, S.C., Balestrieri, M.L., Kohn, B., 2021. Thermo-tectonic imaging of the Gulf of Aden-Red Sea rift systems and Afro-Arabian hinterland. Earth Sci. Rev. 222, 103824.
Bosworth, W., Stockli, D.F., 2016. Early magmatism in the greater Red Sea rift: timing and significance. Can. J. Earth Sci. 53 (11), 1158–1176.
Bosworth, W., Huchon, P., McClay, K., 2005. The red sea and gulf of Aden basins. J. Afr. Earth Sci. 43 (1–3), 334–378.
Bottrill, A.D., van Hunen, J., Allen, M.B., 2012. Insight into collision zone dynamics from topography: numerical modelling results and observations. Solid Earth 3 (2), 387–399.
Boyce, A., Bastow, I.D., Cottaar, S., Kounoudis, R., Guilloud De Courbeville, J., Caunt, E., Desai, S., 2021. AFRP20: New P-wavespeed model for the African mantle reveals two whole-mantle plumes below East Africa and neoproterozoic modification of the Tanzania Craton. Geochem., Geophy., Geosy. 22 (3) e2020GC009302.
Boyce, A., Kounoudis, R., Bastow, I.D., Cottaar, S., Ebinger, C.J., Ogden, C.S., 2023. Mantle wavespeed and discontinuity structure below East Africa: Implications for Cenozoic hotspot tectonism and the development of the Turkana Depression. Geochem. Geophys. Geosyst. 24 (8) e2022GC010775.
Braun, J., 2010. The many surface expressions of mantle dynamics. Nat. Geosci. 3 (12), 825.
Brew, G., Barazangi, M., Al-Maleh, A.K., Sawaf, T., 2001. Tectonic and geologic evolution of Syria. GeoArabia 6 (4), 573–616.
Brown, F.H., Mcdougall, I., 2011. Geochronology of the Turkana depression of northern Kenya and southern Ethiopia. Evol. Anthrop.: Issues, News, and Rev. 20 (6), 217–227.
Brown, G.F., Schmidt, D.L., Huffan, A.C., 1989. Geology of the Arabian Peninsula, Shield area of western Saudi Arabia. In: U.S. Geological Survey Professional Paper, 560-A.
Burke, K., 1996. The African plate. S. Afr. J. Geol. 99 (4), 341–409.
Burke, K., Gunnell, Y., 2008. The African erosion Surface: A Continental-Scale Synthesis of Geomorphology, Tectonics, and Environmental Change over the Past 180 Million Years. Soc. Am, Geol. https://doi.org/10.1130/MEM201.
Burke, K., Torsvik, T.H., 2004. Derivation of large igneous provinces of the past 200 million years from long-term heterogeneities in the deep mantle. Earth Planet. Sc. Lett. 227 (3–4), 531–538.
Burov, E., Gerya, T., 2014. Asymmetric three-dimensional topography over mantle plumes. Nature 513, 85–89.
Burov, E., Guillou-Frottier, L., 2005. The plume-head continental lithosphere interaction using a tectonically realistic formulation for the lithosphere. Geophys. J. Int. 58 https://doi.org/10.1111/j.136.-246x.2005.02588.x.
Burrough, P.A., McDonnell, R., 1998. Principles of Geographical Information Systems. Oxford University Press, Oxford, p. 333.
Camp, V.E., Roobol, M.J., 1992. Upwelling asthenosphere beneath western Arabia and its regional implications. *J. Geophys. Res.: Solid*. Earth 97 (B11), 15255–15271.
Cao, X., Flament, N., Müller, D., Li, S., 2018. The dynamic topography of eastern China since the latest Jurassic Period. Tectonics 37 (5), 1274–1291.
Cavazza, W., Cattò, S., Zattin, M., Okay, A.I., Reiners, P., 2018. Thermochronology of the Miocene Arabia-Eurasia collision zone of southeastern Turkey. Geosphere 14 (5), 2277–2293.
Cavazza, W., Albino, I., Galoyan, G., Zattin, M., Catto, S., 2019. Continental accretion and incremental deformation in the thermochronologic evolution of the Lesser Caucasus. Geosci. Front. 10 (6), 2189–2202. https://doi.org/10.1016/j.gsf.2019.02.007.
Chaimov, T.A., Barazangi, M., Al-Saad, D., Sawaf, T., Gebran, A., 1990. Crustal shortening in the Palmyride fold belt, Syria, and implications for movement along the Dead Sea fault system. Tectonics 9 (6), 1369–1386.
Champagnac, J.D., Schlunegger, F., Norton, K., von Blanckenburg, F., Abbühl, L.M., Schwab, M., 2009. Erosion-driven uplift of the modern Central Alps. Tectonophysics 474 (1–2), 236–249.
Chang, S.J., Van der Lee, S., 2011. Mantle plumes and associated flow beneath Arabia and East Africa. Earth Plan. Sci. Lett. 302 (3–4), 448–454.
Chang, S.-J., Merino, M., Van Der Lee, S., Stein, S., Stein, C.A., 2011. Mantle flow beneath Arabia offset from the opening Red Sea. Geophys. Res. Lett. 38 (4), 1–5. https://doi.org/10.1029/2010GL045852.
Chang, S.-J., Kendall, E., Davaille, A., Ferreira, A.M.G., 2020. The evolution of mantle plumes in East Africa. J. Geophys. Res. Solid Earth 125 (12). https://doi.org/10.1029/2020JB019929 e2020JB019929.
Chen, B., Kaban, M.K., El Khrepy, S., Al-Arifi, N., 2015. Effective elastic thickness of the Arabian plate: Weak shield versus strong platform. Geophys. Res. Lett. 42, 3298–3304. https://doi.org/10.1002/2015GL063725.
Civiero, C., Lebedev, S., Celli, N.L., 2022. A complex mantle plume head below East Africa-Arabia shaped by the lithosphere-asthenosphere boundary topography. Geochem., Geophy., Geosy. 23 https://doi.org/10.1029/2022GC010610 e2022GC010610.
Clementucci, R., Ballato, P., Siame, L., Fox, M., Lanari, R., Sembroni, A., , et al.Essaifi, A., 2023. Surface uplift and topographic rejuvenation of a tectonically inactive range: Insights from the Anti-Atlas and the Siroua Massif (Morocco). Tectonics 42 (2) e2022TC007383.
Cloetingh, S., Koptev, A., Lavecchia, A., Kovács, I.J., Beekman, F., 2022. Fingerprinting secondary mantle plumes. Earth Plan. Sci. Lett. 597, 117819 https://doi.org/10.1016/j.epsl.2022.117819.
Cloos, H., 1939. Hebung-Spaltung-Volcanismus. Geol. Rundsch. 30, 405–427.
Coleman, R.G., Gregory, R.T., Brown, G.F., 1983. Cenozoic Volcanic Rocks of Saudi Arabia, vol. 83. US Department of the Interior, Geological Survey. No. 788.
Coltorti, M., Dramis, F., Ollier, C.D., 2007. Planation surfaces in northern Ethiopia. Geomorphology 89 (3–4), 287–296.
Coltorti, M., Firuzabadi, D., Borri, A., Fantozzi, P., Pieruccini, P., 2015. Planation surfaces and the long-term geomorphological evolution of Ethiopia. Landscapes and landforms of Ethiopia 117–136.
Corti, G., 2009. Continental rift evolution: from rift initiation to incipient break-up in the Main Ethiopian Rift. East Africa. Earth-Sc. Rev. 96 (1–2), 1–53.
Courtillot, V., Jaupart, C., Manighetti, I., Tapponnier, P., Besse, J., 1999. On causal links between flood basalts and continental breakup. Earth Plan. Sci. Lett. 166 (3–4), 177–195.
Courtillot, V., Davaille, A., Besse, J., Stock, J., 2003. Three distinct types of hotspots in the Earth's mantle. Earth Plan. Sci. Lett. 205 (3–4), 295–308.
Cox, K.G., 1989. The role of mantle plumes in the development of continental drainage patterns. Nature 342 (6252), 873–877.
Crameri, F., Schmeling, H., Golabek, G.J., Duretz, T., Orendt, R., Buiter, S.J.H., Tackley, P.J., et al., 2012. A comparison of numerical surface topography calculations in geodynamic modelling: an evaluation of the 'sticky air' method. Geophys. J. Int. 189 (1), 38–54.
Czarnota, K., Roberts, G.G., White, N.J., Fishwick, S., 2014. Spatial and temporal patterns of Australian dynamic topography from River Profile Modeling. J. Geophys. Res.-Sol. Ea. 119 (2), 1384–1424.
d'Acremont, E., Leroy, S., Burov, E.B., 2003. Numerical modelling of a mantle plume: the plume head–lithosphere interaction in the formation of an oceanic large igneous province. Earth Planet. Sc. Lett. 206 (3–4), 379–396.
D'Agostino, N., McKenzie, D.P., 1999. Convective support of long wavelength topography in the Apennines (Italy). Terra Nova 11, 234–238.
Daradich, A., Mitrovica, J.X., Pysklywec, R.N., Willett, S.D., Forte, A.M., 2003. Mantle flow, dynamic topography, and rift-flank uplift of Arabia. Geology 31, 901–904.
Darin, M.H., Umhoefer, P.J., 2022. Diachronous initiation of Arabia–Eurasia collision from eastern Anatolia to the southeastern Zagros Mountains since middle Eocene

time. Int. Geol. Rev. 64 (18), 2653–2681. https://doi.org/10.1080/00206814.2022.2048272.
Davidson, A., 1983. Reconnaissance Geology and Geochemistry of Parts of Illubabor, Kefa, Gemu Gofa and Sidamo. Ethiopia, Ministry of Mines and Energy, Ethiopian Institute of Geological Surveys, Bulletin, p. 2.
Davidson, A., McGregor, D.C., 1976. Palynomorphs indicating Permian rocks in Ethiopia. Nature 262 (5567), 371–373.
Davila, F.M., Lithgow-Bertelloni, C., 2013. Dynamic topography in South America. J. South Am. Earth Sci. 43, 127–144.
Davison, I., Steel, I., 2018. Geology and hydrocarbon potential of the East African continental margin: a review. Pet. Geosci. 24 (1), 57–91.
de Vries, D., Heritage, S., Borths, M.R., Sallam, H.M., Seiffert, E.R., 2021. Widespread loss of mammalian lineage and dietary diversity in the early Oligocene of Afro-Arabia. Comm. Bio. 4 (1), 1172.
Debayle, E., Lévêque, J.J., Cara, M., 2001. Seismic evidence for a deeply rooted low-velocity anomaly in the upper mantle beneath the northeastern Afro/Arabian continent. Earth Plan. Sci. Lett. 193 (3–4), 423–436.
Demir, T., Westaway, R., Bridgland, D., Pringle, M., Yurtmen, S., Beck, A., Rowbotham, G., 2007. Ar-Ar dating of late Cenozoic basaltic volcanism in northern Syria: Implications for the history of incision by the River Euphrates and uplift of the northern Arabian Platform. Tectonics 26 (3).
Demir, T., Seyrek, A., Westaway, R., Bridgland, D., Beck, A., 2008. Late Cenozoic surface uplift revealed by incision by the River Euphrates at Birecik, Southeast Turkey. Quatern. Int. 186 (1), 132–163.
Dercourt, J.E.A., Zonenshain, L.P., Ricou, L.E., Kazmin, V.G., Le Pichon, X., Knipper, A. L., Biju-Duval, B., et al., 1986. Geological evolution of the Tethys belt from the Atlantic to the Pamirs since the Lias. Tectonophysics 123 (1–4), 241–315.
Dietz, R.S., Menard, H.W., 1953. Hawaiian swell, deep, and arch, and subsidence of the Hawaiian Islands. J. Geol. 61 (2), 99–113.
Dixon, T.H., Ivins, E.R., Franklin, B.J., 1989. Topographic and volcanic asymmetry around the Red Sea: Constraints on rift models. Tectonics 8 (6), 1193–1216.
Ebinger, C., 2005. Continental break-up: the East African perspective. Astron. Geophys. 46 (2), 2–16.
Ebinger, C., Sleep, N.H., 1998. Cenozoic magmatism in central and East Africa resulting from impact of one large plume. Nature 395, 788–791.
Ebinger, C.J., Forsyth, D.W., Bow, C.O., Bowin, C.O., 1989. Effective elastic plate thickness beneath the East African and Afar plateaus and dynamic compensation of the uplifts. J. Geophys. Res. 94 (B3), 2883–2901. https://doi.org/10.1029/jb094ib03p02883.
Ebinger, C.J., Reiss, M.C., Bastow, I., Karanja, M.M., 2024. Shallow sources of upper mantle seismic anisotropy in East Africa. Earth Planet. Sci. Lett. 625, 118488.
Emry, E.L., Shen, Y., Nyblade, A.A., Flinders, A., Bao, X., 2019. Upper mantle Earth structure in Africa from full-wave ambient noise tomography. Geochem. Geophys. Geosyst. 20 (1), 120–147.
Ernst, R.E., Youbi, N., 2017. How large Igneous Provinces affect global climate, sometimes cause mass extinctions, and represent natural markers in the geological record. Palaeogeogr. Palaeoec. 478, 30–52.
Ershov, A., Nikishin, A., 2004. Recent geodynamics of the Caucasus-Arabia-east Africa region. Geotectonics 38 (2), 123–136.
Faccenna, C., Becker, T.W., 2020. Topographic expressions of mantle dynamics in the Mediterranean. Earth-Sc. Rev. 209, 103327.
Faccenna, C., Bellier, O., Martinod, J., Piromallo, C., Regard, V., 2006. Slab detachment beneath eastern Anatolia: a possible cause for the formation of the North Anatolian fault. Earth Plan. Sci. Lett. 242 (1–2), 85–97.
Faccenna, C., Molin, P., Orecchio, B., Olivetti, V., Bellier, O., Funiciello, F., , et al.Billi, A., 2011. Topography of the Calabria subduction zone (southern Italy): Clues for the origin of Mt. Etna. *Tectonics* 30 (1).
Faccenna, C., Becker, T.W., Jolivet, L., Keskin, M., 2013. Mantle convection in the Middle East: Reconciling Afar upwelling, Arabia indentation and Aegean trench rollback. Earth Plan. Sci. Lett. 375, 254–269.
Faccenna, C., Glisovic, P., Forte, A., Becker, T.W., Garzanti, E., Sembroni, A., Gvirtzman, Z., 2019. Role of dynamic topography in sustaining the Nile River over 30 million years. Nat. Geosci. 12 (12).
Farnetani, C.G., Richards, M.A., 1994. Numerical investigations of the mantle plume initiation model for flood basalt events. J. Geophys. Res.-Sol. Ea. 99 (B7), 13813–13833.
Fielding, E.J., 1996. Tibet uplift and erosion. Tectonophysics 260 (1–3), 55–84.
Fishwick, S., 2010. Surface wave tomography: Imaging of the lithosphere-asthenosphere boundary beneath central and southern Africa? Lithos 120 (1–2), 63–73. https://doi.org/10.1016/j.lithos.2010.05.011.
Fishwick, S., Bastow, I.D., 2011. Towards a better understanding of African topography: a review of passive-source seismic studies of the African crust and upper mantle. Geol. Soc. Spec. Publ. 357 (1), 343–371.
Flament, N., Gurnis, M., Müller, R.D., 2013. A review of observations and models of dynamic topography. Lithos 5 (2), 189–210.
Forte, A.M., Quere, S., Moucha, R., Simmons, N.A., Grand, S.P., Mitrovica, J.X., Rowley, D.B., 2010. Joint seismic–geodynamic-mineral physical modelling of African geodynamics: a reconciliation of deep-mantle convection with surface geophysical constraints. Earth Plan. Sci. Lett. 295 (3–4), 329–341. https://doi.org/10.1016/j.epsl.2010.03.017.
French, S.W., Romanowicz, B., 2015. Broad plumes rooted at the base of the Earth's mantle beneath major hotspots. Nature 525, 95–99.
Freund, R., Garfunkel, Z., Zak, I., Goldberg, M., Weissbrod, T., Derin, B., Girdler, R.W., et al., 1970. The Shear along the Dead Sea Rift. Philosophical Transactions for the Royal Society of London. Series A, Mathematical and Physical Sciences, pp. 107–130.
Friedrich, A.M., 2019. Palaeogeological hiatus surface mapping: a tool to visualize vertical motion of the continents. Geol. Mag. 156 (2), 308–319.
Gaina, C., Van Hinsbergen, D.J., Spakman, W., 2015. Tectonic interactions between India and Arabia since the Jurassic reconstructed from marine geophysics, ophiolite geology, and seismic tomography. Tectonics 34 (5), 875–906.
Gani, N.D., 2015. Erosion history from incision modeling and river profile morphologies: example from the Tekeze River System, Ethiopian Plateau, East Africa. Arab. J. Geosci. 8, 11293–11305.
Gani, N.D., Neupane, P.C., 2018. Understanding transient landscape of the Ethiopian Plateau in relation to mantle dynamics. Geol. J. 53 (1), 371–385.
Gani, N.D., Gani, M.R., Abdelsalam, M.G., 2007. Blue Nile incision on the Ethiopian Plateau: Pulsed plateau growth, Pliocene uplift, and hominin evolution. GSA Today 17 (9), 4–11.
Gani, N.D., van Soest, M.C., Gani, M.R., Blackburn, N.C., Neupane, P., Bowden, S., Tadesse, K., 2023. Investigating apatite (U-Th)/he thermochronologic ages to understand exhumation history of the Ethiopian Plateau. J. Afr. Earth Sci. 198, 104605.
Garfunkel, Z., 1981. Internal structure of the Dead Sea leaky transform (rift) in relation to plate kinematics. Tectonophysics 80 (1–4), 81–108.
Garfunkel, Z., 1998. Constrains on the origin and history of the Eastern Mediterranean basin. Tectonophysics 298 (1–3), 5–35.
Garfunkel, Z., 1999. History and paleogeography during the Pan-African orogen to stable platform transition: Reappraisal of the evidence from the Elat area and the northern Arabian-Nubian Shield. Isr. J. Earth Sci. 48, 135–157.
Garfunkel, Z., 2002. Early Paleozoic Sediments of NE Africa and Arabia: Products of Continental-Scale erosion, Sediment Transport, and Deposition. Isr, J. Earth Sci, p. 51.
Garfunkel, Z., 2004. Origin of the Eastern Mediterranean basin: a reevaluation. Tectonophysics 391 (1–4), 11–34.
Garfunkel, Z., Horowitz, A., 1966. The Upper Tertiary and Quaternary morphology of the Negev. Isr. J. Earth Sci. 15, 101–117.
Garfunkel, Z., Zak, I., Freund, R., 1981. Active faulting in the Dead Sea rift. Tectonophysics 80 (1–4), 1–26.
Garzanti, E., Andò, S., Vezzoli, G., Megid, A.A.A., El Kammar, A., 2006. Petrology of Nile River sands (Ethiopia and Sudan): sediment budgets and erosion patterns. Earth Plan. Sci. Lett. 252 (3–4), 327–341.
Gibbons, A.D., Whittaker, J.M., Müller, R.D., 2013. The breakup of East Gondwana: Assimilating constraints from cretaceous ocean basins around India into a best-fit tectonic model. J. Geophys. Res.-Sol. Ea. 118 (3), 808–822.
Godard, V., Lavé, J., Carcaillet, J., Cattin, R., Bourlès, D., Zhu, J., 2010. Spatial distribution of denudation in Eastern Tibet and regressive erosion of plateau margins. Tectonophysics 491 (1–4), 253–274.
Göğüş, O.H., Pysklywec, R.N., 2008. Mantle lithosphere delamination driving plateau uplift and synconvergent extension in eastern Anatolia. Geology 36 (9), 723–726.
Griffiths, R.W., Campbell, I.H., 1991. Interaction of mantle plume heads with the Earth's surface and onset of small-scale convection. J. Geophys. Res.-Sol. Ea. 96 (B11), 18295–18310.
Guiraud, R., Bosworth, W., Thierry, J., Delplanque, A., 2005. Phanerozoic geological evolution of Northern and Central Africa: an overview. J. Afr. Earth Sci. 43 (1–3), 83–143.
Gurnis, M., Mitrovica, J.X., Ritsema, J., van Heijst, H.J., 2000. Constraining mantle density structure using geological evidence of surface uplift rates: the case of the African Superplume. Geochem. Geophys. Geosyst. 1, 1020. https://doi.org/10.1029/1999GC000035.
Gusmeo, T., Cavazza, W., Alania, V.M., Enukidze, O.V., Zattin, M., Corrado, S., 2021. Structural inversion of back-arc basins – the Neogene Adjara-Trialeti fold-and-thrust belt (SW Georgia) as a far-field effect of the Arabia-Eurasia collision. Tectonophysics 803, 228702. https://doi.org/10.1016/j.tecto.2020.228702.
Gvirtzman, Z., Zilberman, E., Folkman, Y., 2008. Reactivation of the Levant passive margin during the late Tertiary and formation of the Jaffa Basin offshore Central Israel. J. Geol. Soc. London 165 (2), 563–578.
Gvirtzman, Z., Steinberg, J., Bar, O., Buchbinder, B., Zilberman, E., Siman-Tov, R., Rosensaft, M., et al., 2011. Retreating late Tertiary shorelines in Israel: Implications for the exposure of North Arabia and Levant during Neotethys closure. Lithosphere 3 (2), 95–109.
Gvirtzman, Z., Faccenna, C., Becker, T.W., 2016. Isostasy, flexure, and dynamic topography. Tectonophysics 683, 255–271.
Hager, B.H., Clayton, R.W., Richards, M.A., Comer, R.P., Dzievonski, A.M., 1985. Lower mantle heterogeneity, dynamic topography and the geoid. Nature 313 (6003), 541.
Hammond, J.O.S., Kendall, J.-M., Wookey, J., Stuart, G.W., Keir, D., Ayele, A., 2014. Differentiating flow, melt, or fossil seismic anisotropy beneath Ethiopia. Geochem. Geophys. Geosyst. 15, 1878–1894. https://doi.org/10.1002/2013GC005185.
Hansen, S.E., Nyblade, A.A., 2013. The deep seismic structure of the Ethiopia/Afar hotspot and the African superplume. Geophys. J. Int. 194 (1), 118–124.
Hansen, S.E., Nyblade, A.A., Benoit, M.H., 2012. Mantle structure beneath Africa and Arabia from adaptively parameterized P-wave tomography: Implications for the origin of Cenozoic Afro-Arabian tectonism. Earth Plan. Sci. Lett. 319, 23–34. https://doi.org/10.1016/j.epsl.2011.12.023.
Hansen, S., Schwartz, S., Al-Amri, A., Rodgers, A., 2006. Combined plate motion and density-driven flow in the asthenosphere beneath Saudi Arabia: evidence from shear-wave splitting and seismic anisotropy. Geology 34 (10), 869–872. https://doi.org/10.1130/g22713.1.
Hartmann, J., Moosdorf, N., 2012. The new global lithological map database GLiM: a representation of rock properties at the Earth surface. Geochem. Geophys. Geosyst. 13 (12).

Heller, P.L., Liu, L., 2016. Dynamic topography and vertical motion of the US Rocky Mountain region prior to and during the Laramide orogeny. Bulletin 128 (5–6), 973–988.
Heron, P.J., 2018. Mantle Plumes and Mantle Dynamics in the Wilson Cycle. *In*: Wilson, R.W., Houseman, G.A., Mccaffrey, K.J.W., Dor'e, a.G., Buiter, S.J.H. (Eds.), Fifty Years of the Wilson Cycle Concept in Plate Tectonics. Geol. Soc. Spec. Publ, p. 470. https://doi.org/10.1144/SP470.18.
Hessami, K., Koyi, H.A., Talbot, C.J., Tabasi, H., Shabanian, E., 2001. Progressive unconformities within an evolving foreland fold–thrust belt. Zagros Mountains. J. Geol. Soc. 158 (6), 969–981.
Hofmann, C., Courtillot, V., Feraud, G., Rochette, P., Yirgu, G., Ketefo, E., Pik, R., 1997. Timing of the Ethiopian flood basalt event and implications for plume birth and global change. Nature 389, 838–841.
Hoke, G., Isacks, L., Jordan, T.E., 2005. Equilibrium landscapes of the western Andean mountain front (10°S - 33°S): Long-term responses to along-strike changes in climate. In: 6th International Symposium on Andean Geodynamics (ISAG 2005, Barcelona), Extended Abstracts, pp. 386–389.
Hosseini, K., Sigloch, K., Tsekhmistrenko, M., Zaheri, A., Nissen-Meyer, T., Igel, H., 2020. Global mantle structure from multifrequency tomography using P, PP and P-diffracted waves. Geophys. J. Int. 220 (1), 96–141.
Houseman, G.A., 1990. The thermal structure of mantle plumes: axisymmetric or triple-junction? Geophys. J. Int. 102 (1), 15–24.
Hua, J., Fischer, K.M., Gazel, E., Parmentier, E.M., Hirth, G., 2023. Long-distance asthenospheric transport of plume-influenced mantle from Afar to Anatolia. Geochem. Geophys. Geosyst. 24 https://doi.org/10.1029/2022GC010605 e2022GC010605.
Hunegnaw, A., Sage, L., Gonnard, R., 1998. Hydrocarbon potential of the intracratonic Ogaden Basin. SE Ethiopia. *J. Petrol. Geol.* 21 (4), 401–425.
Ilani, S., Harlavan, Y., Tarawneh, K., Rabba, I., Weinberger, R., Ibrahim, K., , et al. Steinitz, G., 2001. New K-Ar ages of basalts from the Harrat Ash Shaam volcanic field in Jordan: Implications for the span and duration of the upper-mantle upwelling beneath the western Arabian plate. Geology 29 (2), 171–174.
Isacks, B.L., 1992. Long Term Land Surface Processes: Erosion, Tectonics and climate history in Mountain Belts. In: Mather, P. (Ed.), TERRA-1, Understanding the Terrestrial Environment. Taylor and Francis, London, UK, pp. 21–36.
Ismail, E.H., Abdelsalam, M.G., 2012. Morpho-tectonic analysis of the Tekeze River and the Blue Nile drainage systems on the Northwestern Plateau. Ethiopia. *J. Afr. Earth Sci.* 69, 34–47.
Joffe, S., Garfunkel, Z., 1987. Plate kinematics of the circum Red Sea—a re-evaluation. Tectonophysics 141 (1–3), 5–22.
Johnson, P.R., 2003. Post-amalgamation basins of the NE Arabian shield and implications for neoproterozoic III tectonism in the northern East African orogen. Precambrian Res. 123, 321–337.
Johnson, P.R., Zoheir, B.A., Ghebreab, W., Stern, R.J., Barrie, C.T., Hamer, R.D., 2017. Gold-bearing volcanogenic massive sulfides and orogenic-gold deposits in the Nubian Shield. S. Afr. J. Geol. 120 (1), 63–76.
Jones, S.M., Lovell, B., Crosby, A.G., 2012. Comparison of modern and geological observations of dynamic support from mantle convection. J. Geol. Soc. London 169 (6), 745–758.
Kendall, J.M., Stuart, G.W., Ebinger, C.J., Bastow, I.D., Keir, D., 2005. Magma-assisted rifting in Ethiopia. Nature 433 (7022), 146–148.
Keskin, M., 2003. Magma generation by slab steepening and breakoff beneath a subduction-accretion complex: an alternative model for collision-related volcanism in Eastern Anatolia. Turkey. Geophys. Res. Lett. 30 (24).
Keskin, M., 2007. In: Foulger, G.R., Jurdy, D.M. (Eds.), Plates, Plumes, and Planetary Processes, Vol. 430,. Geological Society of America, pp. 693–722.
Khalil, H.M., Capitanio, F.A., Betts, P.G., Cruden, A.R., 2020. 3-D analog modeling constraints on rifting in the Afar region. Tectonics 39 (10) e2020TC006339.
Kieffer, B., Arndt, N., Lapierre, H., Bastien, F., Bosch, D., Pecher, A., , et al.Meugniot, C., 2004. Flood and shield basalts from Ethiopia: magmas from the African superswell. J. Petrol. 45 (4), 793–834. https://doi.org/10.1093/petrology/egg112.
Kiraly, A., Faccenna, C., Funiciello, F., Sembroni, A., 2015. Coupling surface and mantle dynamics: a novel experimental approach. Geophys. Res. Lett. 42 (10), 3863–3869.
Kohn, B.P., Eyal, M., Feinstein, S., 1992. A major late Devonian-early Carboniferous (Hercynian) Thermotectonic event at the NW margin of the Arabian-Nubian Shield: evidence from zircon fission track dating. Tectonics 11 (5), 1018–1027.
Koppers, A., Becker, T.W., Jackson, M., Konrad, K., Müller, R.D., Romanowicz, B., Steinberger, B., Whittaker, J., 2021. Mantle plumes and their role in Earth processes. Nature Rev. Earth & Environ. 2, 382–401.
Koptev, A., Calais, E., Burov, E., Leroy, S., Gerya, T., 2015. Dual continental rift systems generated by plume–lithosphere interaction. Nat. Geosci. 8 (5), 388–392.
Koptev, A., Cloetingh, S., Burov, E., François, T., Gerya, T., 2017. Long-distance impact of Iceland plume on Norway's rifted margin. Sci. Rep. 7 (1), 10408.
Koptev, A., Burov, E., Gerya, T., Le Pourhiet, L., Leroy, S., Calais, E., Jolivet, L., 2018. Plume-induced continental rifting and break-up in ultra-slow extension context: Insights from 3D numerical modeling. Tectonophysics 746, 121–137.
Koshnaw, R.I., Stockli, D.F., Schlunegger, F., 2019. Timing of the Arabia-Eurasia continental collision—evidence from detrital zircon U-Pb geochronology of the Red Bed Series strata of the northwest Zagros hinterland. Kurdistan region of Iraq. Geology 47 (1), 47–50.
Koulakov, I., Burov, E., Cloetingh, S., El Khrepy, S., Al-Arifi, N., Bushenkova, N., 2016. Evidence for anomalous mantle upwelling beneath the Arabian Platform from travel time tomography inversion. Tectonophysics 667, 176–188. https://doi.org/10.1016/j.tecto.2015.11.022.
Kounoudis, R., Bastow, I.D., Ebinger, C.J., Darbyshire, F., Ogden, C.S., Musila, M., Ugo, F., Ayele, A., Sullivan, G., Bendick, R., Mariita, N., Kianji, G., 2023. The development of rifting and magmatism in the multiply rifted Turkana Depression, East Africa: Evidence from surface-wave analysis of crustal and uppermost mantle structure. Earth and Planetary Science Letters 621, 118386.
Kounoudis, R., Bastow, I.D., Ogden, C.S., Goes, S., Jenkins, J., Grant, B., Braham, C., 2020. Seismic tomographic imaging of the Eastern Mediterranean mantle: implications for terminal-stage subduction, the uplift of Anatolia, and the development of the North Anatolian Fault. Geochemistry, Geophysics, Geosystems 21 (7), e2020GC009009.
Krenkel, E., 1924. Der Syrische Bogen. *Zentralblatt Mineralogie* 9 (10), 274–281.
Krienitz, M.S., Haase, K.M., Mezger, K., van den Bogaard, P., Thiemann, V., Shaikh-Mashail, M.A., 2009. Tectonic events, continental intraplate volcanism, and mantle plume activity in northern Arabia: Constraints from geochemistry and Ar-Ar dating of Syrian lavas. Geochem. Geophys., Geosy. 10 (4).
Kühni, A., Pfiffner, O.A., 2001. The relief of the Swiss Alps and adjacent areas and its relation to lithology and structure: topographic analysis from a 250-m DEM. Geomorphology 41 (4), 285–307.
Lanari, R., Boutoux, A., Faccenna, C., Herman, F., Willett, S.D., Ballato, P., 2023. Cenozoic exhumation in the Mediterranean and the Middle East. Earth-Sc. Rev. 237, 104328.
Laske, G., Masters, G., Ma, Z., Pasyanos, M., 2013. Update on CRUST1. 0—A 1-degree global model of Earth's. In: Geophysical Research Abstracts, vol. 15. EGU General Assembly, Vienna, Austria, p. 2658. No. 15.
Lebkicher, R., 1960. Aramco Handbook. Arabian American Oil Company.
Leroy, S., Razin, P., Autin, J., Bache, F., Acremont, E., Watremez, L., Lazki, A.A., et al., 2012. From rifting to oceanic spreading in the Gulf of Aden: a synthesis. Arab. J. Geosci. 5, 859–901.
Lim, J.A., Chang, S.J., Mai, P.M., Zahran, H., 2020. Asthenospheric flow of plume material beneath Arabia inferred from S wave traveltime tomography. J. Geophys. Res.-Sol. Ea. 125 (8) https://doi.org/10.1029/2020JB019668.
Lithgow-Bertelloni, C., Silver, P.G., 1998. Dynamic topography, plate driving forces and the African superswell. Nature 395, 269–272. https://doi.org/10.1038/26212.
Liu, L., 2015. The ups and downs of North America: evaluating the role of mantle dynamic topography since the Mesozoic. Rev. Geophys. 53 (3), 1022–1049.
Lu, C., Grand, S.P., Lai, H., Garnero, E.J., 2019. TX2019slab: a new P and S tomography model incorporating subducting slabs. *J. Geophys. Res.: Solid.* Earth 124 (11), 11549–11567.
Lustrino, M., Wilson, M., 2007. The circum-Mediterranean anorogenic Cenozoic igneous province. Earth-Sc. Rev. 81 (1–2), 1–65.
Macgregor, D., 2015. History of the development of the East African Rift System: a series of interpreted maps through time. J. Afr. Earth Sci. 101, 232–252.
Macgregor, D., 2018. History of the development of Permian–Cretaceous rifts in East Africa: a series of interpreted maps through time. Petrol. Geosci. 24 (1), 8–20.
Mackenzie, G.H., Thybo, H., Maguire, P., 2005. Crustal velocity structure across the Main Ethiopian Rift: results from two-dimensional wide-angle seismic modelling. Geophys. J. Int. 162, 994–1006.
McClusky, S., Reilinger, R., Mahmoud, S., Ben Sari, D., Tealeb, A., 2003. GPS constraints on Africa (Nubia) and Arabia plate motions. Geophys. J. Int. 155 (1), 126–138.
McClusky, S., Reilinger, R., Ogubazghi, G., Amleson, A., Healeb, B., Vernant, P., , et al. Kogan, L., 2010. Kinematics of the southern Red Sea–Afar Triple Junction and implications for plate dynamics. Geophys. Res. Lett. 37 (5).
McDougall, I., Morton, W.H., William, M.A.J., 1975. Ages and rates of denudation of trap series basalts at the Blue Nile Gorge, Ethiopia. Nature 254, 207–209.
McKenzie, D., 1984. A possible mechanism for epeirogenic uplift. Nature 307 (5952), 616–618.
McQuarrie, N., Stock, J., Verdel, C., Wernicke, B., 2003. Cenozoic evolution of Neotethys and implications for the causes of plate motions. Geophys. Res. Lett. 30 (20), 2036. https://doi.org/10.1029/2003GL017992.
Mège, D., Purcell, P., Pochat, S., Guidat, T., 2015. The landscape and landforms of the Ogaden, Southeast Ethiopia. Landscapes and landforms of Ethiopia 323–348.
Mège, D., Purcell, P., Bézos, A., Jourdan, F., La, C., 2016. A major dyke swarm in the Ogaden region south of Afar and the early evolution of the Afar triple junction. Geol. Soc. Spec. Publ. 420 (1), 221–248.
Memiş, C., Göğüş, O.H., Uluocak, E.Ş., Pysklywec, R., Keskin, M., Şengör, A.C., Topuz, G., 2020. Long wavelength progressive plateau uplift in Eastern Anatolia since 20 Ma: implications for the role of slab peel-Back and Break-off. Geochem. Geophys. Geosy. 21 (2) e2019GC008726.
Molin, P., Pazzaglia, F.J., Dramis, F., 2004. Geomorphic expression of active tectonics in a rapidly-deforming forearc, Sila massif, Calabria, southern Italy. Am. J. Sci. 304 (7), 559–589.
Merry, T.A., Bastow, I.D., Kounoudis, R., Ogden, C.S., Bell, R.E., Jones, L., 2021. The influence of the North Anatolian Fault and a fragmenting slab architecture on upper mantle seismic anisotropy in the eastern Mediterranean. Geochemistry, Geophysics, Geosystems 22 (9), e2021GC009896.
Molin, P., Fubelli, G., Nocentini, M., Sperini, S., Ignat, P., Grecu, F., Dramis, F., 2012. Interaction of mantle dynamics, crustal tectonics and surface processes in the topography of the Romanian Carpathians: a geomorphological approach. Global Planet. Change. https://doi.org/10.1016/j.gloplacha.2011.05.005.
Molin, P., Sembroni, A., Ballato, P., Faccenna, C., 2023. The uplift of an early stage collisional plateau unraveled by fluvial network analysis and river longitudinal profile inversion: the case of the Eastern Anatolian Plateau. Tectonics 42. https://doi.org/10.1029/2022TC007737 e2022TC007737.
Montagner, J.P., Marty, B., Stutzmann, E., Sicilia, D., Cara, M., Pik, R., Debayle, E., et al., 2007. Mantle upwellings and convective instabilities revealed by seismic tomography and helium isotope geochemistry beneath eastern Africa. Geophys. Res. Lett. 34 (21).

Montelli, R., Nolet, G., Dahlen, F.A., Masters, G., 2006. A catalogue of deep mantle plumes: New results from finite-frequency tomography. Geochem. Geophys. Geosy. 7 (11).
Moucha, R., Forte, A.M., 2011. Changes in African topography driven by mantle convection. Nat. Geosci. 4 (10), 707–712.
Moucha, R., Forte, A.M., Mitrovica, J.X., Rowley, D.B., Quéré, S., Simmons, N.A., Grand, S.P., 2008. Dynamic topography and long-term sea-level variations: there is no such thing as a stable continental platform. Earth Planet. Sci. Lett. 271 (1–4), 101–108. https://doi.org/10.1016/j.epsl.2008.03.056.
Mukhopadhyay, M., Mukhopadhyay, B., Mogren, S., Nandi, B.K., Varghese, S., Ibrahim, E., 2023. Geophysical modelling detects an intrusive magmatic body in the lower crust atop an underplated Moho at the Red Sea rifted margin, Central Saudi Arabia. J. Afr. Earth Sci. 202, 104914.
Murris, R.J., 1980. Middle East: stratigraphic evolution and oil habitat. AAPG Bull. 64 (5), 597–618.
Nelson, W.R., Furman, T., van Keken, P.E., Shirey, S.B., Hanan, B.B., 2012. OsHf isotopic insight into mantle plume dynamics beneath the East African Rift System. Chem. Geol. 320, 66–79.
Nuriel, P., Weinberger, R., Kylander-Clark, A.R.C., Hacker, B.R., Craddock, J.P., 2017. The onset of the Dead Sea transform based on calcite age-strain analyses. Geology 45 (7), 587–590.
Nyblade, A.A., 2011. The upper-mantle low-velocity anomaly beneath Ethiopia, Kenya, and Tanzania: Constraints on the origin of the African superswell in eastern Africa and plate versus plume models of mantle dynamics. Geol. Soc. Am. Spec. Paper 478, 37–50.
Nyblade, A.A., Owens, T.J., Gurrola, H., Ritsema, J., Langston, C.A., 2000. Seismic evidence for a deep upper mantle thermal anomaly beneath East Africa. Geology 28 (7), 599–602.
Ogden, C.S., Bastow, I.D., 2022. The crustal structure of the Anatolian Plate from receiver functions and implications for the uplift of the central and eastern Anatolian plateaus. Geophysical Journal International 229 (2), 1041–1062.
Okay, A.I., Zattin, M., Cavazza, W., 2010. Apatite fission-track data for the Miocene Arabia-Eurasia collision. Geology 38 (1), 35–38. https://doi.org/10.1130/G30234.1.
Padoan, M., Garzanti, E., Harlavan, Y., Villa, I.M., 2011. Tracing nile sediment sources by Sr and Nd isotope signatures (Uganda, Ethiopia, Sudan). Geochim. Cosmochim. Acta 75 (12), 3627–3644.
Panasyuk, S.V., Hager, B.H., 2000. Models of isostatic and dynamic topography, geoid anomalies, and their uncertainties. J. Geophys. Res.-Sol. Ea. 105 (B12), 28199–28209.
Paul, J.D., Roberts, G.G., White, N., 2014. The African landscape through space and time. Tectonics 33 (6), 898–935.
Picard, L., 1951. Geomorphogeny of Israel, part 1 — the Negev. Bull. Res. Counc. Isr. 1 (1–2), 1–32.
Pik, R., Marty, B., Carignan, J., Lavé, J., 2003. Stability of the Upper Nile drainage network (Ethiopia) deduced from (U–Th)/he thermochronometry: implications for uplift and erosion of the Afar plume dome. Earth Plan. Sci. Lett. 215 (1–2), 73–88.
Pik, R., Bellahsen, N., Leroy, S., Denèle, Y., Razin, P., Ahmed, A., Khanbari, K., 2013. Structural control of basement denudation during rifting revealed by low-temperature (U–Th–Sm)/he thermochronology of the Socotra Island basement—Southern Gulf of Aden margin. Tectonophysics 607, 17–31.
Pirouz, M., Avouac, J.P., Hassanzadeh, J., Kirschvink, J.L., Bahroudi, A., 2017. Early Neogene foreland of the Zagros, implications for the initial closure of the Neo-Tethys and kinematics of crustal shortening. Earth Plan. Sci. Lett. 477, 168–182.
Powers, R.W., Ramirez, L.F., Redmond, C.D., Elberg Jr., E.L., 1966. Geology of the Arabian Peninsula: Sedimentary geology of Saudi Arabia (No. 560-D). US Geological Survey.
Prave, A.R., Bates, C.R., Donaldson, C.H., Toland, H., Condon, D.J., Mark, D., Raub, T.D., 2016. Geology and geochronology of the Tana Basin, Ethiopia: LIP volcanism, super eruptions and Eocene–Oligocene environmental change. Earth Plan. Sci. Lett. 443, 1–8.
Priestley, K., McKenzie, D., Debayle, E., Pilidou, S., 2008. The African upper mantle and its relationship to tectonics and surface geology. Geophys. J. Int. 175 (3), 1108–1126.
Purcell, P.G., 2017. Re-imagining and re-imaging the development of the East African Rift. Pet. Geosci. 24 (1), 21–40.
Qaysi, S., Liu, K.H., Gao, S.S., 2018. A database of shear-wave splitting measurements for the Arabian Plate. Seismol. Res. Lett. 89 (6), 2294–2298. https://doi.org/10.1785/0220180144.
Quennell, A.M., 1958. The structural and geomorphic evolution of the Dead Sea Rift. Quat. J. Geol. Soc. Lond. 114, 1–24.
Reeves, C., De Wit, M., 2000. Making ends meet in Gondwana: retracing the transforms of the Indian Ocean and reconnecting continental shear zones. Terra Nova 12 (6), 272–280.
Reilinger, R., McClusky, S., 2011. Nubia–Arabia–Eurasia plate motions and the dynamics of Mediterranean and Middle East tectonics. Geophys. J. Int. 186 (3), 971–979.
Reilinger, R., McClusky, S., Vernant, P., Lawrence, S., Ergintav, S., Cakmak, R., , et al. Karam, G., 2006. GPS constraints on continental deformation in the Africa-Arabia-Eurasia continental collision zone and implications for the dynamics of plate interactions. J. Geophys. Res.-Sol. Ea. 111 (B5).
Reiss, M.C., Long, M.D., Creasy, N., 2019. Lowermost mantle anisotropy beneath Africa from differential SKS-SKKS shear-wave splitting. *J. Geophys. Res.: Solid.* Earth 124 (8), 8540–8564.
Ribe, N.M., Christensen, U.R., 1994a. Three-dimensional modeling of plume-lithosphere interaction. J. Geophys. Res.-Sol. Ea. 99 (B1), 669–682.
Ribe, N.M., Christensen, U.R., 1994b. Three-dimensional modeling of plume-lithosphere interaction. J. Geophys. Res. Solid Earth 99, 669–682.
Ribe, N.M., Christensen, U.R., 1999. The dynamical origin of Hawaiian volcanism. Earth Plan. Sci. Lett. 171 (4), 517–531.
Richards, M.A., Hager, B.H., Sleep, N.H., 1988. Dynamically supported geoid highs over hotspots: Observation and theory. J. Geophys. Res. Solid Earth 93, 7690–7708.
Richards, M.A., Duncan, R.A., Courtillot, V.E., 1989. Flood basalts and hot-spot tracks: plume heads and tails. Science 246, 103–107.
Ritsema, J., van Heijst, H., 2000. New seismic model of the upper mantle beneath Africa. Geology 28 (1), 63–66.
Ritsema, J., van Heijst, H.J., Woodhouse, J.H., 1999. Complex shear wave velocity structure imaged beneath Africa and Iceland. Science 286, 1925–1928. https://doi.org/10.1126/science.286.5446.1925.
Roberts, G.G., White, N., 2010. Estimating uplift rate histories from river profiles using African examples. J. Geophys. Res.-Sol. Ea. 115 (B2).
Roberts, G.G., Paul, J.D., White, N., Winterbourne, J., 2012. Temporal and spatial evolution of dynamic support from river profiles: a framework for Madagascar. Geochem. Geophys. Geosyst. 13 (4).
Robertson, A.H.F., Dixon, J.E., 1984. Introduction: aspects of the geological evolution of the Eastern Mediterranean. Geol. Soc. Spec. Publ. 17 (1), 1–74.
Robertson, A.H., Ustaömer, T., Parlak, O., Ünlügenç, U.C., Taşlı, K., Inan, N., 2006. The Berit transect of the Tauride thrust belt, S Turkey: Late Cretaceous–Early Cenozoic accretionary/collisional processes related to closure of the Southern Neotethys. J. Asian Earth Sci. 27 (1), 108–145.
Robinet, J., Razin, P., Serra-Kiel, J., Gallardo-Garcia, A., Leroy, S., Roger, J., Grelaud, C., 2013. The Paleogene pre-rift to syn-rift succession in the Dhofar margin (northeastern Gulf of Aden): stratigraphy and depositional environments. Tectonophysics 607, 1–16.
Rogers, N.W., 2006. Basaltic magmatism and the geodynamics of the East African Rift System. Geological Society, London, Special Publications 259 (1), 77–93.
Rogers, N., Macdonald, R., Fitton, J., George, R., Smith, R., Barreiro, B., 2000. Two mantle plumes beneath the East African rift system: Sr, Nd and Pb isotope evidence from Kenya Rift basalt. Earth Planet. Sci. Lett. 176, 387–400.
Rooney, T.O., 2017. The Cenozoic magmatism of East-Africa: Part I—flood basalts and pulsed magmatism. Lithos 286, 264–301.
Rooney, T.O., Mohr, P., Dosso, L., Hall, C., 2013. Geochemical evidence of mantle reservoir evolution during progressive rifting along the western Afar margin. Geochim. Cosmochim. Acta 102, 65–88.
Rowley, D.B., Forte, A.M., Moucha, R., Mitrovica, J.X., Simmons, N.A., Grand, S.P., 2013. Dynamic topography change of the eastern United States since 3 million years ago. Science 340 (6140), 1560–1563.
Roy, M., Jordan, T.H., Pederson, J., 2009. Colorado Plateau magmatism and uplift by warming of heterogeneous lithosphere. Nature 459 (7249), 978–982.
Rubey, M., Brune, S., Heine, C.J., Davies, R.D., Williams, S.E., Muller, R.D., 2017. Global patterns in Earth's dynamic topography since the Jurassic: the role of subducted slabs. Sol. Ea. 8, 899–919. https://doi.org/10.5194/se-8-899-2017.
Saeidi, H., Hansen, S.E., Nyblade, A.A., 2023. Deep mantle influence on the Cameroon Volcanic Line. Geochem. Geophy., Geosy. 24 (1) e2022GC010621.
Salameh, H.R., 1997. Geomorphology of the eastern coast of the Dead Sea, Jordan. Geo Journal 41, 255–266.
Schaeffer, A.J., Lebedev, S., 2013. Global shear speed structure of the upper mantle and transition zone. Geophys. J. Int. 194 (1), 417–449.
Schildgen, T.F., Yıldırım, C., Cosentino, D., Strecker, M.R., 2014. Linking slab break-off, Hellenic trench retreat, and uplift of the Central and Eastern Anatolian plateaus. Earth-Sc. Rev. 128, 147–168.
Sella, G.F., Dixon, T.H., Mao, A., 2002. REVEL: a model for recent plate velocities from space geodesy. J. Geophys. Res.-Sol. Ea. 107 (B4), ETG–11.
Sembroni, A., Molin, P., 2018. Long-term drainage system evolution in the Wabe Shebele River basin (SE Ethiopia-SW Somalia). Geomorphology 320, 45–63.
Sembroni, A., Faccenna, C., Becker, T.W., Molin, P., Abebe, B., 2016a. Long-term, deep-mantle support of the Ethiopia-Yemen Plateau. Tectonics 35 (2), 469–488.
Sembroni, A., Molin, P., Pazzaglia, F.J., Faccenna, C., Abebe, B., 2016b. Evolution of continental-scale drainage in response to mantle dynamics and surface processes: an example from the Ethiopian Highlands. Geomorphology 261, 12–29.
Sembroni, A., Kiraly, A., Faccenna, C., Funiciello, F., Becker, T.W., Globig, J., Fernandez, M., 2017. Impact of the lithosphere on dynamic topography: Insights from analogue modeling. Geophys. Res. Lett. 44 (6), 2693–2702.
Sembroni, A., Molin, P., Faccenna, C., 2021. Drainage system organization after mantle plume impingement: the case of the Horn of Africa. Earth-Sc. Rev. 216, 103582.
Sengör, A.M.C., 2001. Elevation as indicator of mantle-plume activity. *Geol. Soc. Am.* Spec. Pap. 352, 183–225.
Şengör, A.M.C., Özeren, S., Genç, T., Zor, E., 2003. East Anatolian high plateau as a mantle-supported, north-south shortened domal structure. Geophys.Res. Lett. 30 (24).
Şengör, A.M.C., Tüysüz, O., Imren, C., Sakınç, M., Eyidoğan, H., Görür, N., Rangin, C., et al., 2005. The North Anatolian fault: a new look. Annu. Rev. Earth Planet. Sci. 33, 37–112.
Şengül Uluocak, E., Göğüş, O.H., Pysklywec, R.N., Chen, B., 2021. Geodynamics of East Anatolia-caucasus domain: inferences from 3D thermo-mechanical models, residual topography, and admittance function analyses. Tectonics 40 (12), e2021TC007031.
Seward, D., Grujic, D., Schreurs, G., 2004. An insight into the breakup of Gondwana: Identifying events through low-temperature thermochronology from the basement rocks of Madagascar. Tectonics 23 (3).
Sicilia, D., Montagner, J.P., Cara, M., Stutzmann, E., Debayle, E., Lépine, J.C., Sholan, J. M., et al., 2008. Upper mantle structure of shear-waves velocities and stratification of anisotropy in the Afar Hotspot region. Tectonophysics 462 (1–4), 164–177.

Sreenidhi, K.S., Betts, P.G., Radhakrishna, M., Armit, R., 2023. Influence of lateral plume channel on the evolution of rift arms of the afar triple junction: constraints from 3-D gravity interpretation. Journal of Geophysical Research: Solid Earth 128 (8), e2023JB026791.

Steinberger, B., 2016. Topography caused by mantle density variations: observation-based estimates and models derived from tomography and lithosphere thickness. Geophysical Supplements to the Monthly Notices of the Royal Astronomical Society 205 (1), 604–621.

Steinberger, B., Bredow, E., Lebedev, S., Schaeffer, A., Torsvik, T.H., 2019. Widespread volcanism in the Greenland–North Atlantic region explained by the Iceland plume. Nat. Geosci. 12 (1), 61–68. https://doi.org/10.1038/s41561-018-0251-0.

Stephenson, S.N., Hoggard, M.J., Holdt, M.C., White, N., 2024. Continental residual topography extracted from global analysis of crustal structure. Journal of Geophysical Research: Solid. Earth 129. https://doi.org/10.1029/2023JB026735 e2023JB026735.

Stern, R.J., 1994. Arc assembly and continental collision in the Neoproterozoic East African orogen. Annu. Rev. Earth Planet. Sci. 22, 319–351.

Stern, R.J., 2002. Crustal evolution in the East African Orogen: a neodymium isotopic perspective. J. Afr. Earth Sci. 34 (3–4), 109–117.

Stow, D., Nicholson, U., Kearsey, S., Tatum, D., Gardiner, A., Ghabra, A., Jaweesh, M., 2020. The Pliocene-recent Euphrates river system: Sediment facies and architecture as an analogue for subsurface reservoirs. Energy Geosci. 1 (3–4), 174–193.

Straume, E.O., Steinberger, B., Becker, T.W., Faccenna, C., 2024. Impact of mantle convection and dynamic topography on the Cenozoic paleogeography of Central Eurasia and the West Siberian Seaway. Earth Planet. Sci. Lett. 630, 118615.

Stüwe, K., Robl, J., Matthai, S., 2009. Erosional decay of the Yucca Mountain crest. Nevada. Geomorphology 108 (3–4), 200–208.

Stüwe, K., Robl, J., Turab, S.A., Sternai, P., Stuart, F.M., 2022. Feedbacks between sea-floor spreading, trade winds and precipitation in the Southern Red Sea. Nat. Commun. 13 (1), 5405.

Styron, R., Pagani, M., 2020. The GEM global active faults database. Earthq. Spectra 36 (1_suppl), 160–180.

Tang, Z., Mai, P.M., Chang, S.J., Zahran, H., 2018. Evidence for crustal low shear-wave speed in Western Saudi Arabia from multi-scale fundamental-mode Rayleigh-wave group-velocity tomography. Earth Plan. Sci. Lett. 495, 24–37. https://doi.org/10.1016/j.epsl.2018.05.011.

Telbisz, T., Kovács, G., Székely, B., Szabó, J., 2013. Topographic swath profile analysis: a generalization and sensitivity evaluation of a digital terrain analysis tool. Z. Geomorphol. 57 (4), 485–513.

Thiede, R.C., Bookhagen, B., Arrowsmith, J.R., Sobel, E.R., Strecker, M.R., 2004. Climatic control on rapid exhumation along the Southern Himalayan Front. Earth Plan. Sci. Lett. 222 (3–4), 791–806.

Thrastarson, S., van Herwaarden, D.P., Noe, S., Josef Schiller, C., Fichtner, A., 2024. REVEAL: a global full-waveform inversion model. Bull. Seism. Soc. Am. 114 (3), 1392–1406.

Tiberi, C., Ebinger, C., Ballu, V., Stuart, G., Oluma, B., 2005. Inverse models of gravity data from the Red Sea-Aden-East African rifts triple junction zone. Geophys. J. Int. 163, 775–787. https://doi.org/10.1111/j.1365-246X.2005.02736.x.

Trifonov, V.G., Dodonov, A.E., Sharkov, E.V., Golovin, D.I., Chernyshev, I.V., Lebedev, V. A., Ali, O., et al., 2011. New data on the late Cenozoic basaltic volcanism in Syria, applied to its origin. J. Volc. Geotherm. Res. 199 (3–4), 177–192.

Tsekhmistrenko, M., Sigloch, K., Hosseini, K., Barruol, G., 2021. A tree of Indo-African mantle plumes imaged by seismic tomography. Nat. Geosci. 14 (8), 612–619. https://doi.org/10.1038/s41561-021-00762-9.

Turab, S.A., Stüwe, K., Stuart, F.M., Cogne, N., Chew, D.M., Robl, J., 2023. A two phase escarpment evolution of the Red Sea margin of southwestern Saudi Arabia. Insights from low-temperature apatite thermochronology. Earth Plan. Sci. Lett. 603, 117990.

Turcotte, D.L., Schubert, G., 1982. Geodynamics: Applications of Continuum Physics to Geological Problems. John Wiley, New York.

Ukstins Peate, I., Bryan, S.E., 2008. Re-evaluating plume-induced uplift in the Emeishan large igneous province. Nat. Geosci. 1 (9), 625–629.

Vigny, C., Huchon, P., Ruegg, J.C., Khanbari, K., Asfaw, L.M., 2006. Confirmation of Arabia plate slow motion by new GPS data in Yemen. J. Geophys. Res.-Sol. Ea. 111 (B2).

Viltres, R., Jónsson, S., Alothman, A.O., Liu, S., Leroy, S., Masson, F., et al., 2022. Present-day motion of the Arabian plate. Tectonics 41 (3) e2021TC007013.

Wegmann, K.W., Pazzaglia, F.J., 2009. Late Quaternary fluvial terraces of the Romagna and Marche Apennines, Italy: Climatic, lithologic, and tectonic controls on terrace genesis in an active orogen. Quat. Sci. Rev. 28 (1–2), 137–165.

Wegmann, K.W., Zurek, B.D., Regalla, C.A., Bilardello, D., Wollenberg, J.L., Kopczynski, S.E., Pazzaglia, F.J., et al., 2007. Position of the Snake River watershed divide as an indicator of geodynamic processes in the greater Yellowstone region, western North America. Geosphere 3 (4), 272–281.

Wei, W., Zhao, D., Wei, F., Bai, X., Xu, J., 2019. Mantle dynamics of the eastern Mediterranean and Middle East: Constraints from P-wave anisotropic tomography. Geochem. Geophys. Geosy. 20 (10), 4505–4530. https://doi.org/10.1029/2019gc008512.

Weissbrod, T., Gvirtzman, G., 1989. Crustal thinning possibly related to late paleozoic updoming: evidence from two near eastern megastructures. Bulletin de la Société belge de géologie 98 (2), 235–237.

Weissel, J., Malinverno, A., Harding, D., 1995. Erosional development of the Ethiopian Plateau of Northeast Africa from fractal analysis of topography. In: Barton, C.C., Pointe, P.R. (Eds.), Fractals in Petroleum Geology and Earth Processes. Plenum Press, New York, pp. 127–142.

Wessel, P., Luis, J.F., Uieda, L.A., Scharroo, R., Wobbe, F., Smith, W.H., Tian, D., 2019. The Generic Mapping Tools version 6. Geochem. Geophys. Geosyst. 20, 5556–5564.

Williams, M., 2019. The sudd swamps and the white nile. The Nile Basin: Quaternary Geology, Geomorphology and Prehistoric Environments. Cambridge University Press, Cambridge, p. 107e126. https://doi.org/10.1017/9781316831885.009.

Wolfenden, E., Ebinger, C., Yirgu, G., Renne, P.R., Kelley, S.P., 2005. Evolution of a volcanic rifted margin: Southern Red Sea, Ethiopia. Geol. Soc. Am. Bull. 117 (7–8), 846–864.

Yao, Z., Mooney, W.D., Zahran, H.M., Youssef, S.E.H., 2017. Upper mantle velocity structure beneath the Arabian shield from Rayleigh surface wave tomography and its implications. J. Geophys. Res.-Sol. Ea. 122 (8), 6552–6568. https://doi.org/10.1002/2016JB013805.

Yeats, R., 2012. Active Faults of the World. Cambridge University Press.

Ziegler, M.A., 2001. Late Permian to Holocene paleofacies evolution of the Arabian plate and its hydrocarbon implications. GeoArabia 6, 445–504.

Zilberman, E., 1991. Landscape evolution in the central, northern and northwestern Negev during the Neogene and the Quaternary. Isr. Geol. Surv. Rep. GSI/45/90, 164 pp.

Zilberman, E., Calvo, R., 2013. Remnants of Miocene fluvial sediments in the Negev Desert, Israel, and the Jordanian Plateau, evidence for an extensive subsiding basin in the northwestern margins of the Arabian plate. J. Afr. Earth Sci. 82, 33–53.